Graduate School of Science
Osaka University

Interaction between Alternating Magnetic Fields and a Relativistic Collisionless Shock

A dissertation submitted in partial satisfaction
of the requirements for the degree
Doctor of Philosophy in Department of Physics

by

Kentaro Nagata

2008

Table of Contents

List of Figures

List of Tables

Acknowledgments

First of all, I would like to express my deep gratitude to my research supervisor, Professor Hideaki Takabe at Osaka University and Professor Masahiro Hoshino at the University of Tokyo during the doctoral course.

I would like to express my gratitude for helpful comments and advice by Prof. Shin'pei Shibata, Prof. Toshio Terasawa, Prof. Masafumi Hirahara, Dr. Takaaki Yokoyama, Dr. Tsunehiko N. Kato, Dr. Seiji Zenitani, Dr. Claus Jaroschek, Takanobu Amano and Ryo Yoshitake.

I would like to express appreciation of colleagues and secretaries, who have supported my school life, Dr. N. Shimada, Dr. H. Isobe, Dr. S. Imada, Dr. M. N. Nishino, T. Minoshima, N. Watanabe, Y. Takagi, T. Tanaka, T. Yamamoto, T. Kawashima, S. Notoya, M. Hirai, Y. Mimura, K. Hashimoto, S. Nagasaki, Y. Iida, T. Mukasa and Y. Hosoi at the University of Tokyo. Also I would like to express gratitude to Dr. Y. Kuramitsu, Dr. W. Feilu, T. Kawashima, Y. Fukuda, Y. Yasuhara, M. Taniguchi, and A. Kageyama at Osaka University.

The computational resources for this work are supported by NEC SX-8 and SX-6 at Cybermedia Center of Osaka University.

Finally, I would like to express my deepest gratitude to my parents, who had long supported me since they gave birth to me.

Publications and Presentations

Particle Acceleration in Kinetic Plasma Processes

M. Hoshino, S. Zenitani, K. Nagata, and Y. Takagi (2006)

in Katsuhiko Sato and Junji Hisano ed. Energy Budget in the High Energy Universe, World Scientific

Interaction between Alternating Magnetic Fields and a Relativistic Collisionless Shock

K. Nagata, M. Hoshino, C. Jaroschek, and H. Takabe (2007), submitted

The Astrophysical Journal, University of Chicago Press

A Practical Solution for Numerical Cherenkov Radiation Problem

K. Nagata and T. N. Kato (2008), submitted

Journal of Computational Physics, Elsevier

Committee on Space Research 36th COSPAR Scientific Assembly

K. Nagata and M. Hoshino

Beijing, China, 16-23 July 2006

The Extreme Universe in the Suzaku Era

K. Nagata and M. Hoshino

Kyoto, Japan, 4-8 December 2006

Abstract of the Dissertation

Interaction between Alternating Magnetic Fields and a Relativistic Collisionless Shock

by

Kentaro Nagata

Doctor of Philosophy in Department of Physics

Osaka University, 2008

The non-thermal spectrum is usual in our universe. This means that a part of particles should be strongly accelerate in collisionless plasma, although the precise mechanism is not clear yet. The relativistic astrophysical objects with non-thermal spectrum are, for instance, pulsar nebulae, active galactic nuclei (AGN) jets and γ-ray bursts (GRBs). Additionally cosmic-ray also represents non-thermal spectrum including extremely high energy particles. On the other hand, the energy conversion from magnetic field to particles is also an important problem for these objects. In the pulsar nebulae the energy conversion of the stellar wind between the neutron star and the surrounding shock wave should be solved to explain the theoretical and observational model. In AGN jets and GRBs, the energy conversion is expected to explain the highly relativistic bulk flow.

In this thesis, we focus on two ordinary phenomena to solve the above problems. One is a shock wave, and the other is dissipation of alternating magnetic field. The former exists everywhere a supersonic flow collides other matters. The latter is also common feature on "active" magnetized objects. Then we study the interaction between alternating magnetic fields and a shock wave using numerical simulations. In order to investigate the realistic mechanism of the particle acceleration and the magnetic dissipation, we choose the Particle-in-Cell (PIC) method which can treat kinetic plasma processes.

First, we show the solution to the problem for the numerical simulation. The PIC simu-

lations of relativistic plasma flows in two or three dimensions have a trouble of the numerical Cherenkov radiation, it is excited because the speed of light is reduced numerically in such simulations especially in large wavenumber region due to the effects of the finite size of spatial grid and time steps. There is a method that can solve the dispersion relation of the electromagnetic waves correctly and the well-known cause of the numerical Cherenkov radiation is removed with this method. However, there is another cause due to the numerical aliasing effect of the current density, which involves the shape factor of particles used in the PIC simulations. The aliasing component of the current density resonates with the electromagnetic waves and causes the numerical Cherenkov radiation. When the flow of plasma is highly relativistic, the numerical Cherenkov radiation can be avoided with an appropriate filter. On the other hand, when the flow is mildly relativistic, one may have to use a higher-order shape factor to decrease the aliasing effect.

Next, we investigate the interaction between alternating magnetic fields with cold current sheets and a relativistic collisionless shock wave by one-dimensional PIC simulations. We found that a precursor wave, propagating from the shock front to upstream, accelerates dense current sheet plasma in the upstream. In case that the current sheet width and each clearance are larger than the typical gyro-radius of the downstream plasma, the current sheet excites a large amplitude magnetosonic wave in the downstream by the collision with a shock front. The motional electric field accompanied with the magnetosonic wave can further accelerate the pre-accelerated particles, forming a non-thermal energy spectrum. In addition, the current sheet structure is stable against not only the collision but also compression by other current sheets. On the other hand, in the small current sheet case, which means the case that the current sheet width and each clearance is smaller than the downstream gyro-radius, the magnetic field dissipates and the magnetosonic wave excitation is absent. This situation can be applied to pulsar wind nebulae, and the result of the dissipation could solve the σ problem.

Finally, we study the two-dimensional interaction using the exact spectral method. The particle with larger gyro-radius than the clearance of each current sheets flows back upstream from the shock front. We found that such back-flow excites the Weibel instability. The insta-

bility generate not only magnetic field, but also electric field in the shock downstream frame. The electric field, different from alternating background component, accelerates particles. In case that the current sheet width and each clearance are smaller than the typical gyro-radius of the downstream plasma, the alternating magnetic fields completely dissipate within the shock transition region. Particles are not affected the alternating magnetic fields but the magnetic field excited by the Weibel instability. In case that the width and the clearance are comparable or larger than the gyro-radius, partial magnetic reconnection make the shock downstream nonuniformalize. So the large amplitude magnetosonic waves are dispersed during the propagation. Unlike the small case, the alternating magnetic field accelerates back-flow particles. Furthermore the residual magnetic fields often reflect the accelerated particles to the upstream. This can yield the long term acceleration process.

This thesis consists of the following chapters and appendixes. In chapter 1, general information of this study is introduced. In chapter 2, the solution to the numerical Cherenkov radiation is resented. In chapter 3, one-dimensional study of the interaction between alternating magnetic fields and a shock is presented. In chapter 4, the two-dimensional study is presented. In chapter 5, we summarize and conclude this thesis.

CHAPTER 1

General Introduction

1.1 General introduction

Plasma is one of the most common material in our universe. Plasma is a group of a mixture of positively and negatively charged particles. Curiously, such simple components yield extremely complicated phenomena. The plasma physics has been developed in the field of the nuclear fusion, the earth's ionosphere, the earth' magnetosphere and so on. In laboratories people can generate plasma and measure it by using various instruments. Around the earth, people cannot control these natural plasma, but can measure via radio wave or instruments on satellites. In these cases people can get the precise data of the plasma phenomena. However, astrophysical objects are too far from the earth to be precisely observed in spite of the fact that they also include the complicated plasma phenomena.

For a long time, the astrophysics are mainly developed as the macro physics, because the observed parameters are the value integrated over the global scale. These studies explain the phenomena well in many cases, but some cases are not explained or not so well, because the plasma density is too small and the kinetic effect is important in such collisionless plasma. For example, macro physical approach can not treat particle acceleration mechanism in a precise sense.

The particle acceleration is common problem everywhere in our universe. Non-Thermal particles are observed on the earth magnetosphere, solar flares, super nova shocks, pulsar nebulae, active galactic nuclei (AGN) jets and γ-ray burst (GRB), and as cosmic-rays. The diffusive shock acceleration (DSA) is a plausible solution to this problem (Blandford and Ostriker, 1978;

Bell, 1978a,b), but not available for every cases (Chiueh, 1989; Begelman and Kirk, 1990). For example, the DSA is not efficient for the shock with highly relativistic upstream flow. In such case the magnetic field angle to the shock normal is almost perpendicular, called a perpendicular shock, because the perpendicular component of the magnetic field in the proper frame increases the "Lorentz factor" times in the shock frame. In the DSA process the particle must move back and forth between the upstream and the downstream to gain their energy. In case of perpendicular shock, the particles are bounded along the magnetic field line (Hudson, 1965), and hardly across the shock front.

The major instances accompanying such a highly relativistic shock are pulsar nebulae, AGN jets and GRBs. The central engine of these objects radiates huge energy, so the radiation exceed the electron rest mass generates electron-positron pair. Then the plasma of the outflow would mainly consist of electron and positron, which is called pair-plasma. Then the micro physical process in pair-plasma is considered to overcome the difficulty of the particle acceleration. For example, Hoshino (2001) showed the shock surfing acceleration in pair-plasma. Originally the shock surfing acceleration in electron-ion plasma was advanced by Sagdeev (1966), which is a direct acceleration at the shock front. Zenitani and Hoshino (2001) also showed the acceleration by the magnetic reconnection, which is energy release process by an alternating magnetic fields (e.g., Jaroschek et al., 2004; Zenitani and Hoshino, 2005, 2007).

For the pulsar nebula, recently the magnetic field reversal and the shock wave in the stellar wind are focused as a plausible solution to the particle acceleration and the magnetic field dissipation problem (σ-problem). The alternating magnetic field and the shock wave are not unique structure of the pulsar nebulae but would be common for AGN jets and GRBs. The interaction between supersonic flow and interplanetary medium should generate a shock wave, and rotating magnetized objects should form magnetic field reversal.

Such relativistic collisionless shock and alternating magnetic field in pair-plasma can not be generated in a laboratory. On the astrophysical objects, the physical parameters are completely different from the ones in the other fields. On the basis of the knowledge of the plasma physics developed in the other fields, people need numerical simulations to study the complicated micro

plasma processes on the astrophysical objects.

One of the effective methods to simulate the micro scale plasma phenomena is Particle-in-Cell (PIC) method. In this method the equation of motion solves the particle trajectory and a full set of the Maxwell equations solve electro-magnetic field. Therefore, although the calculation consumes a large amount of computational resources, the PIC method can simulate all kind of plasma phenomena in principle. Fortunately tremendous increase in processing power of computers makes large scale numerical simulations possible in late years.

In this Ph.D thesis we study the interaction between current sheets and a relativistic shock via numerical simulations with PIC method. We are mainly interested in the particle acceleration and the magnetic field dissipation process by the interaction. In this chapter we show the general feature of the relativistic collisionless shock in pair plasma and the introduction of the astrophysical objects to be applied our scenario.

1.2 Uniform Collisionless Shock in Relativistic Pair Plasma

The major difference between electron-ion plasma and electron-positron (pair) plasma is their mass ratio. In the electron-ion plasma the asymmetrical motion due to the mass difference can generate a strong electro-static field, and waves with the electro-static field play a key role in many kind of phenomena. On the other hand the symmetrical mass of the pair plasma does not yield such a large electro-static field. Of cause some waves consist of the electro-static field, but do not have much effect on the phenomena. Furthermore pair-plasma is usually relativistic, because only the extremely high energy source can generate such nearly pure pair plasma. If the bulk velocity of the upstream flow is relativistic, the magnetic field component perpendicular to the flow direction is boosted the "Lorentz factor" times. Therefore in case that the Lorentz factor of the bulk velocity is much larger than unity, the magnetic field direction against the shock normal is almost perpendicular in the shock frame.

This shock structure can be characterize a Lorentz invariant parameter σ (Kennel and

Coroniti, 1984a),

$$\sigma = \frac{B_1^2}{8\pi mc^2 n_1 \gamma_1}, \tag{1.1}$$

where the parameters noted "1" are upstream quantities in the shock frame, and B, n and γ are the magnetic field, number density of electron/positron and the Lorentz factor of the upstream bulk flow, respectively. The notation is common in this chapter, but not used the following chapters. Basically the Rankine-Hugoniot relations describe the shock profiles.

$$n_1 u_1 = n_2 u_2, \tag{1.2}$$

$$\frac{u_1 B_1}{\gamma_1} = \frac{u_2 B_2}{\gamma_2}, \tag{1.3}$$

$$\gamma_1 \mu_1 + \frac{B_1^2}{4\pi\gamma_1 n_1} = \gamma_2 \mu_2 + \frac{B_2^2}{4\pi\gamma_2 n_2}, \tag{1.4}$$

$$\mu_1 u_1^2 n_1 + P_1 + \frac{B_1^2}{8\pi} = \mu_2 u_2^2 n_2 + P_2 + \frac{B_2^2}{8\pi}, \tag{1.5}$$

where notation "2" means the downstream quantities in the shock frame. u is the four-velocity of the bulk flow and γ is its Lorentz factor ($\gamma = \sqrt{1 + u^2/c^2}$). μ is the specific enthalpy written by

$$\mu = mc^2 + \frac{\Gamma}{\Gamma - 1}\left(\frac{P}{n}\right), \tag{1.6}$$

where P is the gas pressure and Γ is a adiabatic index. In case of relativistic gas, the Γ is 4/3 for three-dimensional distribution of the particle velocity and 3/2 for the two-dimensional one. For example, in case that the magnetic field is perpendicular to the simulation space, the adiabatic index Γ is 3/2. Equation (1.2)-(1.5) mean conservation of mass flux, magnetic flux, energy and momentum, respectively. On the assumption of cold and highly relativistic upstream flow, $P_1 \ll n_1 mc^2$ and $u_1 \gg c$, equation (1.2)-(1.5) can be solved for each parameters. The downstream velocity is

$$\begin{aligned} \frac{v_2}{c} &= \frac{u_2}{c\gamma_2} \\ &= \frac{1}{2(\sigma+1)}\left[\left(\frac{\Gamma}{2}\sigma + \Gamma - 1\right) + \sqrt{\left(\frac{\Gamma}{2}\sigma + \Gamma - 1\right)^2 + 4\sigma(\sigma+1)\left(1 - \frac{\Gamma}{2}\right)}\right], \end{aligned} \tag{1.7}$$

and the compression ratio of the number density and magnetic field between the upstream and the downstream are

$$\frac{n_2}{n_1} = \frac{B_2}{B_1} = 1 + \frac{1}{v_2/c}. \tag{1.8}$$

Figure 1.1 shows the behavior of equation (1.7) and (1.8) for σ. Although the above parameters are defined in the shock frame, the shock simulations are usually performed in the shock downstream frame. In the shock down stream, the shock front propagates with the shock downstream velocity v_2 defined in the shock frame, and the compression ratio is not changed.

Figure 1.2 shows the result of the one-dimensional perpendicular shock simulation for $\sigma = 0.14$. Cold magnetized pair plasma is injected from the left boundary $x = 0$, and the right boundary ($x = 30R_c$) reflects the particles and electro-magnetic fields, where the spacial unit is gyro-radius defined by the upstream magnetic field and the bulk Lorentz factor $R_c = \gamma_0 mc^2/(eB_{z0})$. Here the notation "0" means the initial upstream value. The shock front is located at $x \sim 15.5R_c$. The right-side of the shock front is the shock downstream. In the shock downstream the average of the perpendicular electric field E_y is zero, because of the plasma has no bulk motion. The perpendicular magnetic field B_z is compressed as the suggestion by equation (1.8). The downstream plasma is strongly thermalized.

In the upstream the large amplitude extraordinary mode (X-mode) wave, so called precursor wave, propagates leftward from the shock front with nearly light velocity. The collective motion of the upstream plasma on the shock front generates the X-mode wave via the synchrotron maser instability (Hoshino and Arons, 1991). The excitation of the precursor wave means that the wave absorbs the energy in the downstream and on the shock front. Actually the energy absorption by the precursor wave requires the Rankine-Hugoniot relations, equation (1.2)-(1.5), to be modified (Gallant et al., 1992). They showed that the precursor has peak-energy with 10% of the injection total energy for $\sigma \simeq 0.1$. The Poynting flux of the precursor wave is far from negligible. However the upstream plasma does not resonant with the precursor because the X-mode wave does not satisfy the cyclotron resonance condition. In particular, the dispersion

relation of the X-mode for cold plasma is

$$\frac{c^2k^2}{\omega^2} = \frac{\omega^2/\Omega^2 - 1 - \omega_p^2/\Omega^2}{\omega^2/\Omega^2 - 1} < 1, \tag{1.9}$$

where ω_p is plasma frequency in pair plasma, $\omega_p = \sqrt{8\pi ne^2/m}$, and Ω is gyro frequency, $\Omega = eB/(mc)$. These parameters are defined for cold plasma in the plasma proper frame. Equation (1.9) can be rewritten by

$$\frac{\omega^2}{\Omega^2} = 1 + \frac{\omega_p^2}{\Omega^2\left(1 - c^2k^2/\omega^2\right)} > 1. \tag{1.10}$$

This result shows no cyclotron resonance. In the phase space plot for u_y in figure 1.2, one can see modulation of the upstream flow by the precursor but no heating.

1.3 Application to Astrophysical Objects

Both of the alternating magnetic field and the relativistic shock can be ordinary structures on the relativistic astrophysical objects. For example pulsar nebulae, GRBs and AGNs can include these structures. The radiation from these objects show the power-law spectrum, which suggests the existence of the non-thermal electrons/positrons. We introduce the model of the pulsar nebulae and the one of GRBs and AGNs briefly.

1.3.1 Pulsar Wind Nebula

The pulsar nebula is driven by the rotational energy of the central neutron star (Michel, 1982). Despite observational and theoretical researches for a long time, the detailed mechanism includes open questions (Gaensler and Slane, 2006; Arons, 2004). Radio pulsars which is driven by its rotation energy are rapidly spinning and strongly magnetized neutron stars. With a typical radius of $r_{NS} \sim 10$ km, magnetic field strengths of 10^{12} G are reached on the surface. Rotation periods T_r are about one second and co-rotation of the pervasively dipolar magnetic field extends towards the light cylinder $r_L = cT_r/2\pi$, see figure 1.3. In case of the Crab nebula the rotation period is $T_r \approx 33$ ms and the light cylinder is $r_L \approx 158 r_{NS}$. Electrostatic gap

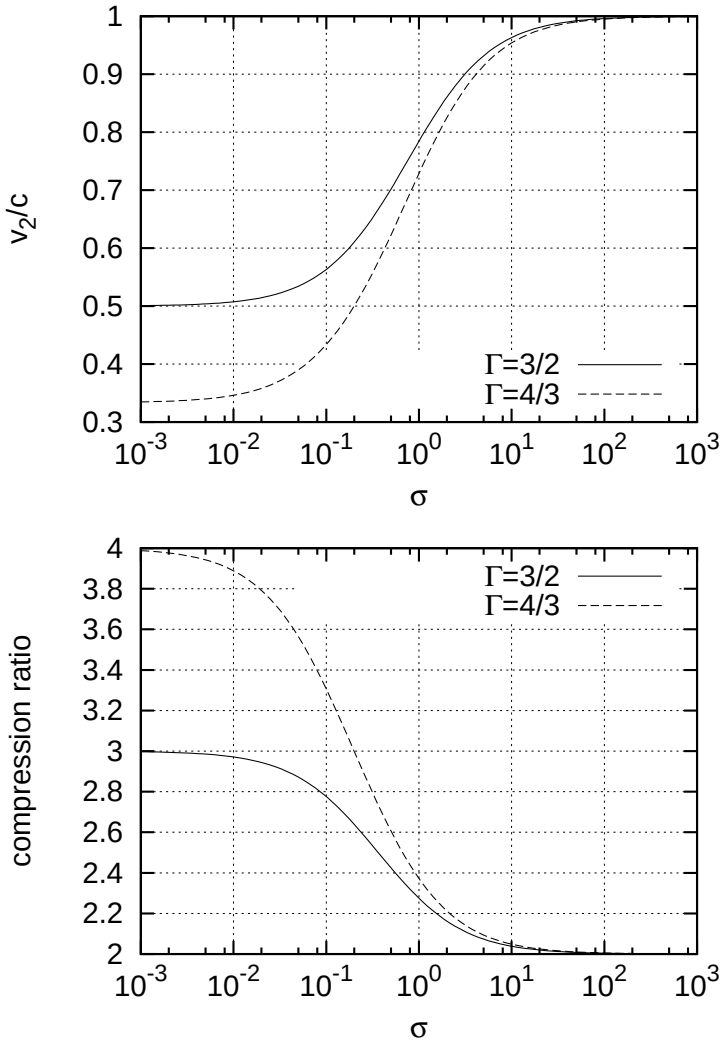

Figure 1.1: σ value dependencies of the shock parameters. Top plots show the downstream flow velocity (equation (1.7)) and bottom ones show the compression ratio of the number density and the magnetic field (equation (1.8)).

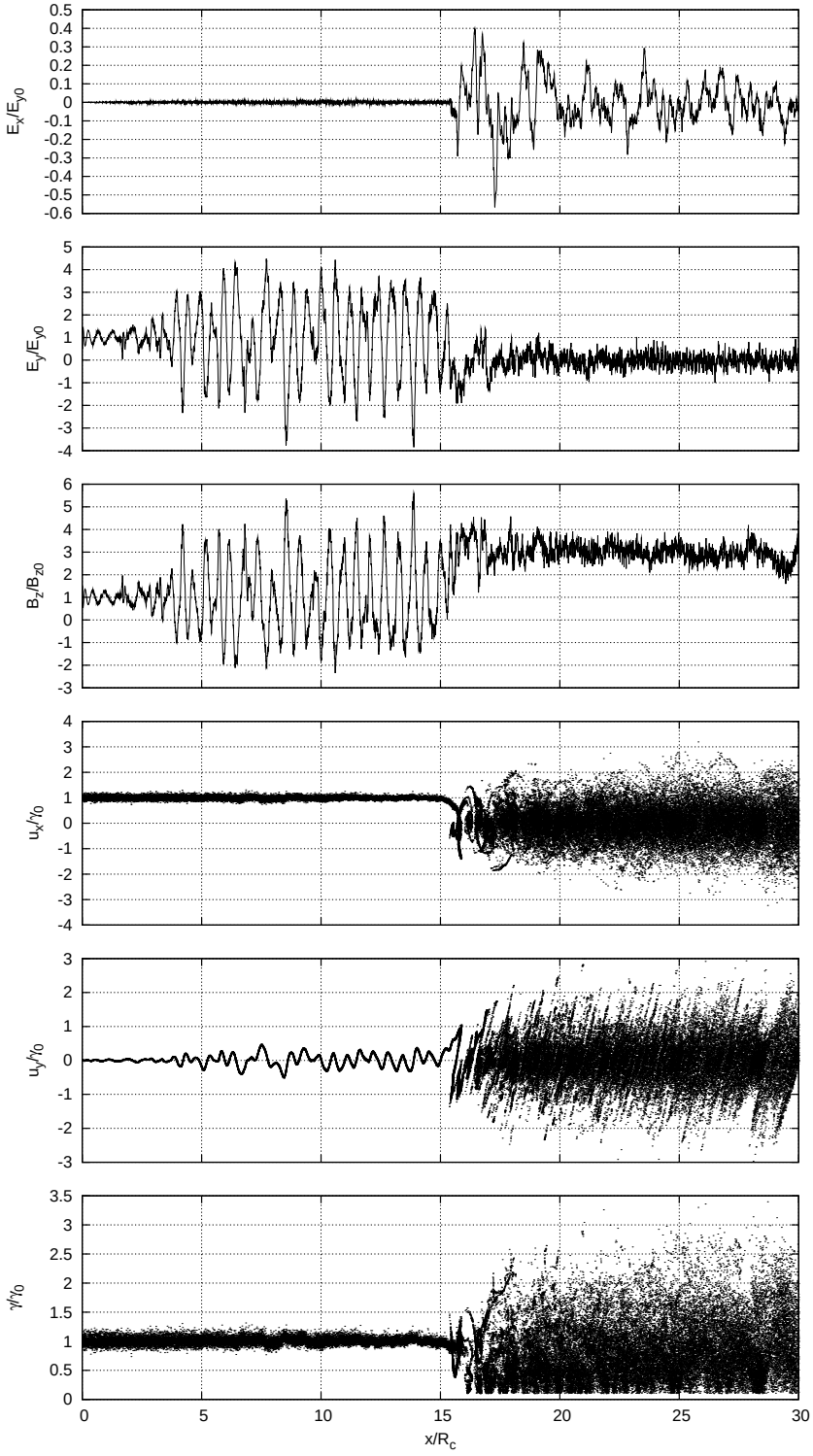

Figure 1.2: Uniform shock profiles for $\sigma = 0.14$. From top, electro-static field (E_x), perpendicular electric field (E_y), perpendicular magnetic field (B_z), four-velocity of the particles along the simulation space (u_x), four-velocity of perpendicular component (u_y) and the Lorentz factor (γ).

in the magnetosphere accelerates electrons (positrons) to relativistic energy, then they radiate γ-ray which generate pair plasmas. The pairs fill the magnetosphere (Goldreich and Julian, 1969) escape along the open magnetic field line outward, which is called pulsar wind.

The Crab Nebula is well observed in broad band and in high resolution due to the comparatively small distance of 2 kpc. Chandra X-ray observatory shows the double ring structure (Weisskopf et al., 2000), see figure 1.6. The inner ring generated by the interaction between the pulsar outflow and the supernova remnant is located about 0.1 pc from the center. Schmidt et al. (1979) showed the "winding up" of the magnetic field lines by the pulsar rotation via the optical polarization by observation (e.g., Bietenholz and Kronberg, 1990; Hickson and van den Bergh, 1990)).

Rees and Gunn (1974) outlined the hydrodynamic model. The morphology is basically consistent with recent observations. Furthermore Kennel and Coroniti (1984a,b) proposed a one-dimensional spherical MHD model (KC model, see figure 1.5) (e.g., Emmering and Chevalier, 1987). The model suggested that the ratio of magnetic field energy flux to kinetic energy flux (σ parameter, defined by equation (1.1)) and bulk Lorentz factor of the upstream flow at the immediate shock upstream are 3×10^{-3} and 10^6, respectively. The σ value means that the kinetic energy is dominant around the shock in contrast to the situation close to the light cylinder $\sigma \sim 10^4$ (Rees and Gunn, 1974; Arons, 1979; Coroniti, 1990), so called "σ problem". The spectrum of the Crab Nebula shown in figure 1.4 exhibits highly non-thermal features (Aharonian and Atoyan, 1998; Mori et al., 2004) which is indicative for the presence of some particle acceleration process. Because of extremely high Lorentz factor 10^6 of the flow, the toroidal magnetic field perpendicular to the flow direction is relativistically boosted. In such a perpendicular shock case the diffusive shock acceleration, the standard theory of particle acceleration, is not an efficient mechanism of particle acceleration. The particle acceleration and the magnetic dissipation (σ-problem) are two of the unsolved issues.

Although the KC model neglected the magnetic field structure in the pulsar wind, the magnetic field polarity is alternating around the equatorial plane due to oblique rotation of the pulsar (Michel, 1973; Kirk et al., 2002) The structure of the pulsar wind propagates toward ter-

mination shock from the central pulsar (Michel, 1971; Coroniti, 1990; Michel, 1994; Lyubarsky and Kirk, 2001). Kirk and Skjæraasen (2003) calculated a dissipation of the alternating magnetic field during the propagation with three dissipation processes; slow, fast and tearing mode instability. According to the article the magnetic field does not dissipate enough to explain the σ value $\sim 3.0 \times 10^{-3}$, required by the KC model in case of standard pair creation rate in the pulsar magnetosphere (Hibschman and Arons, 2001a,b). In this case the σ parameter is larger than 0.003 suggested by KC model. This means that the alternating magnetic fields remains until the shock front. On the one hand, Kirk (2004) proposed the acceleration by the magnetic reconnection in the shock upstream (e.g., Kirk, 2006). On the other, Lyubarsky (2003) showed current sheets dissipation on the shock front yield a consistent result with KC model and also discussed the possibility of particle acceleration. The dissipation process in this article is that the alternating magnetic fields annihilate due to magnetic reconnection which is driven by strong compression from highly relativistic bulk pressure of inflow. They have shown that high energy particles are generated on the assumption that magnetic reconnection form a power law spectrum via induction electric field (Zenitani and Hoshino, 2001). Lyubarsky (2005) and Pétri and Lyubarsky (2007) studied a dissipation of the alternating magnetic field with relativistic hot current sheet plasma in the pulsar wind nebula by means of full particle simulations (PIC). Pétri and Lyubarsky (2007) found a criterion of the dissipation in the high-σ case.

We apply some of our results to the particle acceleration problem and the σ problem. The scale of alternating magnetic field pitch should be comparable to the radius of the light cylinder. The radius of light cylinder for the Crab nebula is $r_L \sim 1600$km as noted above. On the other hand the typical gyro-radius of the particles in the shock downstream is roughly $R_g \sim 1.7 \times 10^8$km by using a particle Lorentz factor $\sim 3 \times 10^6$ (Kennel and Coroniti, 1984a,b; de Jager and Harding, 1992) and the magnetic field $\sim 3 \times 10^{-4}$G determined by Marsden et al. (1984) due to a turnoff point of the spectrum at infrared (Green et al., 2004). So the alternating magnetic field scale is much smaller than the gyro-radius of the downstream particles. Of course one can not cover both scales in one time by numerical simulations. We extrapolate the pulsar case by the simulation in the case of $r_L < R_g$.

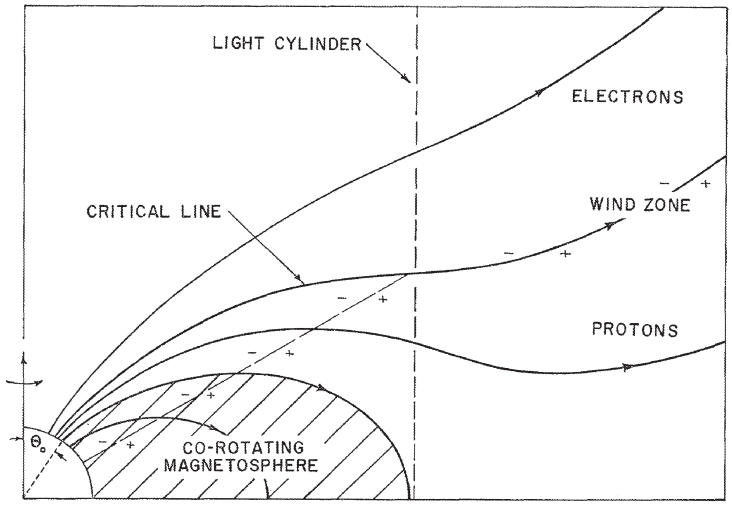

Figure 1.3: Schematic diagram showing the corotation magnetosphere and the wind zone (from Goldreich and Julian (1969)). The neutron star is at lower left.

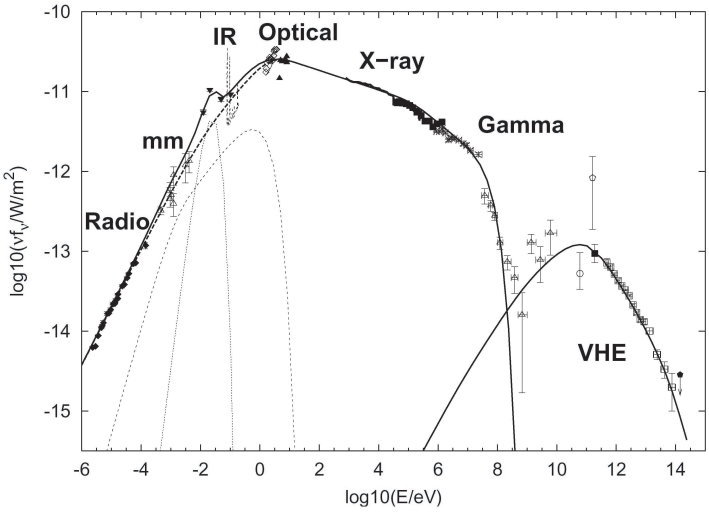

Figure 1.4: The photon spectrum of the Crab nebula in multi-wavelength (from Horns and Aharonian (2004)).

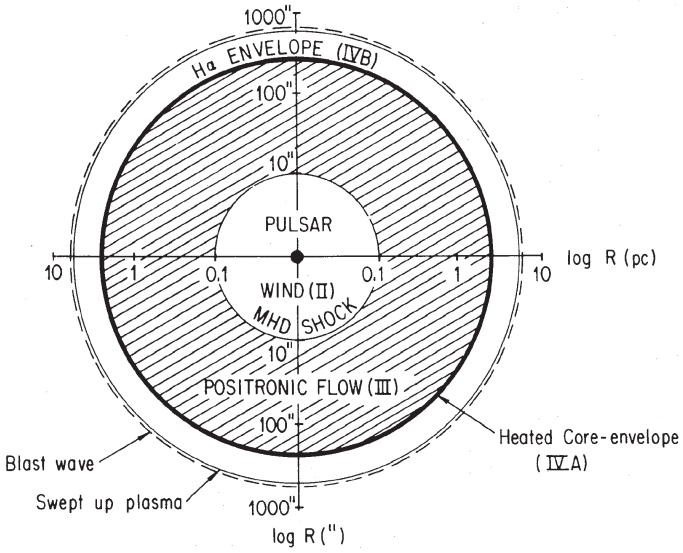

Figure 1.5: Schematic relation between the Crab nebula and supernova remnant (from Kennel and Coroniti (1984a)).

1.3.2 Relativistic flow by GRB and AGN

GRBs and AGN jets are also plausible sources of relativistic flow. Because GRBs are located at cosmological distance, it is impossible to resolve spacially by observations. However the models are advanced using indirect evidences. The standard is "fire ball model" (Piran, 1999; Mészáros, 2001). This model requires high Lorentz factor jet $\gamma \sim 100$ with multiple shock to explain several observations. For example, non-thermal spectrum, pulse time scale, temporal difference of pulses and energy flux are well explained via Lorentz contraction, time delay and beaming by the special relativity. Although AGNs are also located at large distance, the jet is directly observable due to its huge scale 100kpc - 1Mpc. In addition to the GRB case, the superluminal motion of the jet also requires the high Lorentz factor of $\gamma \sim 10 - 20$ (Vermeulen and Cohen, 1994). The central engines in both objects radiate huge energy, so the radiation exceed the electron rest mass generates electron-positron plasma. Therefore the jets include the pair at a high rate, compared to proton. Furthermore both objects show the non-thermal spectrum. At present the acceleration mechanism is explained by the diffusive shock acceleration. However

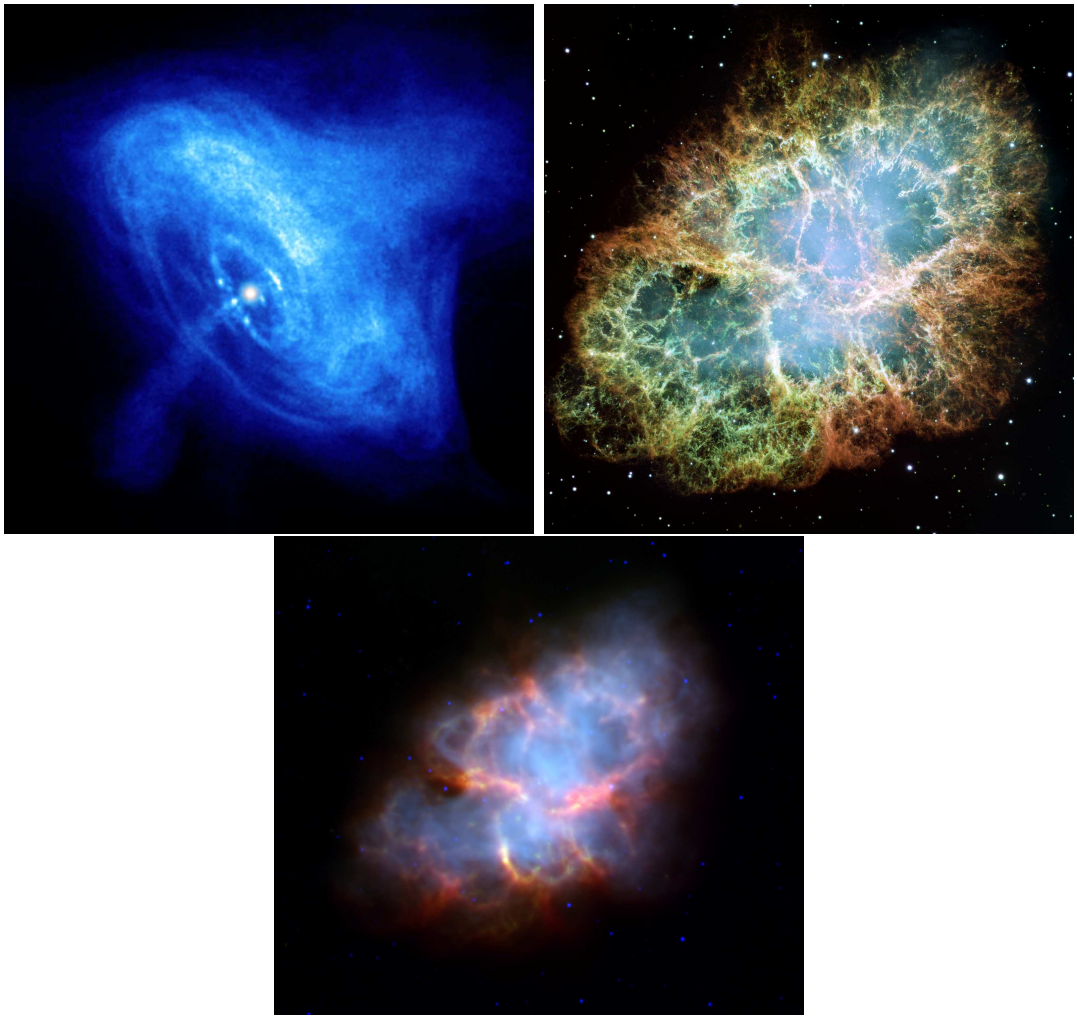

Figure 1.6: The images of the Crab nebula. Left top is the X-ray image by the Chandra X-ray Observatory. Right top is the optical image by the NASA Hubble Space Telescope. Bottom is the infrared image by the Spitzer Space Telescope. The view angles of the images are 2.24, 8.2 and 8 arcmin across, respectively.

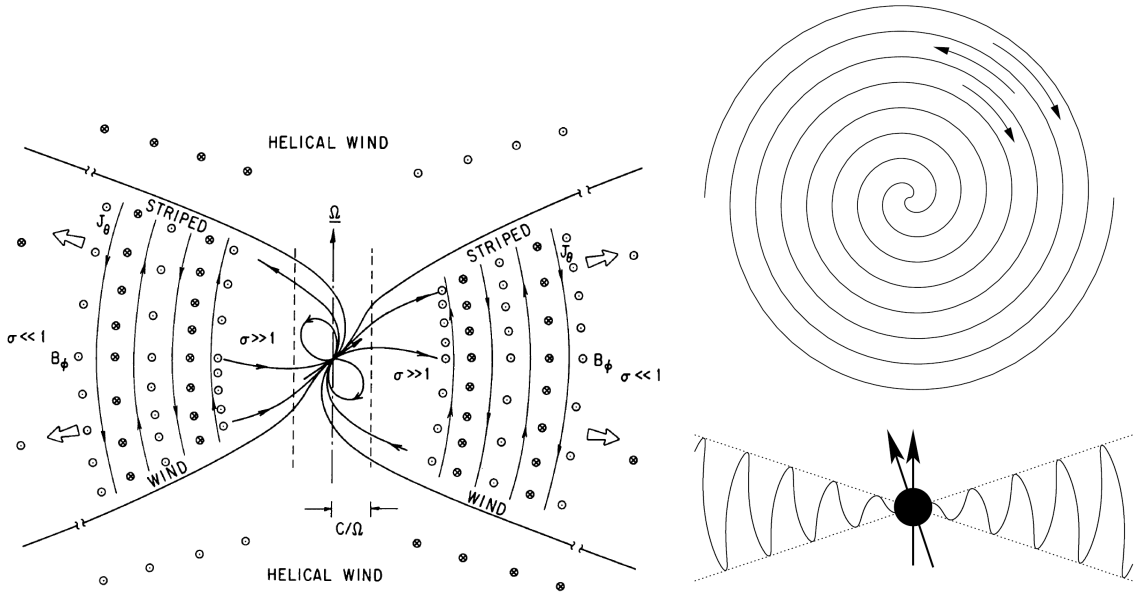

Figure 1.7: Schematic view of the striped wind. Left shows a plausible magnetic topology for a relativistic MHD wind from an oblique rotator (from Coroniti (1990)). The toroidal magnetic field has an alternating polarity near the rotational equator. Right top shows the toroidal magnetic field with Parker spiral pattern as seen from the rotational axis, and right bottom shows the magnetic neural sheet structure (solid line) as seen from the rotational equatorial plane (from Kirk and Skjæraasen (2003)).

the specific acceleration process is not clear yet. The existence of the magnetic field is believed both on AGN jets (Larrabee et al., 2003) and on GRB (Drenkhahn and Spruit, 2002). If the object include magnetic fields with active motion of the central engine, the anti-parallel structure of the magnetic fields would naturally arise. We envision the interaction between the shock and anti-parallel magnetic fields to accelerate particles.

CHAPTER 2

A Practical Solution for Numerical Cherenkov Radiation Problem

The Particle-in-Cell (PIC) simulations of relativistic plasma flows in two or three dimensions have a trouble of the numerical Cherenkov radiation; it is excited because the speed of light is reduced numerically in such simulations especially in large wavenumber region due to the effects of the finite size of spatial grid and time steps. There is a method that can solve the dispersion relation of the electromagnetic waves correctly and the well-known cause of the numerical Cherenkov radiation is removed with this method. However, there is another cause due to the numerical aliasing effect of the current density, which involves the shape factor of particles used in the PIC simulations. The aliasing component of the current density resonates with the electromagnetic waves and causes the numerical Cherenkov radiation. When the flow of plasma is highly relativistic, the numerical Cherenkov radiation can be avoided with an appropriate filter. On the other hand, when the flow is mildly relativistic, one may have to use a higher-order shape factor to decrease the aliasing effect.

2.1 Introduction

Astrophysical objects are studied from the standpoint of the microscopic plasma physics in late years. Accordingly, the Particle-in-Cell (PIC) simulation is often used to study phenomena involved with the relativistic plasma dynamics. In such simulations, the phase velocity of electromagnetic wave that is reduced by a numerical effect and so relativistic particles can move faster than it. These particles excite the Cherenkov radiation as real, which is called the

numerical Cherenkov radiation (Godfrey, 1974). In the following, we review how the numerical effects modify the dispersion relation of electromagnetic waves.

In the PIC simulation, two of the Maxwell's equations are used to advance the electromagnetic fields,

$$\frac{1}{c}\frac{\partial \boldsymbol{E}}{\partial t} = \boldsymbol{\nabla} \times \boldsymbol{B} - \frac{4\pi}{c}\boldsymbol{J}, \tag{2.1}$$

$$\frac{1}{c}\frac{\partial \boldsymbol{B}}{\partial t} = -\boldsymbol{\nabla} \times \boldsymbol{E}. \tag{2.2}$$

The other equations

$$\boldsymbol{\nabla} \cdot \boldsymbol{B} = 0, \tag{2.3}$$

$$\boldsymbol{\nabla} \cdot \boldsymbol{E} = 4\pi\rho \tag{2.4}$$

are used as constraints. The correct dispersion relation of the electromagnetic wave in vacuum is derived from equation (2.1) and (2.2) ignoring the current term $\boldsymbol{J}$,

$$\omega = kc, \tag{2.5}$$

where c is the speed of light, ω is a frequency and k is a wavenumber.

In the PIC simulation, one of the most popular methods to advance the electromagnetic fields in time with the Maxwell's equations is the finite-difference-time-domain (FDTD) method (Yee, 1966). The reasons many people use the FDTD method would be its flexibility and simplicity. In case of the FDTD methods, the phase velocity of the electromagnetic wave becomes smaller than the true value, equation (2.5), especially in the large wavenumber region.

Using the leap-frog algorithm with the explicit time integration, the dispersion relation of the electromagnetic wave becomes

$$\left(\frac{1}{c\Delta t}\sin\frac{\omega\Delta t}{2}\right)^2 = \sum_{j=x,y,z}\left(\frac{1}{\Delta j}\sin\frac{k_j\Delta j}{2}\right)^2, \tag{2.6}$$

where Δj and k_j $(j = x, y, z)$ are the size of the spatial grid and the wavenumbers in the j direction, respectively. Δt is the time step. In the following, let us consider the dispersion

relation of the electromagnetic wave in the x direction for simplicity.

$$\frac{1}{c\Delta t}\sin\frac{\omega\Delta t}{2} = \frac{1}{\Delta x}\sin\frac{k_x\Delta x}{2}. \tag{2.7}$$

We see that the above relation gives the correct dispersion relation ($\omega = kc$) when the Courant number ($c\Delta t/\Delta x$) is unity, although it holds only along one of the axes. However, the explicit method becomes unstable when the Courant number is larger than unity, the case of $c\Delta t/\Delta x = 1$ is marginally stable in numerical simulations, and so it is impractical. When the Courant number is smaller than unity, the method is stable, although the dispersion relation is deviated from the correct relation as is shown in figure 2.1.

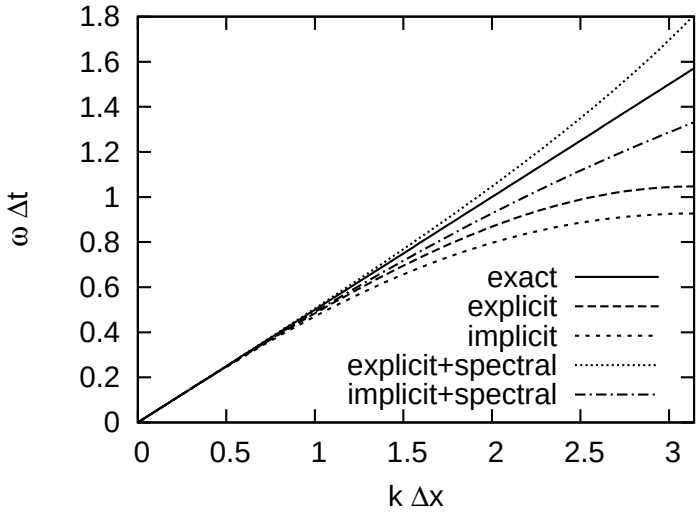

Figure 2.1: Dispersion relations of electromagnetic wave in vacuum. These five plots ("exact," "explicit," "implicit," "explicit+spectral" and "implicit+spectral") are described by equation (2.5), (2.7), (2.8), (2.13) and (2.14), respectively. The Nyquist wavenumber is given by $k_{x,\max}\Delta x = \pi$. For all numerical schemes, the Courant number ($c\Delta t/\Delta x$) is 0.5. Therefore, the slope of the exact solution in this figure is also 0.5.

The implicit time integration schemes can avoid the restriction of the Courant condition, because of their stability for any Courant number. For example, the dispersion relation of the

electromagnetic wave for Crank-Nicolson scheme is given by

$$\frac{1}{c\Delta t/2}\tan\left(\frac{\omega\Delta t}{2}\right) = \frac{1}{\Delta x/2}\sin\left(\frac{k_x\Delta x}{2}\right). \tag{2.8}$$

This relation also does not give the correct solution (see figure 2.1).

One of the ways to improve the dispersion relation in PIC simulation is to use the spectral method. This method solves the Maxwell's equations in the Fourier space, then the Maxwell's equations become as follows,

$$\frac{1}{c}\frac{\partial\tilde{\boldsymbol{E}}}{\partial t} = i\boldsymbol{k}\times\tilde{\boldsymbol{B}} - \frac{4\pi}{c}\tilde{\boldsymbol{J}}, \tag{2.9}$$

$$\frac{1}{c}\frac{\partial\tilde{\boldsymbol{B}}}{\partial t} = -i\boldsymbol{k}\times\tilde{\boldsymbol{E}}, \tag{2.10}$$

$$\boldsymbol{k}\cdot\tilde{\boldsymbol{B}} = 0, \tag{2.11}$$

$$\boldsymbol{k}\cdot\tilde{\boldsymbol{E}} = 4\pi\tilde{\rho}, \tag{2.12}$$

where $\mathbf{k} = (k_x, k_y, k_z)$ is a wave vector, and the tilde means the Fourier transform. Although the effect of the finite grid size (Δx) still emerges through the Nyquist wavenumber, the numerical dispersion of the electromagnetic wave caused by the spatial finite differences is eliminated in this method. The dispersion relation of electromagnetic wave by the spectral method with explicit and implicit schemes are respectively given by as follows:

$$\sin\frac{\omega\Delta t}{2} = \frac{k_x c\Delta t}{2}, \tag{2.13}$$

$$\tan\frac{\omega\Delta t}{2} = \frac{k_x c\Delta t}{2}. \tag{2.14}$$

The dispersion relations of the electromagnetic wave in vacuum obtained from the above methods (equation (2.13) and (2.14)) are shown in figure 2.1. It should be noted that the dispersion relations obtained from the spectral methods (both explicit and implicit) approach the true relation when we take $\Delta t \to 0$, whereas the phase velocity of equation (2.13) is always larger than the true value in the explicit spectral method and always smaller than the true value in the implicit spectral method.

The above methods cannot solve the dispersion relation of the electromagnetic wave correctly, especially in large wavenumber region. This yields the numerical Cherenkov radiation.

In the following section, we show a method that leads the correct dispersion relation even in the large wavenumber region.

2.2 The Exact Spectral Method

Godfrey (1974) studied the methods to avoid the numerical Cherenkov radiation. One of the remarkable methods mentioned in the article, which solves the Maxwell's equations in the Fourier space, can solve the electromagnetic waves in vacuum correctly. Here, we explain that method.

By combining equation (2.9) and (2.10), a second order differential equation is obtained. This differential equation can be solved exactly on the assumption that the current density ($\tilde{\boldsymbol{J}}$) is constant during a time interval $[0, t]$, with equation (2.11) as follows,

$$\begin{aligned}\tilde{\boldsymbol{E}}(t) &= \cos(kct)\tilde{\boldsymbol{E}}(0) + i\frac{\sin(kct)}{k}\boldsymbol{k}\times\tilde{\boldsymbol{B}}(0) - \frac{\sin(kct)}{k}\frac{4\pi}{c}\tilde{\boldsymbol{J}} \\ &\quad + \left\{(1-\cos(kct))\,\boldsymbol{k}\cdot\tilde{\boldsymbol{E}}(0) - \frac{kct-\sin(kct)}{k}\boldsymbol{k}\cdot\left(\frac{4\pi}{c}\tilde{\boldsymbol{J}}\right)\right\}, \qquad (2.15)\\ \tilde{\boldsymbol{B}}(t) &= \cos(kct)\tilde{\boldsymbol{B}}(0) - i\frac{\sin(kct)}{k}\boldsymbol{k}\times\tilde{\boldsymbol{E}}(0) + i\frac{1-\cos(kct)}{k^2}\boldsymbol{k}\times\left(\frac{4\pi}{c}\tilde{\boldsymbol{J}}\right), \qquad (2.16)\end{aligned}$$

where $k = |\mathbf{k}| = \left(k_x^2 + k_y^2 + k_z^2\right)^{1/2}$.

Generally, a vector ($\boldsymbol{A}$) can be separated into the longitudinal ($\boldsymbol{A}_\parallel$) and the transverse ($\boldsymbol{A}_\perp$) component to a wave vector $\mathbf{k}$ considered,

$$\boldsymbol{A}_\parallel \equiv \frac{\boldsymbol{k}}{k^2}(\boldsymbol{k}\cdot\boldsymbol{A}), \qquad \boldsymbol{A}_\perp \equiv \boldsymbol{A} - \boldsymbol{A}_\parallel. \qquad (2.17)$$

Then, the time integration equation for the electric field (2.15) is separated into those for the longitudinal part and the transverse part, as follows,

$$\begin{aligned}\tilde{\boldsymbol{E}}_\parallel(t) &= \tilde{\boldsymbol{E}}_\parallel(0) - 4\pi\tilde{\boldsymbol{J}}_\parallel t, \qquad (2.18)\\ \tilde{\boldsymbol{E}}_\perp(t) &= \cos(kct)\tilde{\boldsymbol{E}}_\perp(0) + \frac{\sin(kct)}{k}\left(i\boldsymbol{k}\times\tilde{\boldsymbol{B}}_\perp(0) - \frac{4\pi}{c}\tilde{\boldsymbol{J}}_\perp\right). \qquad (2.19)\end{aligned}$$

equation (2.18) describes the time development of the longitudinal electric field. However, in PIC simulations, the constraint condition (the Poisson equation) equation (2.12) is generally

not satisfied with this equation. To ensure the condition, instead of equation (2.18), one can use the following equation for the longitudinal electric field,

$$\tilde{\boldsymbol{E}}_{\parallel}(t) = -4\pi i \frac{\boldsymbol{k}}{k^2}\rho(t). \tag{2.20}$$

Eventually, combining the longitudinal part and the transverse part again, we obtain a set of equations to advance the electric and magnetic fields,

$$\tilde{\boldsymbol{E}}(t) = \cos(kct)\tilde{\boldsymbol{E}}_{\perp}(0) + \frac{\sin(kct)}{k}\left(i\boldsymbol{k}\times\tilde{\boldsymbol{B}}(0) - \frac{4\pi}{c}\tilde{\boldsymbol{J}}_{\perp}\right) - 4\pi i\frac{\boldsymbol{k}}{k^2}\rho(t), \tag{2.21}$$

$$\tilde{\boldsymbol{B}}(t) = \cos(kct)\tilde{\boldsymbol{B}}_{\perp}(0) - i\frac{\sin(kct)}{k}\boldsymbol{k}\times\tilde{\boldsymbol{E}}(0) + i\frac{1-\cos(kct)}{k^2}\boldsymbol{k}\times\left(\frac{4\pi}{c}\tilde{\boldsymbol{J}}\right), \tag{2.22}$$

where the longitudinal magnetic field $\tilde{\boldsymbol{B}}_{\parallel}$ is excluded from the first term in the right side of equation (2.22) to ensure the constraint (2.11). For the discrete time step Δt, for which the time is given by $t = n\Delta t$ where n is the step of simulation, the time advance equations from the step n to the step $n+1$ are written as

$$\tilde{\boldsymbol{E}}^{n+1} = \cos(kc\Delta t)\tilde{\boldsymbol{E}}^{n}_{\perp} + \frac{\sin(kc\Delta t)}{k}\left(i\boldsymbol{k}\times\tilde{\boldsymbol{B}}^{n} - \frac{4\pi}{c}\tilde{\boldsymbol{J}}^{n+1/2}_{\perp}\right) - 4\pi i\frac{\mathbf{k}}{k^2}\rho^{n+1}, \tag{2.23}$$

$$\tilde{\boldsymbol{B}}^{n+1} = \cos(kc\Delta t)\tilde{\boldsymbol{B}}^{n}_{\perp} - i\frac{\sin(kc\Delta t)}{k}\boldsymbol{k}\times\tilde{\boldsymbol{E}}^{n} + i\frac{1-\cos(kc\Delta t)}{k^2}\boldsymbol{k}\times\left(\frac{4\pi}{c}\tilde{\boldsymbol{J}}^{n+1/2}\right). \tag{2.24}$$

The representative value of the current density, which is assumed constant for the time interval Δt in the time integration, is taken at the half time step $n+1/2$, as usual in the leap-frog algorithm. The dispersion relation of the electromagnetic wave in this method gives the correct solution for large wavenumber. In the following, we call this method "the exact spectral method." The dispersion relation obtained from a simulation with this method is shown in figure 2.2 together with those obtained by other two methods.

2.3 Numerical Cherenkov Radiation Caused by Aliases

The method described in the previous section provides the exact dispersion relation for the electromagnetic waves. However, the numerical Cherenkov radiation still can be caused by the aliasing effect due to the finite time step and the finite spatial grid. There are two different

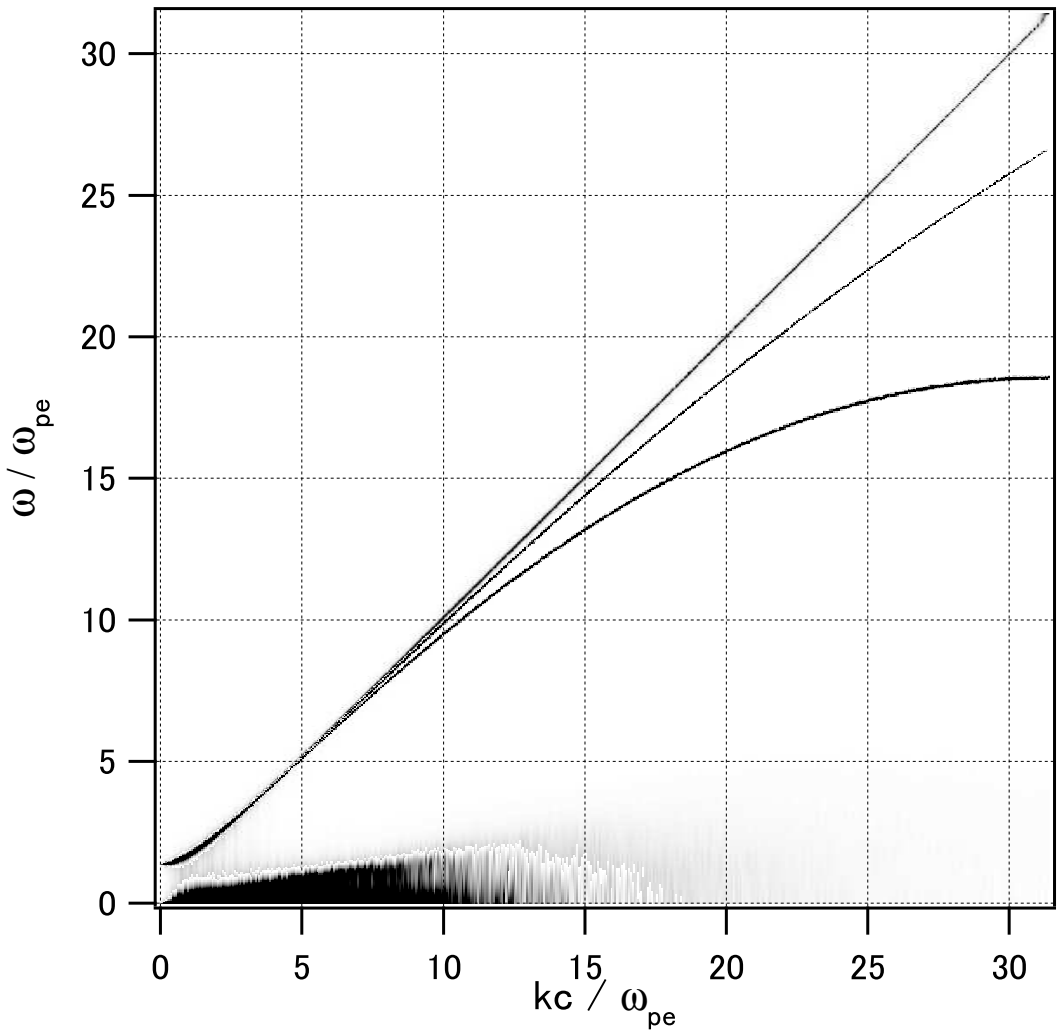

Figure 2.2: The dispersion relations for electromagnetic wave in uniform plasma obtained from three two-dimensional simulations with different schemes. Here we used the Fourier transformation of B_z for the spatial data and then the maximum entropy method for the temporal data to make this plot. The result of the exact spectral method is shown by the upper curve. The other two curves are obtained from the implicit finite-difference method (lower curve) and the implicit spectral method (middle curve), respectively.

causes. One is related to the alias in the time (frequency) domain, and the other is caused by the alias in the current density calculated from the particle quantities with a shape factor. The latter is significant when relativistic bulk flows exist.

Thus, the concept of the Nyquist frequency/wavenumber is essential in the following arguments. For the time step Δt and the grid size Δx, Δy, and Δz for each axis, the corresponding Nyquist frequency and wavenumbers are given by $\omega_{\max} = \pi/\Delta t$, $k_{x,\max} = \pi/\Delta x$, $k_{y,\max} = \pi/\Delta y$, and $k_{z,\max} = \pi/\Delta z$, respectively. The maximum Nyquist wavenumber in three dimensions is given by $k_{\max} = (k_{x,\max}^2 + k_{y,\max}^2 + k_{z,\max}^2)^{1/2}$.

2.3.1 The aliasing in the frequency domain

The former case occurs when the Nyquist frequency is smaller than the maximum Nyquist wavenumber, $\omega_{\max} < k_{\max} c$. Let us consider the problem in the $\omega - k$ space for an arbitrary wave vector $\mathbf{k}$. In the present case, the dispersion relation of the electromagnetic waves is reflected at $\omega = \omega_{\max}$ for $k > \omega_{\max}/c$ due to the aliasing effect (see figure 2.3), because the exact solution of the Maxwell's equations includes the contributions even from the high-frequency modes with $\omega = kc > \omega_{\max}$. Therefore, the phase velocity of the electromagnetic waves in this domain decreases linearly with k and it eventually becomes smaller than the typical velocity of particles. This results in the numerical Cherenkov radiation. Then, the line of dispersion relation in the $\omega - k$ space again reflected at $\omega = 0$ and so the phase velocity turns to increase with k. Such reflections in the $\omega - k$ space are repeated until k reaches $k_{\max}$. Figure 2.4 shows the power spectrum of B_z in the $k_x - k_y$ space obtained from a two-dimensional simulation of a relativistic uniform flow in the x direction using the exact spectral method. The bulk Lorentz factor of the flow is $\Gamma = 1000$. The Nyquist frequency and wavenumbers are $\omega_{\max} = 62.8\omega_{\rm pe}$ and $k_{\max} = \sqrt{2}k_{x,\max} = 4540\omega_{\rm pe}/c$, where $\omega_{\rm pe}$ is the electron plasma frequency. The simulation was calculated until the numerical Cherenkov radiation emerged significantly. The numerical Cherenkov radiation caused by the aliasing effect is evident.

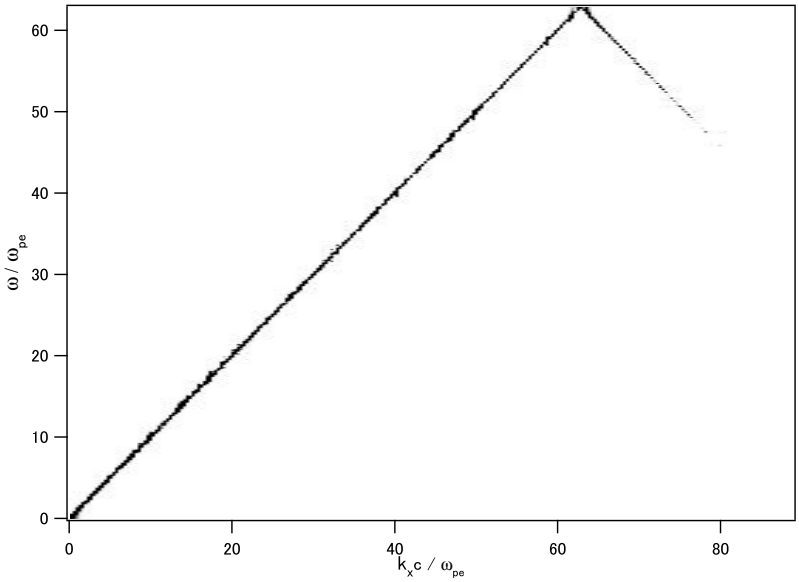

Figure 2.3: The dispersion relation of electromagnetic wave obtained from a simulation with the exact spectral method as in figure 2.2 but for $\omega_{\max}/k_{\max} = 0.5$, where $\omega_{\max} = 62.8\omega_{\rm pe}$ and $k_{\max} = 125.7\omega_{\rm pe}/c$.

2.3.2 The aliasing of the current density

The latter case can occur even when $\omega_{\max} \geq k_{\max}c$ as well as when $\omega_{\max} < k_{\max}c$ because of the aliasing effect arising from the shape factor of the particles, $S(x)$, which is used when calculating the contribution of each particle to the current density on the grid, that is, since we *sample* the particle's current using the shape factor on the grid, which has a finite spacing, the modes in the Fourier transform of the shape factor, $S(k)$, with k larger than the Nyquist wavenumber results in the aliasing effect. For example, one of the most popular shape factors (one dimension, for simplicity), which has a triangle shape,

$$S_1(x) = \begin{cases} 1 - \dfrac{|x|}{\Delta x} & (|x| < \Delta x) \\ 0 & (\text{otherwise}), \end{cases} \tag{2.25}$$

has the Fourier transform given by

$$S_1(k) = \left[\frac{\sin(k\Delta x/2)}{k\Delta x/2}\right]^2. \tag{2.26}$$

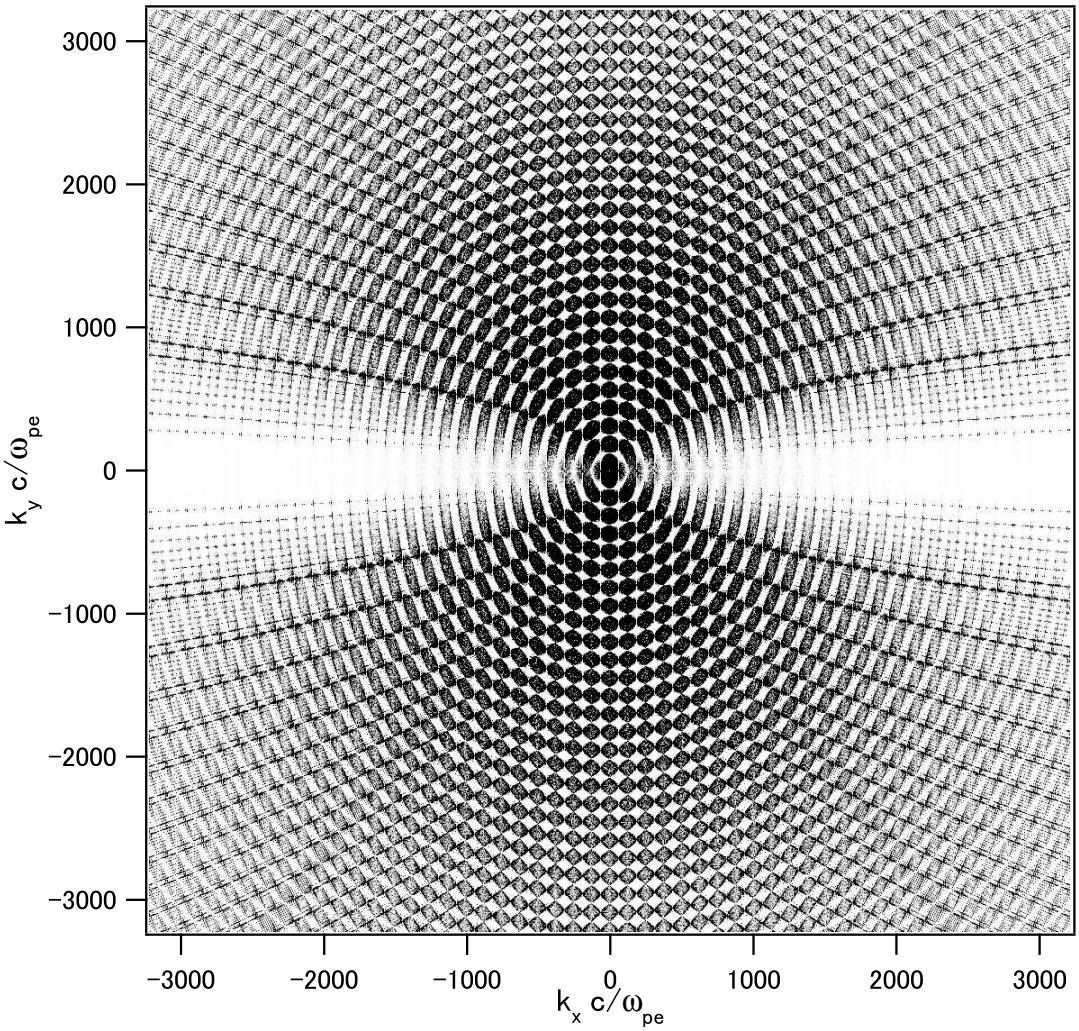

Figure 2.4: The power spectral density of B_z obtained from a two-dimensional simulation of a relativistic uniform flow in the x direction with a bulk Lorentz factor of $\Gamma = 1000$. The ratio of the Nyquist frequency to the maximum Nyquist wavenumber is $\omega_{\max}/k_{\max}c \sim 0.014$. The darker the plot, the stronger the power.

It is clear that the amplitude of this function decreases as k^{-2} and remains finite even for $k > k_{\max}$.

Here, let us consider the present case in a simple situation where a cold uniform plasma flows in the x direction with a bulk velocity of V, which is not necessarily relativistic. If back-reactions are negligible, the (spatial) Fourier transform of the current density has the following time dependence:

$$\tilde{\mathbf{J}} = \tilde{\mathbf{J}}_0 e^{-ik_x V t}, \tag{2.27}$$

where $\tilde{\mathbf{J}}_0$ is the Fourier transform of the current density at $t = 0$ and k_x is the wavenumber in the x direction. This is also accompanied by the fluctuation of electric and magnetic fields and can provide the source for the numerical Cherenkov radiation. The point is that when $\tilde{\mathbf{J}}$ is calculated on the grid, it includes an aliasing effect due to the sampling of the shape factor mentioned above (cf. Birdsall and Langdon, 2005, Chapter 8) and, as a result, large-wavenumber modes with $k_x > k_{x,\max}$ are folded at $k_x = k_{x,\max}$ in the $\omega - k$ space. Note that in the present situation the reflection condition depends only on k_x because the "dispersion relation" of the fluctuation of the current density is given by $\omega = k_x V$ according to the phase factor in equation (2.27). When the plasma flows in the y direction, the reflection is involved with only k_y. Thus, the line of $\tilde{\mathbf{J}}$ reflected at $k = k_{x,\max}$ crosses the dispersion relation of the electromagnetic wave somewhere causing the numerical Cherenkov radiation, although the phase velocity of the electromagnetic waves is correctly solved with the exact spectral method. As already mentioned, since the Fourier transform of the shape factor, in general, remains finite value even for large k, the line of $\tilde{\mathbf{J}}$ is also reflected at $\omega = 0$, $\omega = \omega_{\max}$, $k = 0$, and $k_{x,\max}$, and crosses (or resonates with) the dispersion relation of the electromagnetic waves, $\omega = kc$, repeatedly (see figure 2.5). The all crossing points (or resonance points) can cause the numerical Cherenkov radiation as well. However, in general, only the first crossing point is important because the shape factor $S(k)$ usually decreases rapidly with k.

The location of the first crossing point in the wavenumber space can be found by solving the following set of equations for $0 < k_x < k_{x,\max}$,

$$\omega = kc, \tag{2.28}$$

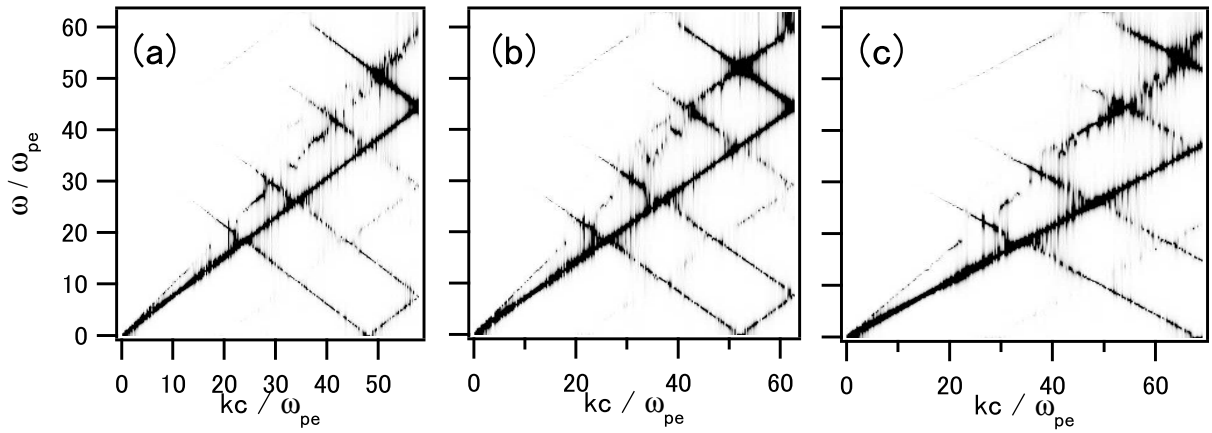

Figure 2.5: Same as in figure 2.3 but for a relativistic flow with $\Gamma = 1000$ in the x direction and $\omega_{\max}/k_{\max} = 1$, where $\omega_{\max} = 62.8\omega_{\rm pe}$ and $k_{\max} = 62.8\omega_{\rm pe}/c$. The angles of propagation, where $k_x = k\cos\theta$, are (a) $\theta = 40°$, (b) $\theta = 45°$, and (c) $\theta = 50°$, respectively.

$$\omega = k_{x,\max}V + (k_{x,\max} - k_x)V, \tag{2.29}$$

with $k_x = k\cos\theta$, where θ is the angle between the direction of the flow (i.e., the x axis here) and that of the wave vector $\mathbf{k}$ considered. The first equation is the dispersion relation of the electromagnetic waves in vacuum. The second one is the condition for the fluctuation of the current density that is reflected once at $k_x = k_{x,\max}$. The solution is given by

$$k = \frac{2(V/c)}{1 + (V/c)\cos\theta}k_{x,\max} \tag{2.30}$$

for $0 \le |\theta| \le \pi/2$. This means an ellipsoid (or an ellipse in two dimension) with the latus rectum $l = 2(V/c)k_{x,\max}$ and the eccentricity $\epsilon = V/c$ for $0 < V/c < 1$, or a paraboloid (or a parabola in two dimension) for $V/c = 1$. Since we treat the Fourier transforms of the real quantities (for example, B_z), the solution is symmetrical about the origin for $\pi/2 < |\theta| \le \pi$. Figure 2.6 shows the power spectrum of B_z obtained from a two-dimensional simulation for the bulk Lorentz factor of $\Gamma = 1000$ ($V \sim c$). The time step and grid size are $\Delta t = 0.05\omega_{\rm pe}^{-1}$ and $\Delta x = \Delta y = 0.195c\omega_{\rm pe}^{-1}$, respectively, that is, $\omega_{\max} = 62.8\omega_{\rm pe}$ and $k_{x,\max} = k_{y,\max} = 16.1\omega_{\rm pe}/c$. The dashed curve represents the solution (2.30). We see that it fits the simulation results very well.

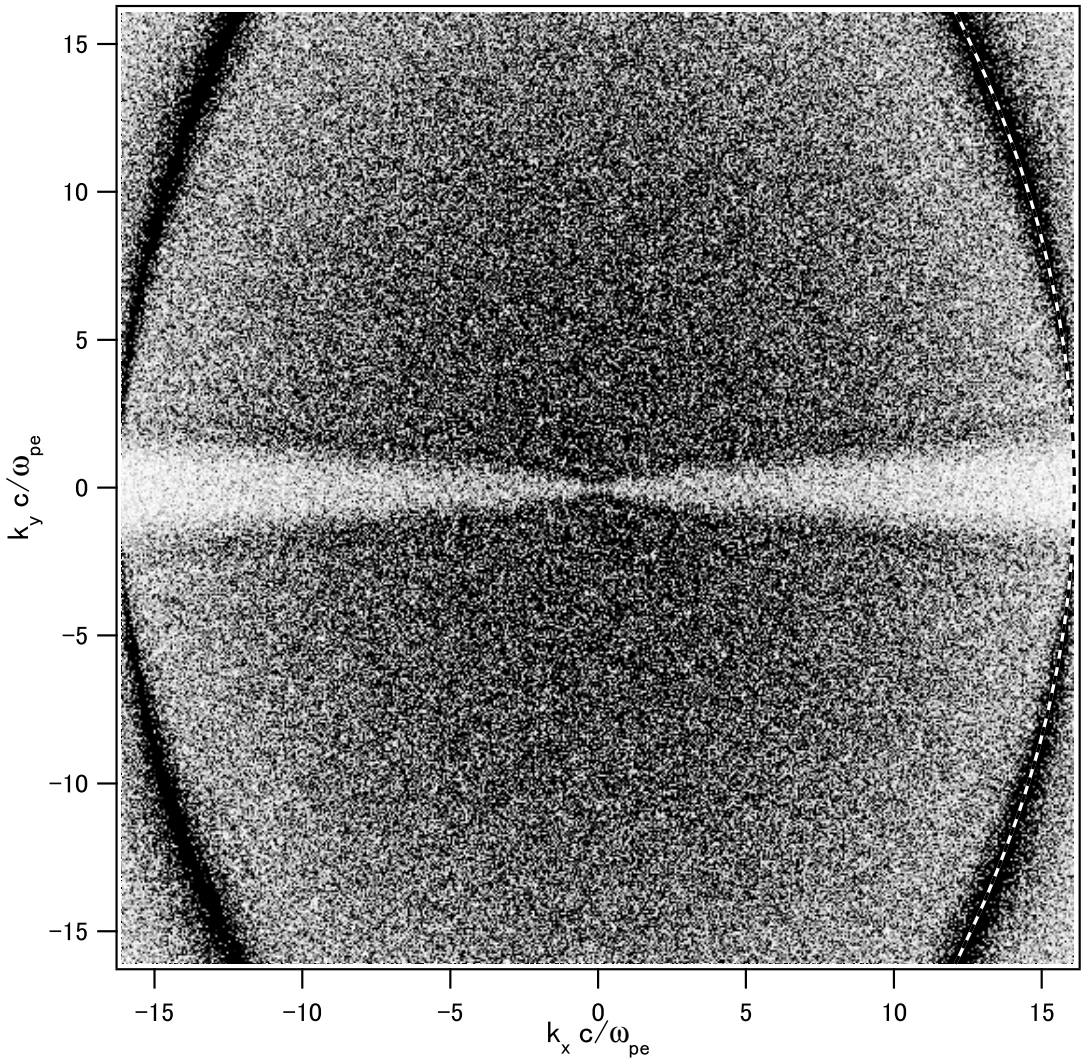

Figure 2.6: The power spectral density of B_z obtained from a two-dimensional simulation with a bulk Lorentz factor of $\Gamma = 1000$ as in figure 2.4 but for $\omega_{\max}/k_{\max} \sim 2.8$. The dashed curve shows the analytical solution (2.30).

The locations of the second or higher crossing points can be found in the same way, although they are generally dependent not only on $k_{x,\max}$ but also on $\omega_{\max}$. As already mentioned, since the first crossing point usually plays a dominant role in generating the numerical Cherenkov radiation in the present situation, we consider only it and do not take care of those higher crossing points in this paper.

2.4 A Practical Solution for the Numerical Cherenkov Radiation

From the solution (2.30), we see that the first crossing point is located in the region $k \geq k_{x,\max}$ for $V \sim c$, namely, for highly relativistic cases. Thus, one of practical solutions for such cases is to remove the spectral power of the current density for $k > k_{x,\max}$ by using an appropriate filter. Figure 2.7 shows the B_z obtained from simulations at time $t = 50\omega_{\rm pe}^{-1}$, (a) without filter and (b) with a filter in the wavenumber space defined by

$$f(k) = \begin{cases} \left[1 - (k/k_c)^{11}\right]^4 & \text{for } k/k_c < 1 \\ 0 & \text{for } k/k_c \geq 1, \end{cases} \tag{2.31}$$

where we take $k_c = 0.97 k_{x,\max}$. The numerical Cherenkov radiation is evident in (a), whereas it is not visible in (b).

The solution (2.30) also indicates that the location of the first crossing point however approaches $k = 0$ when decreasing the bulk velocity V. When V is small, the method using filters described above would not be an efficient solution because the cut-off at small wavenumber results in a serious loss in the spatial resolution of simulation. For such cases, one of practical solutions is using a higher-order shape factor to accelerate the decay of the large-wavenumber modes with $k > k_{x,\max}$ in the Fourier transform of the shape factor. However, since the magnitude of the current density also becomes small when V is small, the growth rate of the numerical Cherenkov radiation would become small, too.

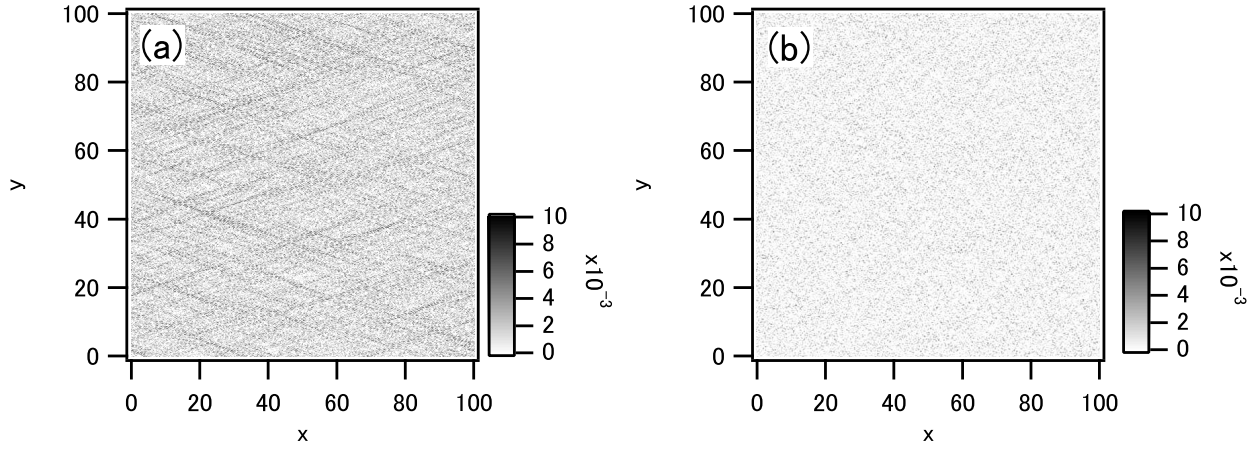

Figure 2.7: The magnetic field B_z obtained from two-dimensional simulations for a bulk Lorentz factor of $\Gamma = 1000$ and $\omega_{\max}/k_{\max} \sim 2.8$: (a) without filters, and (b) with a filter described in equation (2.31).

2.5 Conclusions

One of the causes of the numerical Cherenkov radiation in the PIC simulation is the numerically reduced speed of light. This problem can be solved by the exact spectral method which provides the correct phase velocity of the electromagnetic waves in vacuum for all wavenumbers (see figure 2.2).

There is another cause for the numerical Cherenkov radiation that involved with numerical aliasing effects. This alias problem is significant in case of relativistic bulk flow and there are two cases. When $\omega_{\max} < k_{\max}c$, the alias of the electromagnetic wave reflected at the $\omega = \omega_{\max}$ resonates with the relativistic particles (see figure 2.3 and 2.4). This case corresponds to $c\Delta t/\Delta x > 1$ and is impractical. The other case occurs even when $\omega_{\max} \geq k_{\max}c$, because the aliasing component of the shape factor, accompanied with the current fluctuation of the plasma flow, resonates with the electromagnetic wave (see figure 2.5). The amplitude of the aliasing component of the shape factor generally decreases with k, so the first crossing point with the dispersion relation of the electromagnetic wave in $\omega - k$ space leads to the most

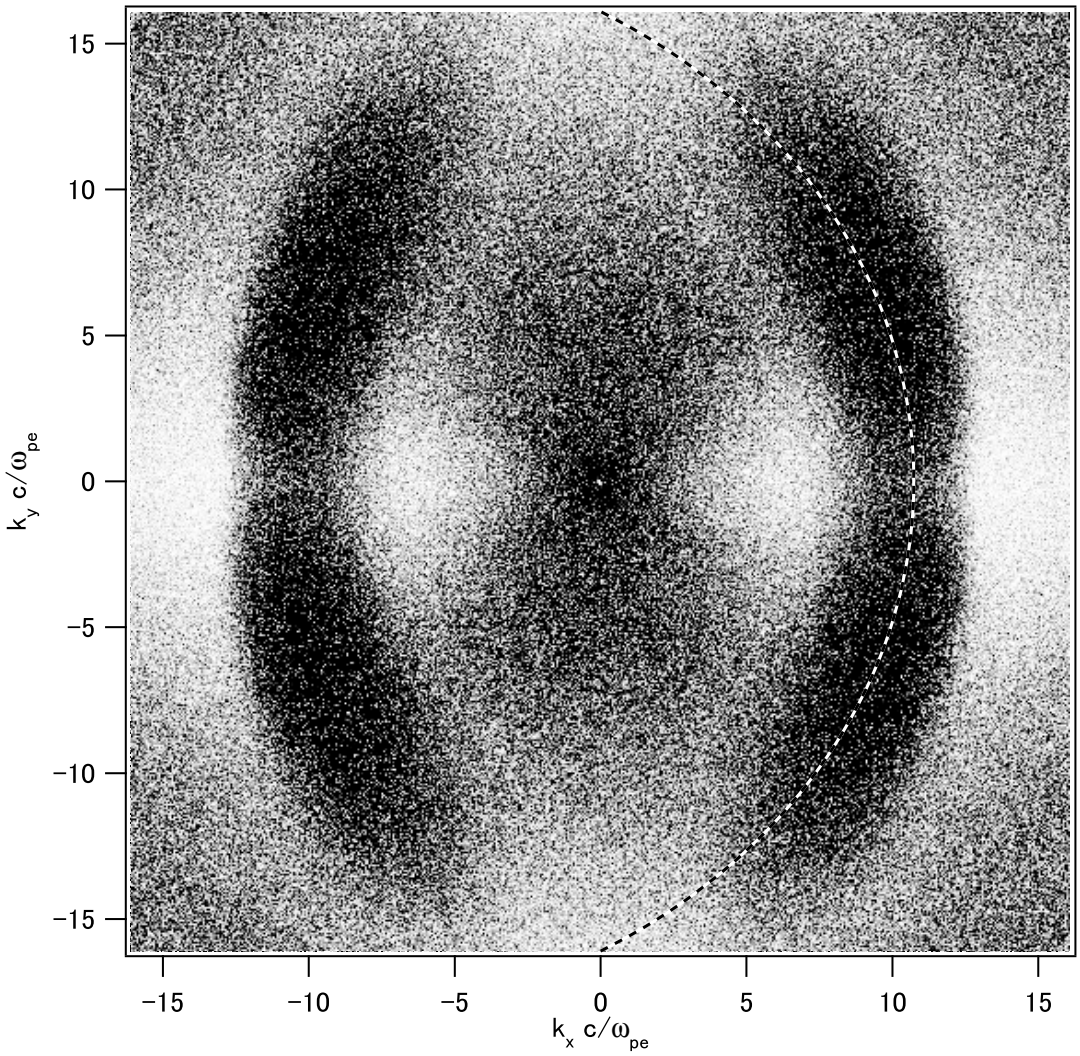

Figure 2.8: Same as in figure 2.6 but for a bulk velocity of $V = 0.5c$.

significant numerical Cherenkov radiation. The location of the first crossing point is described by equation (2.30). In highly relativistic cases, the first crossing points are almost located outside the radius of $k_{x,\max}$ as shown in figure 2.6, so cutting off the current density outside this radius in k-space with an appropriate filter removes the numerical Cherenkov radiation efficiently. In non-relativistic cases, the fluctuation of the current is relatively small, and growth of the numerical Cherenkov radiation may be negligible. However, in mildly relativistic cases, the growth cannot be negligible, and the first crossing point is hard to be eliminated by the method using filters without loosing the spatial resolution of simulation significantly, because the location is middle in the wavenumber space as seen in figure 2.8. For such cases, one of the ways to suppress the numerical Cherenkov radiation would be to use a higher order shape factor.

CHAPTER 3

Interaction between Current Sheets and a Shock in One Dimension

We investigate the interaction between alternating magnetic field with cold current sheets and a relativistic collisionless shock wave. Many kinds of high energy astrophysical objects may involve such alternating magnetic fields and a relativistic shock. They can be potent sources for the generation of high energy particles.

We found that a precursor wave, propagating from the shock front to upstream, accelerates a dense current sheet plasma in the upstream. In case that the width of the respective magnetic field reversal is larger than the downstream gyro-radius, the current sheet generates a large amplitude magnetosonic wave in the downstream by the collision with a shock front. The motional electric field accompanied with the magnetosonic wave can further accelerate the pre-accelerated particles, forming a non-thermal energy spectrum. In addition, the current sheet structure is stable against not only the collision but also compression by other current sheets.

In the thin current sheet case, which means the case that the width of the alternating magnetic field reversal is smaller than the downstream gyro-radius, the magnetic field dissipates and the magnetosonic wave excitation is absent. This result is applied to pulsar wind nebulae. The result of the dissipation could solve the σ problem.

3.1 Introduction

Although the non-thermal spectrum is a common feature in many astrophysical objects, the particle acceleration mechanism to form the non-thermal spectrum remains elusive. The elu-

cidation of the mechanism could resolve not only the spectrum on such objects, but also the cosmic ray power-law spectrum. Especially the acceleration process on highly relativistic astrophysical objects is effective to generate the ultra high energy cosmic rays (UHECR). Well known relativistic objects are AGNs ($\gamma \sim 10$), GRBs ($\gamma \sim 100$), and pulsar nebulae ($\gamma \sim 10^6$), where γ represents a bulk Lorentz factor of a jet (for AGN and GRB) or a stellar wind (for pulsar nebula). Usually such highly relativistic flows generate a shock wave due to an interaction with outer matter. So the acceleration at the shock is a reasonable scenario. Meanwhile magnetic reconnection is also a plausible mechanism as a particle acceleration process. A central engine of the relativistic astrophysical object with magnetic field may form alternating magnetic field structures in the flow by its rotational motion. Although the details of AGNs and GRBs are uncertain, the stellar wind from the pulsar manifests such a situation. The pulsar and its nebula are well studied by means of observational and theoretical approaches.

The Crab Nebula is a well observed pulsar nebula in broad band and in high resolution. Chandra X-ray observatory shows the double ring structure (Weisskopf et al., 2000). The inner ring generated by the interaction between the pulsar outflow and the supernova remnant is located about 0.1 pc from the center. This is believed as the location of a standing shock wave. Kennel and Coroniti (1984a,b) proposed a one-dimensional spherical MHD model (KC model) which suggesting that the ratio of magnetic field energy flux to kinetic energy flux (σ parameter) and bulk Lorentz factor of the upstream flow at the immediate shock upstream are 3×10^{-3} and 10^6, respectively. This means that the kinetic energy is dominant around the shock in contrast to the situation close to the light cylinder $\sigma \sim 10^4$, the so called "σ problem".

As mentioned above, the particle acceleration mechanism is also one of the open questions of the pulsar wind nebula. Indeed, the spectrum of the Crab Nebula exhibits highly non-thermal features (Aharonian and Atoyan, 1998; Mori et al., 2004). Because of the extremely high Lorentz factor of 10^6 of the flow, the toroidal magnetic field perpendicular to the flow direction is relativistically boosted. In such a perpendicular shock the diffusive shock acceleration, the standard theory of particle acceleration, is not an efficient mechanism. Some people previously engaged the particle acceleration mechanism by the highly relativistic perpendicular shock (e.g.

Gallant et al. (1992), Hoshino et al. (1992), Hoshino (2001)).

Although the KC model also neglected the magnetic field structure, the magnetic field polarity is alternating around the equatorial plane due to the magnetic pole precession of the pulsar (Michel, 1971). The structure of the pulsar wind propagates toward termination shock from the central pulsar (Coroniti, 1990; Lyubarsky and Kirk, 2001). The alternating magnetic field structure ("striped wind model") in the relativistic flow is favored as a means for solving both the σ problem and the particle acceleration problem. Kirk and Skjæraasen (2003) calculated a dissipation of the alternating magnetic field during the propagation with three dissipation processes: slow, fast and tearing mode instability. According to the article the magnetic field dissipation is insufficient to explain the σ value $\sim 3.0 \times 10^{-3}$, required by the KC model in case of a standard pair creation rate in the pulsar magnetosphere (Hibschman and Arons, 2001a,b). In this case the σ parameter is larger than 0.003 as suggested by the KC model. Lyubarsky (2003) showed analytically that current sheet dissipation at the shock front yields a consistent result with the KC model and also discussed the possibility of the particle acceleration. Therein the dissipation process is established by the alternating magnetic fields annihilating due to the magnetic reconnection driven by the strong compression from highly relativistic bulk pressure of the inflow. Lyubarsky (2003) has shown the generation of high energy particles under the assumption of an initial power-law spectrum. Such a power-law spectrum has been found previously by Zenitani and Hoshino (2001).

We investigate a general scenario of the interaction between alternating magnetic fields with cold current sheets and a perpendicular shock. Lyubarsky (2005) and Pétri and Lyubarsky (2007) studied a dissipation of the alternating magnetic field with relativistic hot current sheet plasma in the pulsar wind nebula by means of full particle simulations (PIC), see appendix A. Pétri and Lyubarsky (2007) found a criterion of the dissipation in the high-σ case. We focus on the possibility of the particle acceleration and magnetic field dissipation by checking a relatively low-σ case, $\sigma = 0.1$. Because it is impossible to describe these kinetic processes accurately by the MHD simulation, we also study by using full particle simulations. At first we precisely study the interaction between a single current sheet and a shock to analyze the particle acceleration

process, the magnetic dissipation process and other interesting properties. Furthermore, on the basis of these results, we investigate the interaction between multi current sheets and a shock. The predictions by the previous works are compared with our results. We anticipate the application to the astrophysical phenomena.

3.2 Simulation Condition

We use a relativistic one-dimensional Particle-in-Cell code (Birdsall and Langdon, 2005). Magnetized cold electron-positron plasma is injected from the left boundary. The magnetic field consists of a component (B_z) perpendicular to the flow direction (x). The electric field has a motional (E_y) and a static component (E_x). Particle velocity components are in x and y directions. The right boundary reflects particles and electro-magnetic field. The reflecting wall triggers the creation a perpendicular shock which propagates leftward. Therefore the simulation is in the shock downstream frame. The combination of particle bulk motion and electro-magnetic field of the injection flow satisfies the force-free condition and its bulk kinetic energy has a Lorentz factor of 100. Now we set the injection magnetization parameter $\sigma_0 = B_0^2/(8\pi n_0 \gamma_0 mc^2) = 0.1$, where B_0 is the magnetic field, n_0 is the number density of electron (positron), γ_0 is injection bulk Lorentz factor. All of them are the parameters in the downstream frame. The σ_0 is also described by a symbolic plasma frequency $\omega_{p0} = \sqrt{8\pi n_0 e^2/(m\gamma_0)}$ and a gyro-frequency $\Omega_{g0} = eB_0/(\gamma_0 mc^2)$,

$$\sigma_0 = \frac{\Omega_{g0}^2}{\omega_{p0}^2}. \tag{3.1}$$

The time and space scale is normalized by ω_{p0} and c/ω_{p0} in the following simulations, respectively. It is important to note that these do not exactly correspond to the plasma frequency and the gyro-frequency in the downstream.

The electro-magnetic field is solved with an advection form (Birdsall and Langdon, 2005). The grid size and the time step are $\Delta x \leq 0.01 c/\omega_{p0}$ and $\Delta t = \Delta x/c$, respectively. Each cell contains more than 50 particles to ensure statistical accuracy. The injection current sheets are given by the relativistic Harris solution (Hoh, 1966; Kirk and Skjæraasen, 2003). Then the

current sheet width λ_{cs0} is defined by $B(x) \propto \tanh(x/\lambda_{cs0})$. The λ_{cs0} is resolved by more than 20 grids. Plasma inside the current sheet is the same temperature as the cold outer plasma $T_0 = 0.005mc^2$. The above magnetic field and current sheet temperature, described by σ_0 and T_0, determine the number density of the current sheet plasma $n_{cs} = 10n_0$ via the pressure balance,

$$\sigma_0' = 2\frac{n_{cs0}'}{n_0'}\ \frac{T_0}{mc^2}, \tag{3.2}$$

where the parameters with a prime and the temperature T_0 is in the upstream frame. The hyperbolic tangent magnetic field is smoothly connected to the outer constant one to avoid numerical noise. Then the Harris current sheet region is kept $5\lambda_{cs0}$ for each side, $\delta B_0/B_0 = 1 - \tanh(5) \sim 10^{-4}$, which is sufficiently accurate.

3.3 Single Current Sheet Injection

In this section the focus is on the interaction between a shock and a single current sheet with the width of $\lambda_{cs0}(c/\omega_{p0})^{-1} = 0.01, 0.1, 1, 10$, called CASE1-4 respectively. We will show the simulation results and the analysis of the observed phenomena, and will discuss as an elementary process of the interaction between a fast mode shock and a tangential discontinuity.

3.3.1 Simulation Result

Figure 3.1 shows the simulation results concerning the Lorentz factor of the particles, perpendicular electro-magnetic field, number density and average Lorentz factor in the whole simulation box. Since the positive and negative particles are positrons and electrons, respectively, in our simulations, each particles behave symmetric. So the following plots for particles show only the positrons. Furthermore, because of the symmetry argument, the electrostatic field growth is limited. We do not discuss this in detail and therefore do not plot it in figures.

One can identify the fast shock fronts at $x = 115c/\omega_{p0}$, $120c/\omega_{p0}$, $120c/\omega_{p0}$ and $510c/\omega_{p0}$, for CASE1, CASE2, CASE3 and CASE4, respectively. The shock front propagates leftward with

$\sim 0.5c$ which is consistent with the Rankine-Hugoniot relations in the shock downstream frame applying the ratio of specific heats $\Gamma = 3/2$, i.e. for an ideal two-dimensional gas. The left region of the shock front is the upstream. The X-mode wave, called precursor, propagates leftward from the shock front with $\sim c$, in detail discussed by Gallant et al. (1992). In the downstream, which is the region to the right of the shock front, the alternating magnetic field injected from the upstream remains a tangential discontinuity at $x = 134c/\omega_{p0}$. The downstream parameters are almost consistent with the Rankine-Hugoniot relations except around the magnetic neutral sheet. Although all four cases share these characteristics, a large amplitude magnetosonic wave propagating rightward in the downstream is clearly emerging only in CASE3 and CASE4 at $x = 180c/\omega_{p0}$ and $780c/\omega_{p0}$, respectively.

3.3.2 Excitation of a Magnetosonic Wave

In Figure 3.1 the magnetosonic wave is seen clearly for CASE3 and CASE4, but not for CASE1 and CASE2. This result is also shown in non-relativistic simulations (Tsubouchi and Matsumoto, 2005; Haruki et al., 2006) The reason is that the magnetosonic wave is excited by compression of the shock front by a large bulk energy, or momentum, of the dense current sheet plasma (see appendix C). Its counteraction remnants after the interaction with the shock front is a low temperature current sheet plasma.

In all four cases shown in Figure 3.2, the average Lorentz factor in the magnetic neutral sheet, where $x = 136c/\omega_{p0}$, $135.5c/\omega_{p0}$, $133 - 135c/\omega_{p0}$ and $615 - 650c/\omega_{p0}$ for each cases, is smaller than the outer region. Let's compare the temperature from the simulation results with that from the Rankine-Hugoniot relations. One can generally obtain the temperature from the average Lorentz factor on the assumption that the particle energy distribution is a two-dimensional isotropic Maxwellian. For the four-velocity $\boldsymbol{u} = (u_x, u_y)$,

$$\begin{aligned} \langle\gamma\rangle &= \frac{\int_{-\infty}^{\infty}\int_{-\infty}^{\infty}\gamma(\boldsymbol{u})f(\boldsymbol{u})du_x du_y}{\int_{-\infty}^{\infty}\int_{-\infty}^{\infty}f(\boldsymbol{u})du_x du_y} \\ &= \frac{2\left(T/mc^2\right)^2 + 2T/mc^2 + 1}{T/mc^2 + 1} \end{aligned} \tag{3.3}$$

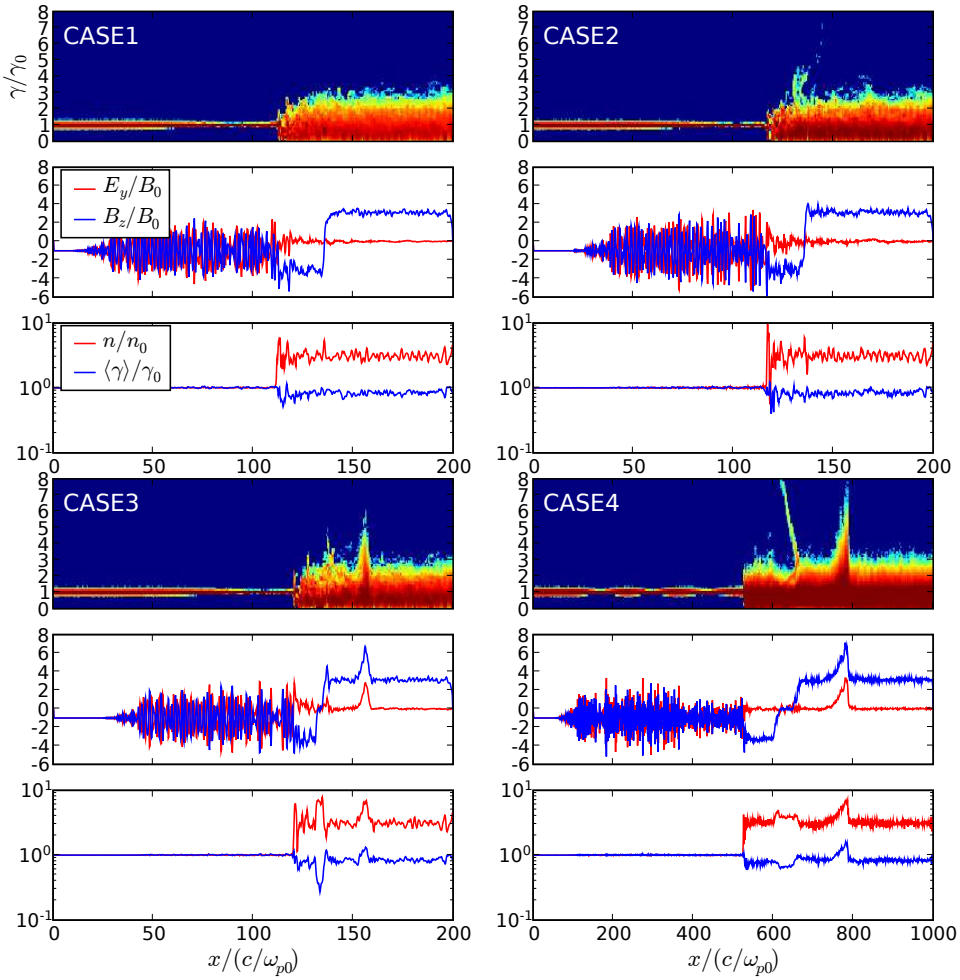

Figure 3.1: Simulation results corresponding to CASE1-4. Each of them consists of three plots which show particle Lorentz factor γ (contour plot), electro-magnetic field E_y, B_z (red and blue lines, respectively), number density n and average Lorentz factor $\langle\gamma\rangle$ (red and blue lines, respectively). All of these physical quantities are normalized by their initial value, are plotted as function of space in unit of c/ω_{p0}.

where $f(\boldsymbol{u})$ is a two-dimensional relativistic Maxwellian, $f(\boldsymbol{u}) \propto \exp(-\gamma(\boldsymbol{u})mc^2/T)$. In our simulations, the temperature comparable to the injection energy is highly relativistic, $T/(mc^2) \sim \gamma_0 = 100 \gg 1$, so equation (3.3) is approximated by $\langle\gamma\rangle \simeq 2T/(mc^2)$. Using this relation and the average Lorentz factors from the simulation as shown in Figure 3.2 or Table 3.1, the temperature inside the magnetic neutral sheet by the simulation results is estimated for CASE1-4 as $T_{cs}/\gamma_0 mc^2 = 0.39, 0.30, 0.19$ and 0.33, respectively. On the other hand, one can also estimate the downstream temperature via the Rankine-Hugoniot relations (Kennel and Coroniti, 1984a; Gallant et al., 1992). According to the relations, the temperature is $T_{cs}/(\gamma_0 mc^2) = 0.5$ by using $\sigma_0 = 0$. This value is inconsistent with the simulation results. The reason is that the bulk energy of the upstream current sheet plasma does not convert into thermal energy as much as described by the Rankine-Hugoniot relations. The residual energy works pushing the shock front and excites a magnetosonic wave.

Identifier	λ_{cs0}	λ_{cs}	$\langle\gamma\rangle$
CASE 1	0.01	0.74	0.77
CASE 2	0.1	0.65	0.60
CASE 3	1	1.7	0.37
CASE 4	10	30	0.66

Table 3.1: The current sheets width before (λ_{cs0}) and after (λ_{cs}) the collision with a shock, and the average Lorentz factors $\langle\gamma\rangle$ on the magnetic neutral sheet in the downstream (see Figure 3.2).

3.3.3 High Energy Particles

Around the magnetosonic waves for CASE3 and CASE4 in Figure 3.1, we can observe strongly accelerated particles. This is basically well explained by the first adiabatic invariant,

$$\mu = \frac{u^2}{B_z}. \tag{3.4}$$

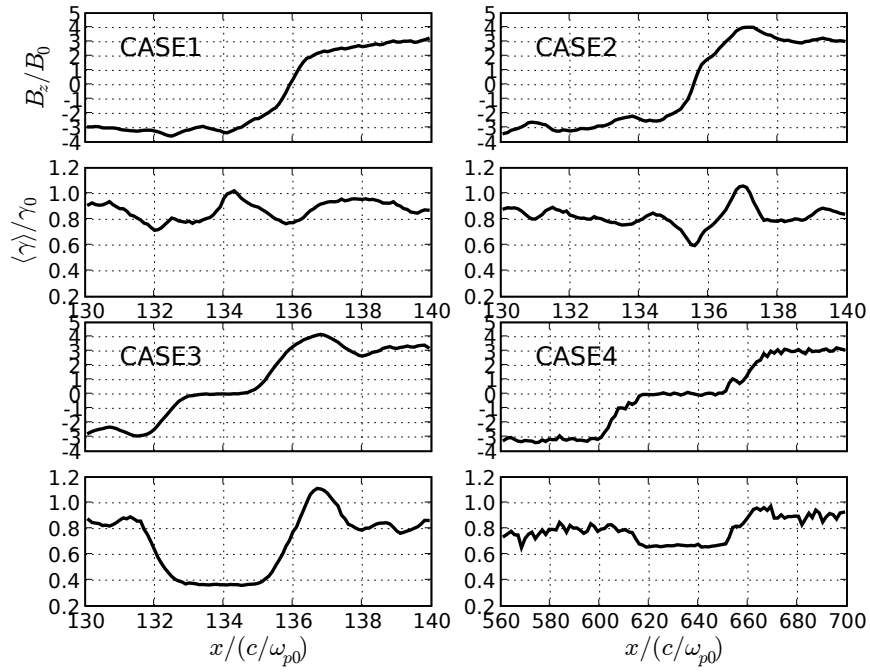

Figure 3.2: Alternating magnetic field and average Lorentz factor for CASE1-4 in the downstream. They are averaged by 50 snapshots for $25\omega_{p0}^{-1}$ in CASE1-3 and for $125\omega_{p0}^{-1}$ in CASE4. The longitudinal axis parameters are normalized by their initial value. The space scale (x) is normalized by c/ω_{p0}

The four-velocity u is a component perpendicular to the magnetic field B_z. The particle energy restores to its original value after passing the wave, so this high energy feature does not yield continuous acceleration. However this explanation is invalid for very high energy particles, whose gyro-radius is larger than the wavelength scale, at the outside of the wave, because the conservation of the adiabatic invariant is invalid. We will discuss later that non-thermal particles are generated during the multi-current sheet interaction.

Another important agent for particle acceleration is seen inside the magnetic neutral sheet in CASE4. They are trapped by the outer magnetic field and meander in the neutral sheet. They got energy from the precursor before the current sheet collides with the shock front. Let us discuss about this acceleration mechanism. We think that the interaction between the precursor wave and the current sheet plays an important role on the acceleration through the action of the precursor wave pressure.

Gallant et al. (1992) showed that the precursor frequency has a lower limit defined by the shock energy,

$$\omega \geq \omega_L = \gamma_{shock}\omega_{p0}. \tag{3.5}$$

In our simulations the Lorentz factor of the shock is $\gamma_{shock} = 1.21$ for $\sigma_0 = 0.1$, so the lower limit of the frequency is $\omega_L = 1.21\omega_{p0}$. On the other hand the dispersion relation of the precursor in a highly relativistic flow (Gallant et al., 1992) is

$$\left(\frac{ck}{\omega}\right)^2 \simeq 1 - \frac{\omega_p^2}{\omega^2} = 1 - \frac{n}{n_0}\frac{\omega_{p0}^2}{\omega^2}, \tag{3.6}$$

where n is the number density inside the current sheet, $n_0 \leq n \leq n_0 + n_{cs0}$. If the number density is larger than this criterion, the precursor cannot propagate in the plasma, $(ck/\omega)^2 < 0$, which means a cut-off. Using equation (3.5) and equation (3.6), one can get the density range which yields the cut-off of the precursor,

$$\frac{n}{n_0} > \frac{\omega^2}{\omega_{p0}^2} \geq \frac{\omega_L^2}{\omega_{p0}^2} = 1.46. \tag{3.7}$$

Since the maximum density of the current sheet plasma in our simulation is $n_{cs0} = 10n_0$, frequencies of the precursor wave consistent with equation (3.7) are partially reflected by the

current sheet plasma and gives its momentum to the dense plasma. Then the precursor pushes the dense plasma and disturbs the Harris equilibrium. As a result a part of the upstream plasma begins a gyro motion. These particles show high energy in the downstream frame, because a gyro-motion along the x-direction in the upstream frame is boosted by γ_0 in the downstream frame. The other plasma is thermalized by a non-equilibrium motion under the perturbed pressure balance. The gyrating plasma is seen as a high energy one of CASE4 in Figure 3.1. These effects can form the non-thermal energy spectrum. We will discuss it in section 3.4.2 in more detail. Although the simulation time scale of CASE1-3 is too short to see the acceleration, we confirmed the acceleration in such thin current sheet cases by longer simulations (not shown here).

The current sheet plasma density depends on its temperature and the outside magnetic pressure, or σ parameter, see equation (3.2). Therefore, in case that a relativistic hot current sheet and a low σ make the current sheet plasma to be low in density, the above effect is not expected.

3.3.4 Expansion of the magnetic neutral sheet by the thermalization

How does the magnetic neutral sheet width change before and after the collision? Since the alternating magnetic field profile in the downstream is not always fitted by a simple analytical function such as a hyperbolic tangent in the downstream (see Figure 3.2), we define the width of the magnetic neutral sheet λ_{cs} as a half width of the region $\left\{x \middle| |B(x)|/B_1 \leq \tanh(1) \simeq 0.76\right\}$, where B_1 is the downstream magnetic field predicted by the Rankine-Hugoniot relations. In CASE1 and CASE2 those magnetic neutral sheets of λ_{cs} strongly expand, compared with λ_{cs0} (see Table 3.1). On the other hand the magnetic neutral sheets in CASE3 and CASE4 do not expand so much. In principle the change of the width is the result of the thermalization of the plasma around the magnetic neutral sheet, based on the pressure balance (see equation (3.2)). The sources of the thermal energy are mainly the upstream bulk energy or the magnetic field energy around the magnetic neutral sheet. Now we estimate the expansion on the assumption that the source is only the upstream bulk energy with no absorption by the magnetosonic

wave and with no injection by the precursor. First, the pressure outside the neutral sheet is calculated by the Rankine-Hugoniot relations,

$$\frac{P_{out}}{n_0\gamma_0 mc^2} = \frac{n_1 T_1}{n_0\gamma_0 mc^2} + \frac{B_1^2}{B_0^2}\sigma_0 = 2.1. \tag{3.8}$$

On the other hand the pressure of the plasma around the magnetic neutral sheet can be expressed as

$$\frac{P_{in}}{n_0\gamma_0 mc^2} = \frac{n_{cs} T_{cs}}{n_0\gamma_0 mc^2}. \tag{3.9}$$

The temperature is $T_{cs}/(\gamma_0 mc^2) = 0.5$ at most. Then, the pressure balance, $P_{out} = P_{in}$ from equation (3.8) and equation (3.9), requires the density around the magnetic neutral sheet of $n_{cs}/n_0 = 4.1$. If the net exchange of the particles between inside and outside the magnetic neutral sheet is not significant, the relation of the density and the width is

$$\frac{n_{cs0}}{n_0}\lambda_{cs0} \sim \frac{n_{cs}}{n_0}\lambda_{cs}. \tag{3.10}$$

Therefore the expected expansion ratio is $\lambda_{cs}/\lambda_{cs0} \sim 2.4$. For CASE 1 and CASE2, however, the expansion ratio is 74 and 6.5 in spite of no energy injection by the precursor. This means that the magnetic field dissipation accounts for the major share of the thermalization, even if energy absorption by the magnetosonic wave excitation is not effective.

For CASE3, there is no energy injection by the precursor but has the energy absorption effect by the magnetosonic wave excitation, the expansion ratio (= 1.7) is less than 2.4. For CASE4, which has the precursor effect and the magnetosonic wave effect, the expansion ratio (= 3.0) is more than 2.4, and the reason for larger expansion than in CASE3 is the additional thermalization by the precursor. Anyhow the magnetic dissipation for CASE3 and CASE4 does not contribute large proportions to thermalize the plasma in the magnetic neutral sheet, unlike CASE1 and CASE2.

Then the final width in CASE1 and CASE2 is comparable to each other, even though the difference of the initial value is ten times. What determines the width? The typical gyro-radius in the downstream can be approximated by combining the upstream bulk flow and the

downstream gyro-frequency,

$$\frac{R_g}{c/\omega_{p0}} = \frac{\langle\gamma\rangle/\gamma_0}{\sqrt{\sigma_0}B_1/B_0} = 1.1\frac{\langle\gamma\rangle}{\gamma_0}, \tag{3.11}$$

where we used a parameter $B_1/B_0 = 2.8$ for $\sigma_0 = 0.1$. If one substitutes the quantity $\langle\gamma\rangle$ of the neutral sheet in Table 3.1 into equation(3.11), the typical gyro-radius of the current sheet plasma for CASE1 and CASE2 is $0.88c/\omega_{p0}$ and $0.68c/\omega_{p0}$, respectively. These results agree with each alternating magnetic field width λ_{cs} in Table. 3.1. Therefore the thin current sheet may expand to the downstream gyro-scale, although this discussion lacks the proof to explain the dissipation process on the basis of the plasma kinetic theory.

3.4 Multi Current Sheet Injection

This section is divided into two parts. One is a thin current sheet case, like CASE1 and CASE2 in the section 3.3. As we have shown in the section 3.3.4, a thin current sheet expands to the scale of gyro-radius R_g predominantly by thermalization via the magnetic field dissipation predominantly. In the multi current sheet case, we expect the annihilation by the expansion and overlapping with subsequent one.

For the case of the thick current sheet, because the magnetic dissipation effect is weak, the alternating magnetic field structure would be stable and sheets will not annihilate, unlike the thin current sheets case. However, we will discuss another important effect by a number of large amplitude magnetosonic waves and the possibility of the additional particle acceleration by the waves. Although in the single current sheet case the alternating magnetic field does not dissipate so much by collision with a shock front, in this case there will be additional compressions via magnetosonic waves by continuous collisions of the other current sheets. We will also check the stability of the downstream current sheet against the compressions.

3.4.1 Thin Current Sheet

As we showed in the section 3.3.4, a thin current sheet expands to the scale of a gyro-radius R_g. Such current sheets would be annihilated by overlapping. We simulated thin current sheets injection into a shock to check this prediction. The current sheet width is $\lambda_{cs0} = 0.01c/\omega_{p0}$, same with CASE1, and each clearance is $0.2c/\omega_{p0}$, which is smaller than the downstream current sheet width of CASE1, $0.77c/\omega_{p0}$. Left plots in Figure 3.3 show the simulation result. Clearly there is no shock structure, but just a counter-streaming in the u_x plot. This result is similar to the case of no magnetic field. Because the alternating magnetic field interval is much smaller than the gyro-radius R_{g0}, the Lorentz force changes its direction before particles complete gyro-motion defined by the magnetic field amplitude and the Lorentz factor of their bulk motion. As a result the particles do not feel magnetic field on the average, and are not affected by the Lorentz force. Then the injected particles reflected at the right boundary are not thermalized but just flow leftward. Although in the one dimensional case a shock is not formed within the PIC simulation scale, Kato (2007) showed that multi-dimensional PIC simulation can generate a shock by the Weibel instability (Weibel, 1959; Kato, 2005). So the shock would also be generated in this case in a multi-dimensional simulation.

The pulsar wind close to the equatorial plane includes current sheets spaced equally, but the polarity is biased at high latitude (Bogovalov, 1999). We also simulate such a case (right plots in Figure 3.3). The magnetic field structure is shown in the top of the figure. In this case, since the average magnetic field is not zero, particles complete the gyro-motion and generate a shock, see Figure 3.3. The electro-magnetic field plot (E_y, B_z) shows that the alternating magnetic fields completely disappear at the shock front. This is consistent with the prediction from the single current sheet case. Upper plot in Figure 3.4 shows a comparison of the total Poynting energy between the alternating magnetic field inflow and the uniform one. In contrast to the uniform case, the Poynting energy does not increase so much for the alternating magnetic field case. This means that the alternating magnetic field dissipates and gives its energy to the particles. The shock downstream parameters meet the Rankine-Hugoniot relations evaluated by using an average of the upstream magnetic field, $\langle B_z \rangle = 0.5B_0$. The energy spectrum has

a small amount of high energy particles. In this case the current sheet scale is less than the gyro-radius. Then the motional electric field, which accelerates particles, can not be generated continuously on such a thin scale.

Lyubarsky (2003) assumed a power-law spectrum to evaluate particle acceleration by magnetic reconnection (Zenitani and Hoshino, 2001). The acceleration is accomplished by particles flowing into the current sheet and running along the reconnection electric field. In the Crab pulsar case, however, the current sheet clearance is about the light cylinder $\sim$ 1600km, and the gyro-radius in the downstream is $\sim 1.7 \times 10^8$km by using a particle Lorentz factor $\sim 3 \times 10^6$ (Kennel and Coroniti, 1984a,b) and the magnetic field $\sim 3 \times 10^{-4}$G (Marsden et al., 1984). Because the current sheet width must be smaller than their clearance, the width is much smaller than the gyro-radius. In such a kinetic scale, similar to the above simulation, particles are not trapped in the magnetic neutral sheet, and also do not generate an accelerating electric field. Therefore the particle acceleration by magnetic reconnection would not work in the termination shock of the Crab pulsar nebula.

3.4.2 Thick Current Sheet

We also performed a simulation of current sheets with a width of $\lambda_{cs0} = 3.2c/\omega_{p0}$ and each clearance of $50c/\omega_{p0}$ colliding with a shock. In this case the sheet width ($1.1c/\omega_{p0}$) are larger than the typical gyro-radius of the downstream plasma. To avoid right boundary effects where a magnetosonic wave reaches the right boundary and is reflected, we set the spacing of an uniform shock downstream by injecting an uniform inflow in the early phase. After that current sheets are injected. Figure 3.5 shows a part of the simulation result. In this figure a shock front is located at $x = 520c/\omega_{p0}$. The precursor propagates leftward from the shock front. Ten current sheets have already interacted with the shock front and stay in the region from the shock front to $x = 720c/\omega_{p0}$. Five magnetosonic waves generated by the interactions are propagating in this region, and the other five are already in the uniform downstream region from $x = 720c/\omega_{p0}$ rightward (see also Figure 3.6). The current sheets in the downstream survive despite the compression by bumping from behind by the other current sheets. Because the compressions

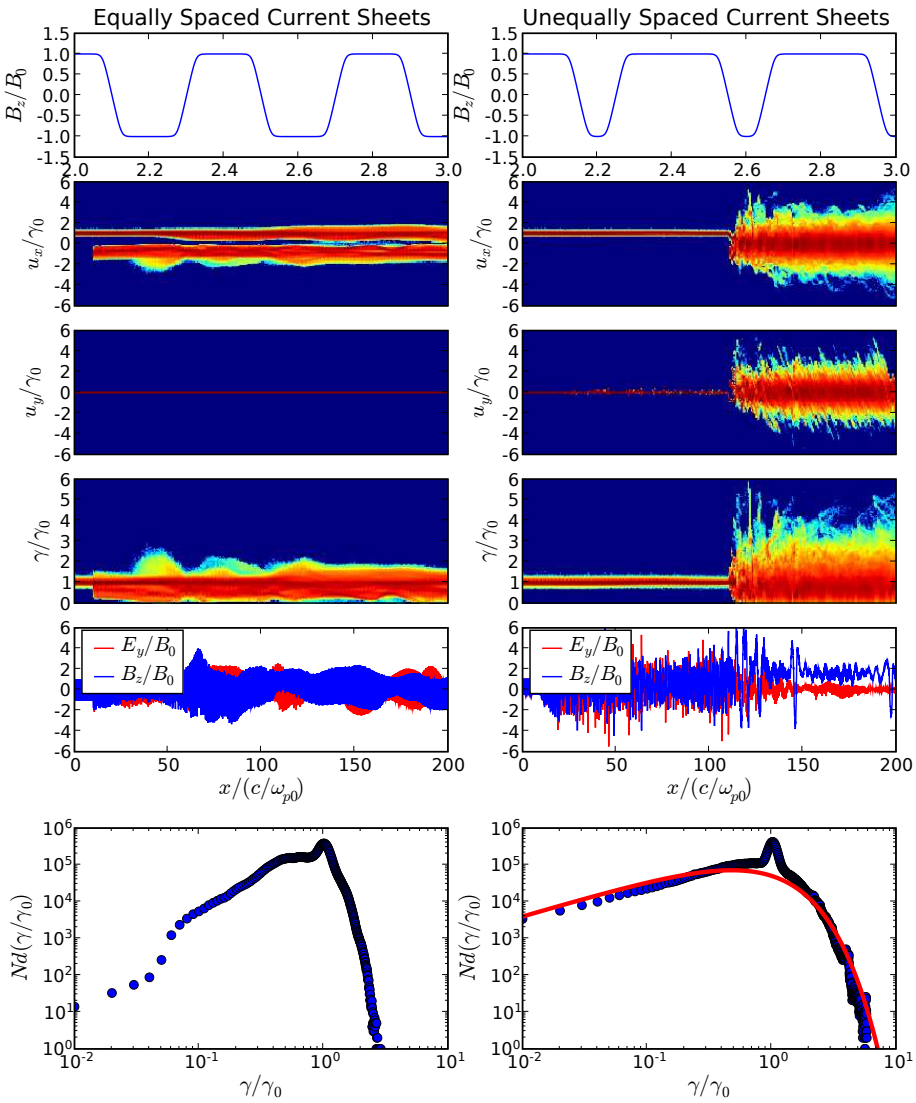

Figure 3.3: The simulation result for thin current sheets with narrow clearance. The space scale x is normalized by c/ω_{p0} and the other parameters are by their respective initial value. For the left plots, each current sheet is spaced equally, so the average magnetic field is zero. For the right, the clearance is alternately shifted, and the average is 0.5, see the right top plot. The contour plots show particle four-velocity and normalized Lorentz factor. Plots just below these show the electro-magnetic field. The bottom ones are the particle energy spectrum in the whole simulation box, and the red line shows a relativistic Maxwellian.

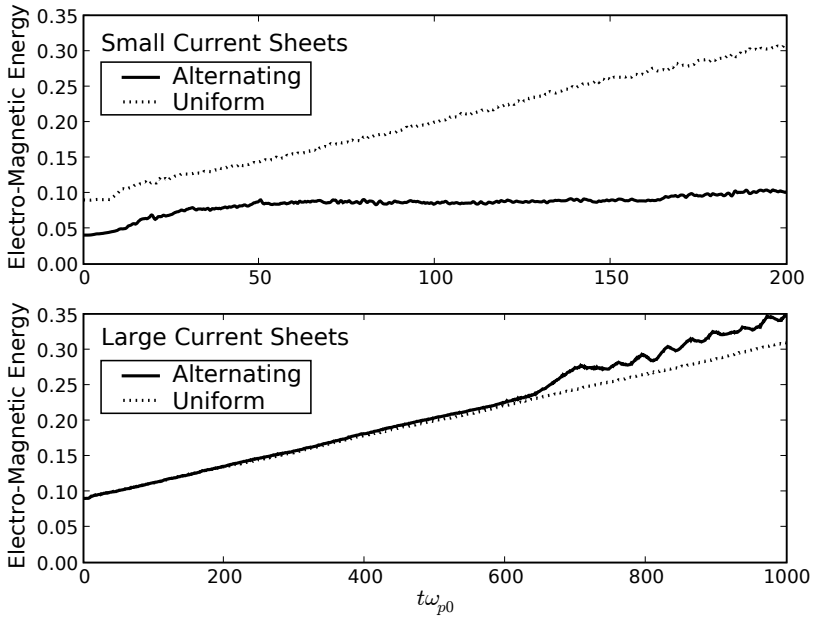

Figure 3.4: Electro-magnetic energy history for the thin current sheet case (top) and the thick current sheet case (bottom). They are normalized by the total energy in the simulation box. The injection energy of particles and electro-magnetic field is subtracted. For comparison no alternating magnetic field case, called "Uniform", is also plotted as solid line.

are carried as magnetosonic waves, it also affects a current sheet separate from the shock front. The bottom panel of Figure 3.4 shows the electro-magnetic energy history. After the first current sheet collision with a shock front at $x = 710/\omega_{p0}$, the electro-magnetic energy enhancement by magnetic field compression dominates the decrease by the magnetic field dissipation. These results mean that the current sheet structure is quite stable at least in one dimension. In the multi-dimensional case one can suggest that a current sheet would dissipate easily by the tearing or drift kink instability (Zenitani and Hoshino, 2005), driven by the compression. If the tearing mode dominates the drift kink mode, the particles could be accelerated by magnetic reconnection, which may contribute to the production of non-thermal particles.

The particle energy spectrum in Figure 3.5 shows a peak at $\gamma/\gamma_0 \sim 0.1$ and a break at $\gamma/\gamma_0 \sim 1$, normalized by the initial value $\gamma_0 = 100$. The peak is attributed to the relatively cold plasma within the magnetic neutral sheet in the downstream, discussed in the section 3.3. The energy region above the break point shows a power-law spectrum with an index 4.

In the left plots of Figure 3.5, one can see the high energy particles in the downstream, from the shock front ($x = 520c/\omega_{p0}$) to the boundary of the uniform region ($x = 720c/\omega_{p0}$). The most strongly accelerated particles of them are accelerated by the precursor in the upstream and by the magnetosonic waves in the downstream. Figure 3.6 shows a stack plot of the magnetic field, three particle trajectories and their energy histories. In the left plot a shock front with an uniform downstream propagates from $(x(c/\omega_{p0})^{-1}, t\omega_{p0}) = (770, 500)$ to $(670, 710)$ where the first current sheet collides with the shock front. After that the shock front moves from $(x(c/\omega_{p0})^{-1}, t\omega_{p0}) = (670, 710)$ to $(520, 1000)$, and the tangential discontinuity between current sheet plasma and the uniform one moves from $(x(c/\omega_{p0})^{-1}, t\omega_{p0}) = (670, 710)$ to $(720, 1000)$ due to compressions by the magnetosonic waves. The fluctuation in the left of the shock front is the precursor.

The two particles, shown by red and blue lines, gain energy for the first time in the upstream precursor region, $t\omega_{p0} = 770 - 830$ for the red line and $t\omega_{p0} = 650 - 700$ for the blue line. These particles loose energy at the beginning of the acceleration, because the precursor pushes them from the anti-flow direction. This detail was discussed in the section 3.3.3. Furthermore these

particles substantially gain or loose their energy by interactions with the magnetosonic waves. A part of the particles which gain energy at the moment form the high energy end of the spectrum. The energy gain (or loss) by a brief interaction by the magnetosonic wave can be evaluated as follows,

$$\Delta\gamma \approx \gamma_i \frac{v_y}{c} \frac{E_y}{B_z} \left(\Omega_{gi}\Delta t\right), \tag{3.12}$$

where γ_i is the Lorentz factor before the interaction and $\Omega_{gi} = qB_z/(\gamma_i mc^2)$ is roughly its gyro-frequency. v_y/c means the injection phase of the particle gyro-motion and determines that the particle energy gain or loss. In other words, the particle gain energy by running along the motional electric field. The important thing is that the energy variation is proportional to the initial energy γ_i. So the pre-acceleration by the precursor has an important role to generate higher energy by the interaction with the magnetosonic wave. Furthermore in order to achieve the acceleration, the magnetosonic wave amplitude should be large so that the group velocity is nearly light velocity, which means that the motional electric field is roughly equal to the wave component of the magnetic field in the downstream frame.

In contrast a particle shown by green lines does not change its energy significantly by over-passing the magnetosonic waves, because the particle has not gained energy from the precursor before the interaction with the magnetosonic waves and so its energy variation is small as suggested by equation (3.12). Such low energy particles have relatively small gyro-radius and tend to conserve the first adiabatic invariant, see section 3.3.3.

3.5 Summary and Discussion

We have studied interactions between alternating magnetic fields with a cold current sheet and a shock front by using a relativistic one-dimensional Particle-in-Cell code. We found that the interaction excites a large amplitude magnetosonic wave, and the precursor and the magnetosonic wave accelerate particles.

First, we simulated a single current sheet collision with a shock front for four cases of the current sheet width. As one of the common points, the precursor gives a part of momentum to

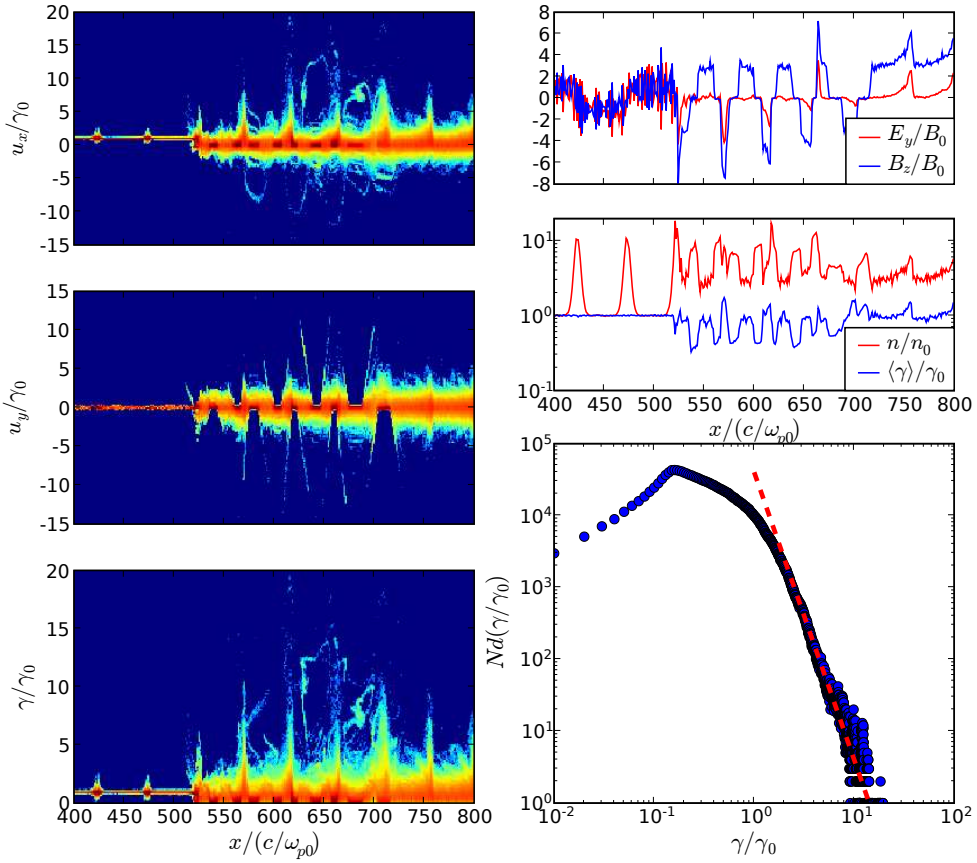

Figure 3.5: Local feature of interactions between a shock and thick current sheets. Left three contour plots shows four-velocity u_x, u_y and Lorentz factor γ. The right upper two show electro-magnetic field E_y, B_z, number density n and average Lorentz factor $\langle\gamma\rangle$. Their abscissa axis are space coordinate normalized by c/ω_{p0} and their ordinate axis are normalized by their initial value. The right bottom plot shows particle energy spectrum. The abscissa axis is Lorentz factor normalized by an injection value, $\gamma_0 = 100$. The red dashed line shows a power-law spectrum with index 4.

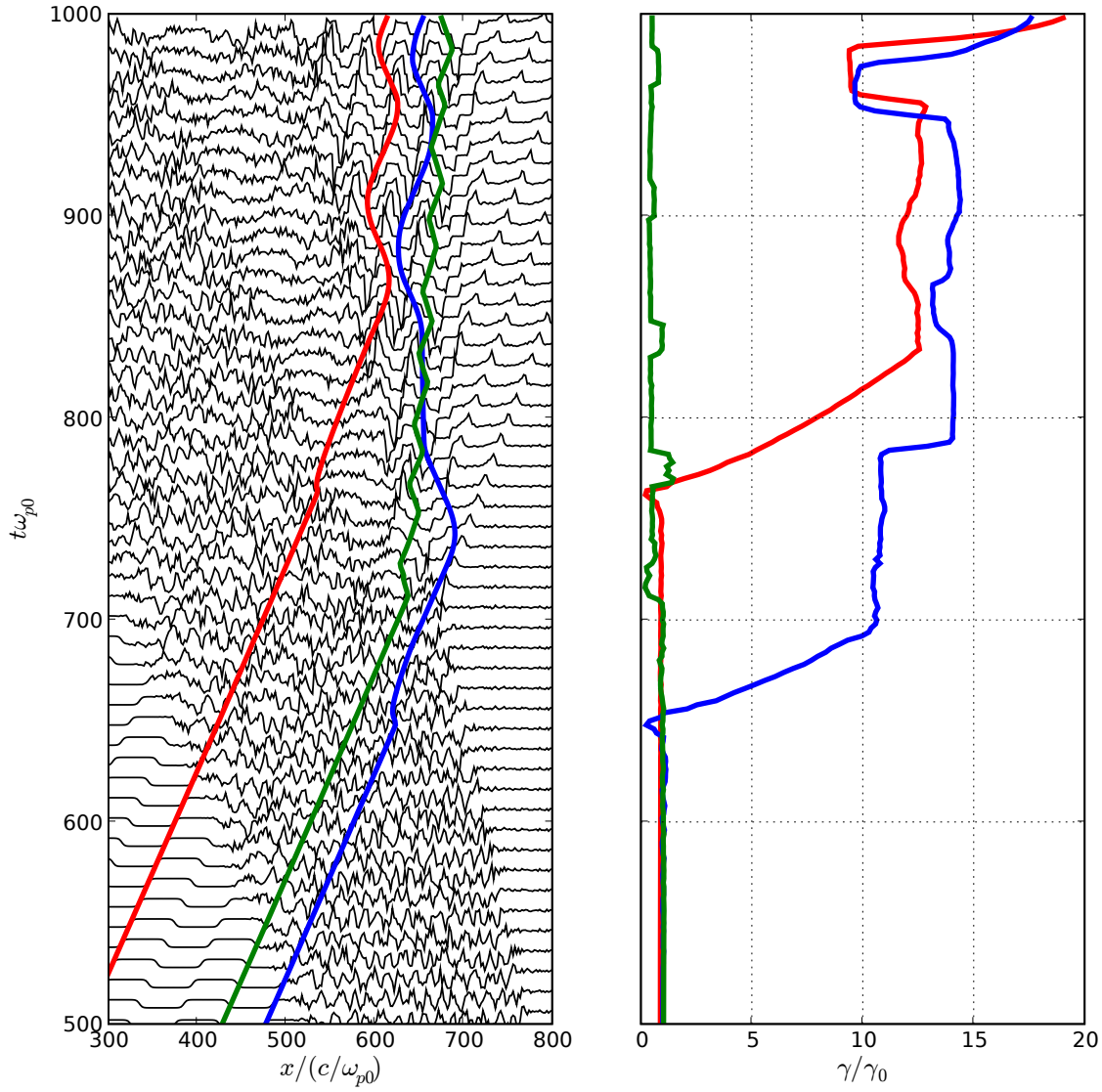

Figure 3.6: A stack plot of the magnetic field (left: black lines), three particle trajectories (left: red, blue and green line) and their energy histories (right: red, blue and green line). The time (t), space (x) are normalized by ω_{p0}^{-1}, c/ω_{p0}, respectively. Lorentz factor (γ) is normalized by its initial value. The final time plots are same as in Figure 3.5.

the dense current sheet plasma inside the magnetic neutral sheet, because the lower frequency band of the precursor is below the cut-off frequency in the dense plasma. As a result some particles begin the gyro-motion, and its kinetic energy in x-direction is identified as high in the downstream frame. Another important point is that the plasma inside the magnetic neutral sheet after the collision is still colder than the outside plasma. The cold plasma inside the neutral sheet is not as thermalized as calculated by the Rankine-Hugoniot relations, because the magnetosonic wave excited by the collision takes away the injection momentum.

The behavior of the alternating magnetic field structure depends on its initial width. For the case that the width is smaller than the gyro radius defined by the magnetic field and the particle energy inside the neutral sheet in the downstream, called thin current sheet case, the width expands to the gyro-scale by thermalization predominantly via magnetic dissipation. On the other hand in the thick current sheet case the width is almost unchanged. This means that the alternating magnetic field structure is stable against strong compression by the collision with a shock. The compression excites a large amplitude magnetosonic wave (see appendix C).

Second, we studied the interaction of the multi current sheet and the relativistic shock. In case that the initial current sheet width and each separation are smaller than the width in the thin current sheet case, we studied two situations. One is the equally spaced current sheet case, and the other is the unequally spaced case. These situations would be similar to the pulsar wind and the termination shock. Although the pulsar wind on the equatorial plane include equally spaced current sheets, the space is biased at latitudes.

In the equally spaced current sheet case a shock is not generated in the one-dimensional simulation . Because the alternating magnetic field structure is much smaller than a gyro-radius defined by the initial magnetic field and the bulk flow Lorentz factor, particles feel the average magnetic field, which is zero in case of equally spaced current sheets. As a result this is similar to the no magnetic field case. However the Weibel instability would trigger a shock structure in the multi-dimensional case with no background magnetic field as shown by Spitkovsky (2005) and Kato (2007).

On the other hand,if the current sheets are spaced unequally (see the right-top in Figure 3.3),

the average magnetic field is not zero. In this case particles complete the gyro-motion, and a shock is generated. At the shock front the alternating magnetic field is completely dissipated, which is documented by the electro-magnetic energy history in the top of Figure 3.4. The downstream parameters are well described by Rankine-Hugoniot relations using the average magnetic field of the upstream. This result is consistent with the suggestion by Lyubarsky (2003), which is to be a plausible mechanism to solve the σ problem. The dissipation process does not produce a non-thermal spectrum. Because the current sheet is less than the gyro-scale, motional electric field structure in such a scale is not excited. During the dissipation process, the alternating magnetic field structure overlaps with the next one, and the magnetic field disappears. Although magnetic reconnection is not considered realistically in this one-dimensional simulation, particle acceleration is not expected within such a sub-gyro-scale in the multi-dimensional case. Therefore the particle acceleration by the magnetic reconnection triggered by a collision with a shock would not work in the pulsar nebula.

In the thick current sheet case, the precursor accelerates the current sheet plasma and the collision with a shock front excites a magnetosonic wave, as we showed in the single current sheet case. A remarkable phenomenon is that the pre-accelerated particles by the precursor get additional energy from the magnetosonic waves. The cause of the acceleration is a motional electric field accompanied by the magnetosonic wave. Because the energy gain is proportional to the initial energy (see equation (3.12)), the pre-acceleration is important to achieve a high energy. Such particles form a high energy tail on the energy spectrum. On the other hand, the stability of the current sheet is an also important result. The magnetosonic wave carries momentum and compresses other current sheets. Our simulation showed that the current sheets in the downstream are also stable against such compressions. The electro-magnetic energy history in the bottom of Figure 3.4 means that excitation of the magnetosonic wave dominates over the dissipation. Although the alternating magnetic field is stable in one dimension, a multi-dimensional instability could trigger the magnetic field dissipation. Then we show the results of the two-dimensional simulations in the next chapter.

CHAPTER 4

Interaction between Current Sheets and a Shock in Two Dimension

We study the two-dimensional interaction between alternating magnetic fields and a relativistic collisionless shock using the exact-spectral method. The particles with larger gyro-radius than the clearance of each current sheets flow back upstream from the shock front. We found that such back flow excites the Weibel instability. The instability generate not only magnetic field, but also electric field in shock downstream frame. The electric field, different from alternating background component, accelerates particles. In case that the current sheet width and each clearance are smaller than the typical gyro-radius of the downstream plasma, the alternating magnetic fields completely dissipate within the shock transition region. Particles are not affected by the alternating magnetic fields but by the magnetic field excited by the Weibel instability. On the other hand, in case that the width and the clearance are comparable or larger than the gyro-radius, partial magnetic reconnections make the shock downstream nonuniform. So the large amplitude magnetosonic waves, shown in the one-dimensional case, disperse during the propagation. Unlike the small case, the alternating electromagnetic field additionally accelerates back-flow particles. Furthermore the residual magnetic fields often reflect the accelerated particles. This would yield the long term acceleration process.

4.1 Introduction

The one-dimensional shock wave has been studied for a long time. Many researchers revealed the precise of the complicated plasma phenomena of the shock wave. The Particle-in-Cell simulation

is frequently used to understand the plasma kinetic processes. Recently it is possible to run multi-dimensional simulations by PIC method due to the rapid advancement of computational power. Actually some people use the multi-dimensional PIC simulations, but most of those are three-dimensional simulation (Spitkovsky, 2005; Nishikawa et al., 2005). Although the three-dimensional PIC simulations can treat all kind of plasma processes in principle, the phenomena are extremely complicated. On the other hand, two-dimensional phenomena are relatively easy to understand because a lack of degree-of-freedom eliminates some plasma modes. So to understand the two-dimensional phenomena would help the analysis of the three-dimensional phenomena.

It is also worth noting that the smaller computational cost is the advantage of the two-dimensional simulations. The thee-dimensional simulations require a huge amount of computational power. It is not only for the simulation but also for the data analysis. However, to save the computational costs by decreasing the spacial and temporal resolution could lead wrong results or escape the attention of important physical processes. Especially the shock simulation needs enough time to wait until the boundary effects are to be negligible small.

As shown in chapter 2, we found the cause of the numerical Cherenkov radiation (Godfrey, 1974) and can eliminate it in case of the highly relativistic flow. Although the numerical Cherenkov radiation is electromagnetic mode in the early stage, it yields density fluctuation in the nonlinear stage. Such a effect can bring the serious problem to the simulation results. The conventional method to solve the Maxwell equations needs the low-pass filter to suppress the numerical Cherenkov radiation (e.g., Greenwood et al., 2004), but one have to be careful not to lose the physical phenomena by the filter. Even using the filter, the numerical Cherenkov radiation appears for a long time simulation.

In case of the perpendicular shock, which means the direction of the background magnetic field is perpendicular to the upstream flow direction (x), the two-dimensional simulation has two options against the direction of the background magnetic field. Here we set the axes of the simulation plane to x-y. The options are $\boldsymbol{B} = (0, 0, B_z)$ and $\boldsymbol{B} = (0, B_y, 0)$. One can also choose $\boldsymbol{B} = (0, B_y, B_z)$, but it can not take advantage of the simplicity of the two-dimensional

phenomena. One of the most significant differences is the degree of freedom for the velocity. In case of $\boldsymbol{B} = (0, 0, B_z)$, it is *two* because of no deformation of the magnetic field B_z, which is similar to the one-dimensional case. In case of $\boldsymbol{B} = (0, B_y, 0)$, that is *three*, because the simulation can treat the deflection of the magnetic field in the x-y plane. In this chapter we study the case of $\boldsymbol{B} = (0, B_y, 0)$.

4.2 Simulation Condition

Similar to the one-dimensional case (see section 3.2), the cold magnetized pair plasma is injected from the left boundary ($x = 0$) and the particles and the electromagnetic fields are reflected at the right boundary. As mentioned above, the background magnetic field is $\boldsymbol{B}_0 = (0, B_0, 0)$. The electric field is given by $\boldsymbol{E}_0 = -\boldsymbol{v_0} \times \boldsymbol{B}_0$ so as to be force free for the initial upstream plasma, where $\boldsymbol{v_0} = (v_0, 0, 0)$ is upstream flow velocity. The notation "0" means the initial upstream value. The magnetization parameter σ defined by equation (1.1) is 0.1 and the upstream bulk Lorentz factor $\gamma_0 = 1/\sqrt{1 - v_0^2/c^2}$ is 100. The alternating magnetic field is given by Harris equilibrium (Hoh, 1966; Kirk and Skjæraasen, 2003), and the density in the current sheet n_{cs0} is $10n_0$. The thermal four-velocity of the plasma both in the background and in the current sheet is $u_{th} = 0.1$. The unit of the time is a inverse of the symbolic plasma frequency $\omega_{p0} = \sqrt{8\pi n_0 e^2/(m\gamma_0)}$, and the spacial unit is c/ω_{p0}.

The spacial resolution is $\Delta x \leq 0.05c/\omega_{p0}$ and the temporal one is $\Delta t \leq 0.01/\omega_{p0}$. The Courant number is $c\Delta t/\Delta x = 0.2$ for all simulations. The particle number per a cell is more than 9 for each of electron and positron.

4.3 Shock by the Uniform Plasma Injection

Before trying the current sheets injection we check the case of the shock by the uniform plasma injection. The parameters are same to the above setting. Figure 4.1 shows the result about the density and magnetic field profiles. The right boundary is $x = 204.8c/\omega_{p0}$ and the scale of the

y-direction is $0 - 25.6c/\omega_{p0}$ as seen in the figure.

The shock front is located at $x \sim 115c/\omega_{p0}$, and the shock transition region is $115-120c/\omega_{p0}$. The shock downstream ($x > 120c/\omega_{p0}$) is nearly uniform. The compression ratio of the number density and the magnetic field (B_y) is ~ 3.3 as seen in the bottom of the figure. This result is consistent with the MHD solution by the Rankine-Hugoniot relations for $\Gamma = 4/3$ (see equation (1.7), (1.8) and figure 1.1). One can see the filament structures in the positron number density shown by the monochromatic contour in the top of the figure. Although we have not analyzed the formation mechanism yet, the cause is the precursor wave. The precursor wave pushes the upstream plasma leftward via ponderomotive force. The filaments are charge neutral, not current filaments. The density of the filaments is more than $10n_0$ for the dense part and the thin part is nearly zero. The strongly nonuniform upstream disturbs the shock front.

The energy spectrum of the particles is approximately three-dimensional Maxwellian (figure 4.2)

$$N(\gamma) \propto \gamma\sqrt{\gamma^2 - 1}\exp(-\gamma/T), \tag{4.1}$$

where T is a temperature normalized by the rest mass energy. So no acceleration is observed for this parameter at least. The peak at $\gamma = 100$ means the cold upstream plasma.

4.4 Thick Current Sheet

We show the result of relatively thick current sheets injection case. The current sheet width is $\lambda_{cs0} = 1c/\omega_{p0}$ and each clearance is $L = 10c/\omega_{p0}$. The typical gyro-radius defined by the injection bulk Lorentz factor ($\gamma_0 = 100$) and the magnetic field in the downstream by the Rankin-Hugoniot relations ($B_1 = 3.3B_0$) is $1.0c/\omega_{p0}$. So the current sheet width is comparable to the typical gyro radius, but their clearance is larger than the typical gyro-radius.

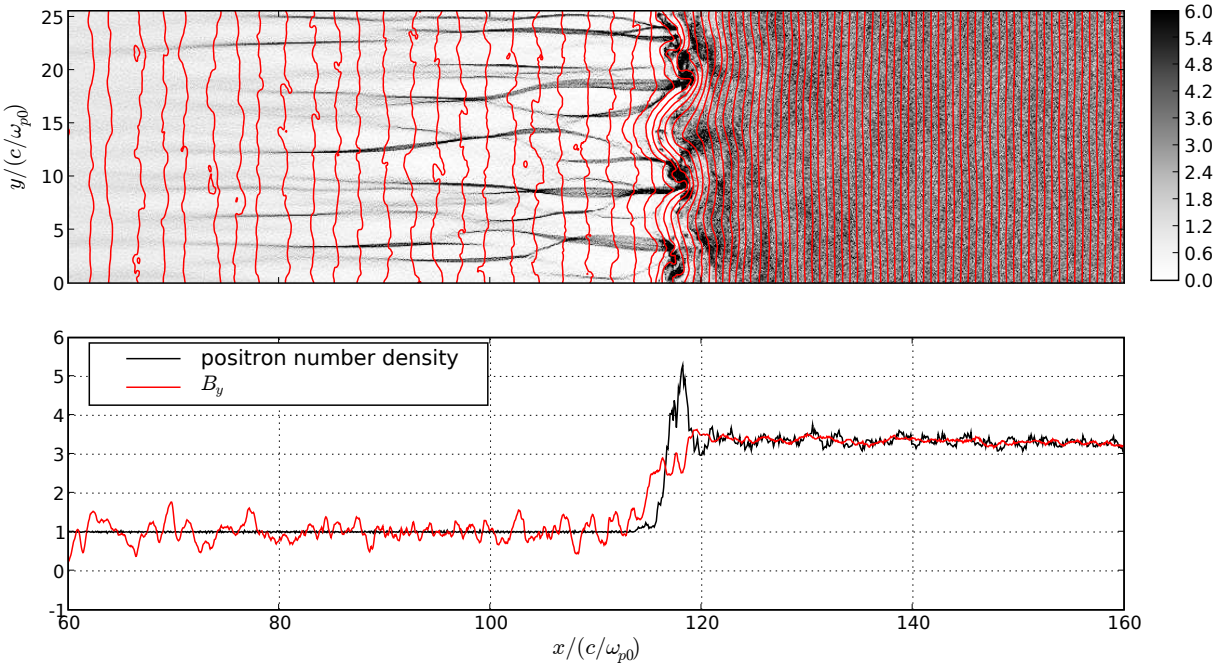

Figure 4.1: The shock structure with uniform upstream. Top is the positron number density (monochromatic contour) and the magnetic field lines (red lines). Bottom is the positron number density and the magnetic field (B_y) averaging over y-direction. All quantities are normalized by each initial upstream value.

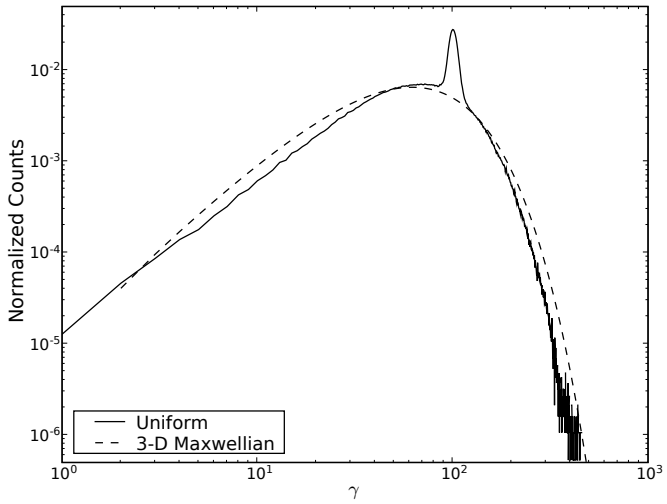

Figure 4.2: The energy spectrum of the shock simulation with uniform upstream. The particles are sampled within the region shown in figure 4.1.

4.4.1 General Representation

Figure 4.3 shows the particle distribution in phase space (x - u_x, u_y, u_z, γ), and the positron number density with the magnetic field lines in two-dimensional space (x-y). The phase space plots are represented by summation for y-direction. The magnetized electron-positron plasma are injected from the left boundary ($x = 0$), and are reflected by the right boundary ($x = 409.6$).

The shock front is located at $x \sim 280c/\omega_{p0}$. So the left region is the shock upstream and the right region is the shock downstream. In order to avoid the reflection of the large amplitude magnetosonic wave (see section 3.3.2) at the boundary, we prepare the uniform shock downstream to get through the magnetosonic waves by the injection of the uniform plasma in the beginning of the simulation. The uniform region is $x > 360c/\omega_{p0}$, not seen in figure 4.3. In the positron number density plot with the magnetic field lines, note that the direction of the magnetic field lines is anti-parallel on the both side of the current sheet, represented as dense parts with monochromatic contour.

The alternating magnetic fields injected in the early stage do not change their overall shape

in the downstream for $x = 320 - 360c/\omega_{p0}$, although the magnetic reconnections partially arise. The ones injected in later stage is twisted up via complete magnetic reconnections for $x = 280 - 320c/\omega_{p0}$. In the early stage the alternating magnetic field dose not change the shape so much at the moment of the collision with the shock front. As continuous collision of the alternating magnetic fields, the tearing mode gradually grows for each collision. Finally the magnetic field is completely reconnected with the neighboring anti-parallel one, as seen at $x = 280 - 320c/\omega_{p0}$ in figure 4.3, and the downstream becomes nonuniform.

For these reasons, in the early stage, the magnetosonic wave excited by the collision can propagate with the initial spiky shape in the uniform plasma. This is similar to the one-dimensional case (see CASE3 and CASE4 in figure 3.1). After the downstream becomes nonuniform, the magnetosonic waves diffuse during the propagation because of the spacial difference of the refractive index. One can check it in u_x (top) and γ (the fourth from top) plots in figure 4.3 as diffusing of the spiky structure with high energy particles from the shock front to the right, because the large amplitude magnetic field accompanying the strong magnetosonic wave instantaneously gives the energy to the particles. This is explained in the first paragraph section 3.3.3.

A part of particles are reflected at the shock front and flow upstream, seen in the plots for u_x and u_z of figure 4.3. The particles with larger gyro-radius than the current sheet clearance L do not complete their gyro-motion within the uniform magnetic field region between the adjacent current sheets. In the opposite signed magnetic fields, the Lorentz force works on the particles is opposite direction. Then the particles continuously across the magnetic field (see figure 4.4). Because such particles should have larger gyro-radius than the current sheets clearance, one can estimate the lower limit of the energy (Lorentz factor) of the back-flow particles.

$$\frac{mc^2\gamma}{eB} > L, \tag{4.2}$$

$$\frac{\gamma}{\gamma_0} > \sqrt{\sigma}\frac{L}{c/\omega_{p0}}, \tag{4.3}$$

where we applied the upstream magnetic field value to B. In this simulation case of $\sigma = 0.1$ and $L = 10c/\omega_{p0}$, the lower limit of the back flow particles is $\gamma/\gamma_0 > 3.2$. The criterion is slightly larger than the actual one, because the magnetic field profile for x direction is not rectangular

but the smooth function and the effective magnetic field is smaller than the value we used. Furthermore the back flow particles gain and lose energy by the existence of the electric field arise from the bulk motion of the upstream flow, so the various energy/momentum particles are seen in figure 4.3. Anyway the criterion means that only the relatively high energy particles of the thermalized downstream plasma can flow upstream.

4.4.2 Particle Acceleration Mechanism

The solid line in figure 4.5 shows the evolution of the energy spectrums of the particles within the whole region except the uniform plasma downstream. The high energy tail continuously grows during this simulation. The dashed line in the figure shows the relativistic Maxwellian for three-dimensional velocity space defined by equation (4.1). Clearly one can find the non-thermal tail on the spectrums (solid lines). The location of the high energy particles is seen in the bottom plot of figure 4.3. The green, cyan and yellow dots means the particles with Lorentz factor of > 800, > 1000 and > 1200, respectively. Most of them are located at just upstream of the shock front. The others are generated by the magnetosonic wave or coming from the upstream after accelerated. How are the particles accelerated in the upstream?

To conclude, the particles are accelerated by the electric fields E_y and E_z. E_z is accompanied with the background magnetic field B_y due to the bulk motion, but E_y should be generated by another process. The process is the Weibel instability, which is driven by anisotropy of the velocity distribution of the plasma (Weibel, 1959). The instability generates the magnetic field in the center-of-mass frame. So the electric field is observed from other frames. In our simulation case, the velocity anisotropy is brought by the upstream flow and the back-flow plasma, and the current filament is formed along x-direction. Therefore the magnetic field generated by the Weibel instability is B_z, and the observed electric field is E_y. These electromagnetic fields are different components from the background one (E_z, B_y). Kato (2005) showed the saturation level and the maximum amplitude of the magnetic field due to the Weibel instability. In our case velocity dispersion for x- and y-direction are $\sigma_{\parallel} \sim \gamma_0 = 100$ and $\sigma_{\perp} \sim u_{th}/c = 0.1$, respectively.

For such strongly anisotropic pair plasma case, the maximum magnetic field is evaluated by

$$\frac{B_{max}}{\sqrt{4\pi nmc^2}} = \frac{\chi\sigma_{\parallel}}{\sqrt{\tilde{\gamma}}}, \tag{4.4}$$

where χ $(= 1/3 - 1)$ is an isotropization parameter, $\tilde{\gamma}$ is defined by $\tilde{\gamma} = \sqrt{1 + \sigma_{\parallel}^2 + 2\sigma_{\perp}^2}$. Now we roughly estimate the maximum magnetic field from equation (4.4)

$$\frac{B_{max}}{B_0} = \chi\frac{\sigma_{\parallel}}{\gamma_0}\sqrt{\frac{1}{2\sigma}\frac{n}{n_0}\frac{\gamma_0}{\tilde{\gamma}}}. \tag{4.5}$$

Assuming $\tilde{\gamma} \sim \sigma_{\parallel} \sim \gamma_0$, $n \sim n_0$ and $\chi \sim 1$, and using $\sigma = 0.1$, the maximum magnetic field is $B_{max}/B_0 \sim 2$. Then the Weibel instability can generate the magnetic field with comparable amplitude to the background B_0. Here we define v_c as the relative velocity between the center-of-mass frame and the shock downstream frame, and the maximum electric field is $|E_{max}| = |v_c B_{max}|/c$. The relative velocity could be roughly c, so the amplitude of the maximum electric field is also comparable to the background magnetic field. The possibility can be assured using the equation of motion for the Lorentz factor,

$$mc^2\frac{d\gamma}{dt} = q\boldsymbol{v}\cdot\boldsymbol{E}. \tag{4.6}$$

For the estimate, this equation can be rewritten using the energy gain $\Delta\gamma$ for the time interval Δt,

$$\frac{\Delta\gamma}{\gamma_0} = \sqrt{\sigma}\frac{E}{B_0}\omega_{p0}\Delta t. \tag{4.7}$$

Then substituting $E_{max} \simeq B_{max}$ into E in equation (4.7) and using equation (4.5), one can obtain the relation

$$\frac{\Delta\gamma}{\gamma_0} \simeq \chi\frac{\sigma_{\parallel}}{\gamma_0}\sqrt{\frac{1}{2}\frac{n}{n_0}\frac{\gamma_0}{\tilde{\gamma}}}\omega_{p0}\Delta t \sim \frac{1}{\sqrt{2}}\omega_{p0}\Delta t. \tag{4.8}$$

This equation means the acceleration ratio does not explicitly depend on σ. The reason is that originally both equation (4.4) and (4.6) do not depend on the background magnetic field B_0, but the phenomena depends on the velocity anisotropy and the density. Then if the velocity anisotropy and the density are respectively proportional to the upstream bulk Lorentz factor γ_0 and the upstream density n_0, the result of equation (4.8) is universal against σ. In practice

the result partially depends on σ via the condition of the back-flow particles described by equation (4.3). The acceleration ratio of $\sim \omega_{p0}\Delta t/\sqrt{2}$ is quite large. However this acceleration does not take place continuously. The comparison with the simulation results is discussed later.

The amplitude of the electromagnetic fields and spacial structures are confirmed by figure 4.6. Figure 4.6 shows the electric fields $\boldsymbol{E} = (E_x, E_y, E_z)$, the magnetic fields $\boldsymbol{B} = (B_x, B_y, B_z)$, the current densities $\boldsymbol{J} = (J_x, J_y, J_z)$ and the charge density ρ. Figure 4.6 is same time to figure 4.3. One can see the alternating magnetic field of B_y and the accompanying electric field E_z in the upstream. The current J_z to keep the gradient of the magnetic field in the upstream is disturbed because it is much smaller than the fluctuation by modulation of the precursor wave.

In the upstream ($x < 280$), J_x and ρ show the current filaments and B_z changes its sign roughly where the J_x and ρ are maximum. This is typical feature of the Weibel instability. The pattern of B_z corresponds to E_y, and this is explained by the relation $|E_{max}| = |v_c B_{max}|/c$. E_y decreases within the shock transition region ($x = 280 - 300c/\omega_{p0}$), where the relative velocity v_c gradually approaches zero. So the behavior of electric field E_y in the transition region is also explained well by the relation $|E_{max}| = |v_c B_{max}|/c$. On the other hand the magnetic field B_z increases at the same time, because the plasma is compressed as the flow velocity decreases. In the upstream, the amplitude of B_z is partly larger than B_y, and this is consistent with equation (4.5).

Figure 4.7 shows the history of the two typical accelerated positrons. In the left plot the shock front moves from $(x(c/\omega_{p0})^{-1}, t\omega_{p0}) = (293, 307)$ to $(280, 408)$. Both particles travel with crossing the shock front during the time. Here we call the particles represented by the solid lines and the dashed lines "A" and "B" for convenience, respectively. In the middle plot "B" constantly gains energy (γ) as increasing the absolute value of u_y. "A" also dose for $t\omega_{p0} = 375 - 385$, and additionally does as increasing of u_x for $t\omega_{p0} = 400 - 408$. Both particles are not accelerated z-direction. So two kind of acceleration, for u_x and u_y, works on the particles. Note that the acceleration for u_y is opposite signed direction in spite that the two particles have same positive charge. This means each particle are accelerated by opposite signed

E_y, see equation (4.6). Although the electric fields work on these particles sharply fluctuate in the right plots, E_y and E_z is dominant rather than E_x. Considering equation (4.6), one can guess that the averagely negative E_y accelerates "B" with negative u_y constantly, and the positive E_y does "A" with positive u_y for $t\omega_{p0} = 375 - 385$. As above, one can confirm that E_y generated by the Weibel instability accelerates particles. The acceleration ratio estimated by equation (4.8) does not continuously take place but instantaneously at $t\omega_{p0} = 375 - 385$ for "A" and $t\omega_{p0} = 350 - 360$ for "B". On the other hand, E_x is not so large for "A" during $t\omega_{p0} = 400 - 408$, even though the particle is accelerated for x-direction (u_x). This is explained as the quick drift motion by the large (E_z, B_y) at $x = 290c/\omega_{p0}$, see figure 4.6.

When the particles escape into the downstream, some of them are reflected by the residual magnetic field and go back to upstream, like "A" at $(x(c/\omega_{p0})^{-1}, t\omega_{p0}) = (295, 344)$ and "B" at $(295, 330)$ in figure 4.7. Therefore the acceleration might be said as a kind of the diffusive shock acceleration.

4.5 Thin Current Sheet

We also show the case of thin current sheets. The current sheet width is $\lambda_{cs0} = 0.1c/\omega_{p0}$ and each clearance is $L = 1.2c/\omega_{p0}$. As shown in appendix C, the amplitude of the magnetosonic wave is not so large. So we do not prepare the absorption region unlike the thick current sheets case. The other parameters are same to the above case.

4.5.1 General Representation

Using equation (4.3), the energy criterion of traversing magnetic fields is $0.38\gamma_0$. Therefore most particles hardly feel the alternating magnetic fields. Actually the injection flow is just reflected at the right boundary in the beginning of the simulation.

Figure 4.8 shows the particle distribution in phase space (x - u_x, u_y, u_z, γ), and the positron number density with the magnetic field lines in two-dimensional space (x-y). The phase space plots are represented by summation for y-direction. The magnetized electron-positron plasma

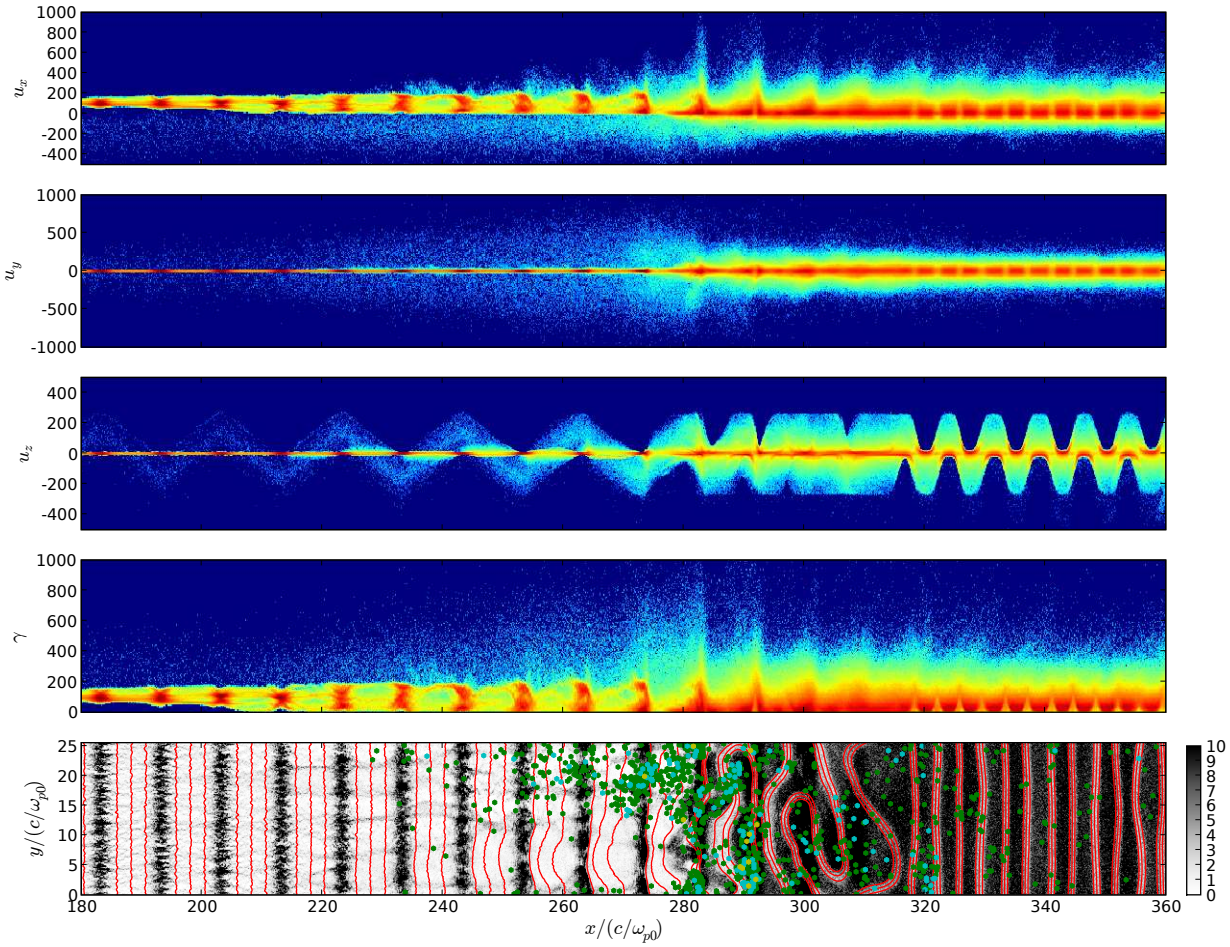

Figure 4.3: Phase space density plots and number density with magnetic field lines for positron. All abscissa are spacial axes for x. From the above the phase space density for u_x, u_y, u_z and γ is represented by the color contour with logarithmic scale. Bottom shows the positron number density as the monochromatic contour and the magnetic field lines with red lines. The density contour is normalized by the initial upstream value. The green, cyan and yellow dots mean the high Lorentz factor particles of > 800, > 1000 and > 1200, respectively.

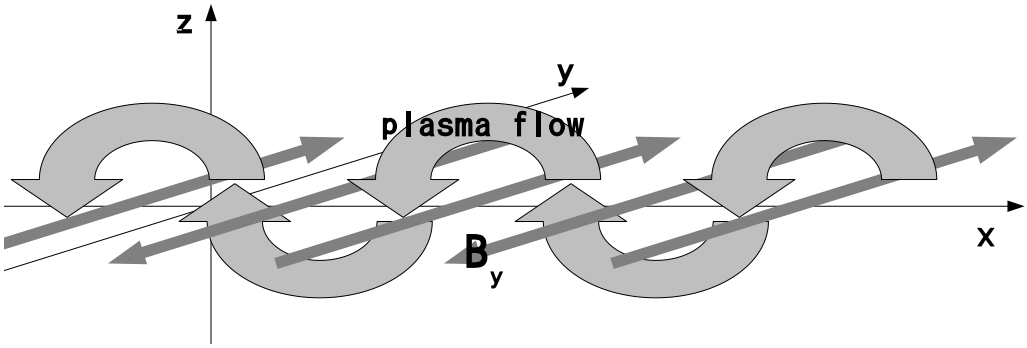

Figure 4.4: Schematic picture of back-flow plasma.

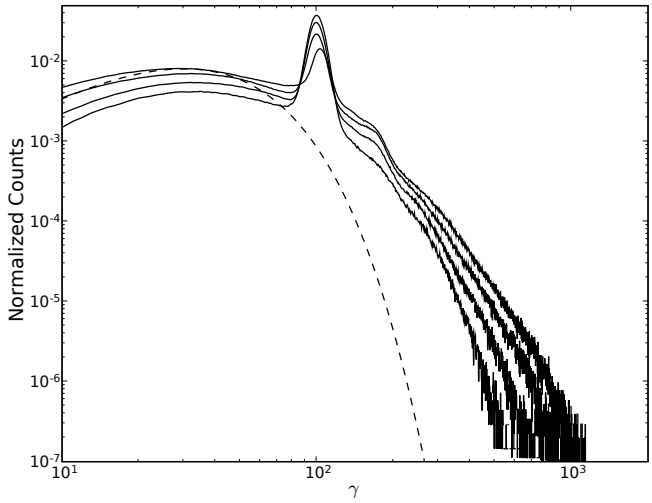

Figure 4.5: Time evolution of normalized energy (Lorentz factor) spectrums of the plasma within the region of the alternating magnetic fields (solid line) and three-dimensional Maxwellian (dashed line). The solid lines show the energy spectrum for each $t = 40/\omega_{p0}$. The sharp peaks at $\gamma = 100$ are contribution of the cold upstream plasma. The spectrums continuously become harder. The spectrum with highest energy tail is the final time snapshot, which is same time to that of figure 4.3 and 4.6. The temperature of the Maxwellian is $T = 0.15mc^2\gamma_0$, which is smaller than the value expected by the Rankine-Hugoniot relations, to fit the moderate peak at $\gamma \sim 30$.

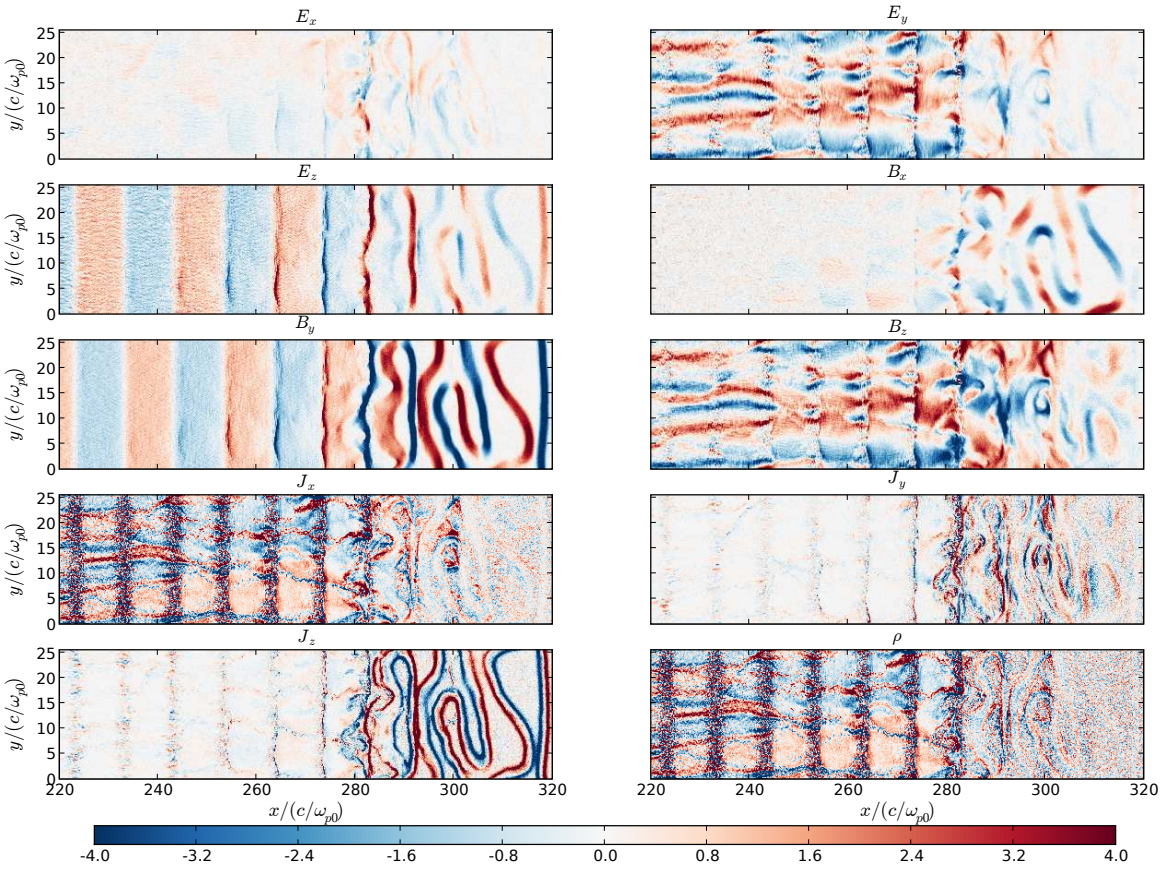

Figure 4.6: Spacial distribution of electric fields, magnetic fields, current densities and charge density. All quantities are normalized by the initial upstream value of the background magnetic field (B_0). As shown by the color bar, red and blue mean positive and negative, respectively. The time of this snapshot is identical to that of figure 4.3.

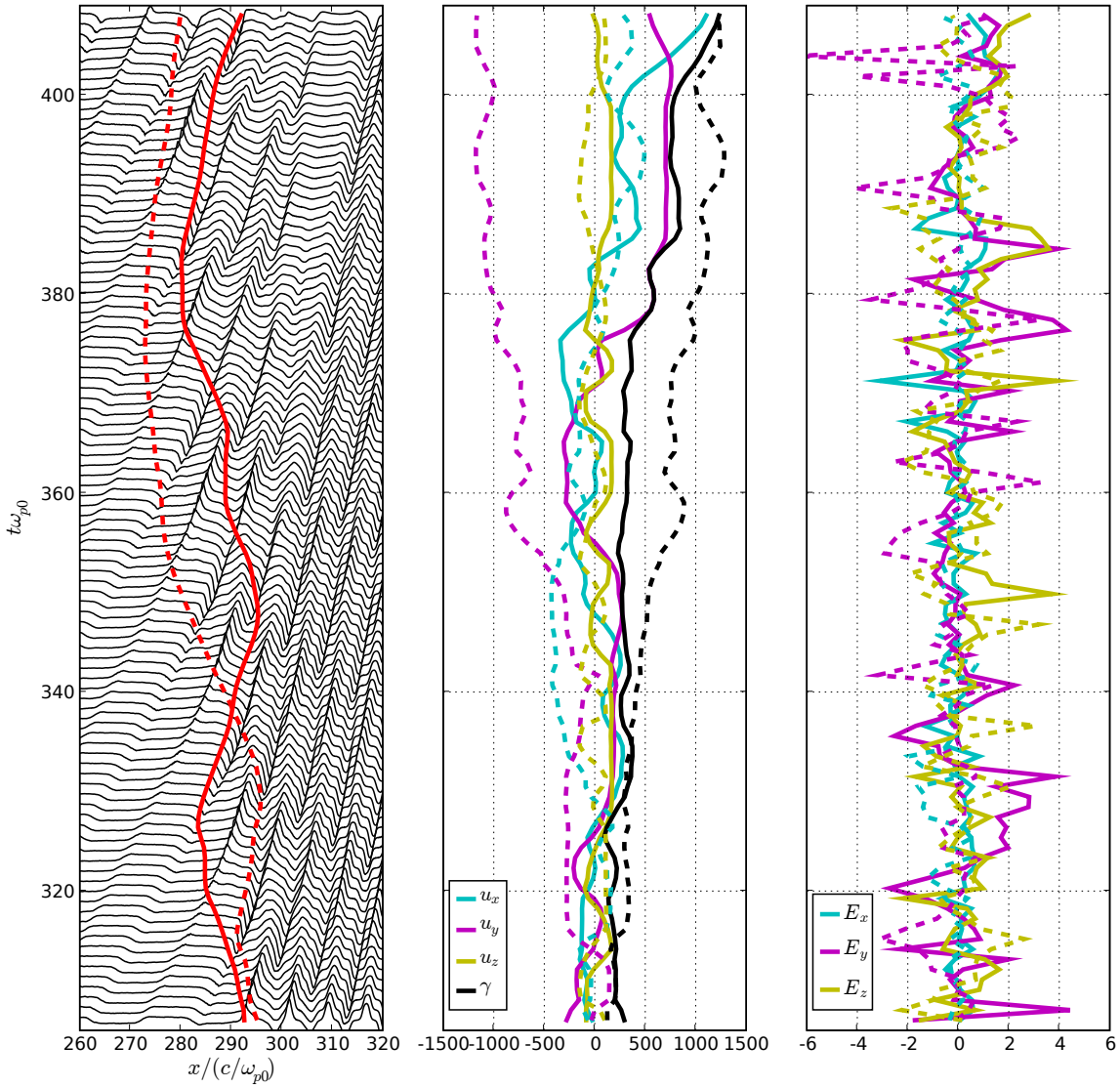

Figure 4.7: History of two positrons. The two positrons are represented by the solid lines and the dashed lines, respectively. The ordinates are the temporal axes. Left plot shows the particle location for x (red lines) with the stack plot of the magnetic field (B_y) averaged over y-direction. Middle shows the four-velocity and the Lorentz factor. Right shows the electric fields works on each particle. The four-velocity, the Lorentz factor and the electric fields are normalized by each initial upstream value. The plot of the final time step is identical to the plot of figure 4.3 and 4.6.

are injected from the left boundary ($x = 0$), and are reflected by the right boundary ($x = 163.8$). The shock front is located at $x \sim 90c/\omega_{p0}$. In one-dimensional case both without background magnetic field and with alternating magnetic field accompanying thin current sheets (section 3.4.1), a shock is not formed. Kato (2007) showed the shock formation due to the Weibel instability in the two-dimensional simulation. In the top of figure 4.9, the dashed line shows the absolute value of B_z averaged over y-direction. B_z suggests the Weibel instability and increases around the shock transition region $x = 80 - 110c/\omega_{p0}$. Then in this case the Weibel instability also plays a role in formation of the shock as explained by Kato (2007).

The u_z plot in figure 4.8 shows that the downstream plasma is barely thermalized along z-direction. So the behavior of the plasma is almost two-dimensional in x-y plane. This should affect the compression ratio, see the bottom plot of figure 1.1. The compression ratio is calculated via density profile in figure 4.9. The density averaged over a half period of the Harris magnetic field (Hoh, 1966; Kirk and Skjæraasen, 2003) in the upstream is

$$\frac{\langle n \rangle}{n_0} = \frac{\int_{-L/2}^{L/2} n_{cs0} \cosh^{-2}(x/\lambda_{cs0}) dx + L n_0}{L n_0} \tag{4.9}$$

$$\simeq \frac{2\lambda_{cs0}}{L} \frac{n_{cs0}}{n_0} + 1 \simeq 2.7, \tag{4.10}$$

where these parameters are $\lambda_{cs0} = 0.1c/\omega_{p0}$, $L = 1.2c/\omega_{p0}$, $n_{cs0} = 10n_0$. The downstream density is $\sim 8.5n_0$ by the bottom plot of figure 4.9, so the compression ratio is ~ 3.1. On the other hand the ratio calculated by the Rankine-Hugoniot relations with the two-dimensional adiabatic index $\Gamma = 3/2$ is 3 for $\sigma = 0$ by equation (1.8), see also figure 1.1. This result means the shock is similar to the case of unmagnetized plasma with two-dimensional velocity space. The reason is that the magnetic field B_z excited by the Weibel instability works on the particles, rather than the alternating magnetic field B_y. Figure 4.10 also supports the result. From the upstream to the shock transition region ($x < 115c/\omega_{p0}$), the Weibel instability excites E_y, B_z, J_x and ρ. Meanwhile, the amplitudes of (E_z, B_y) is much smaller than that of (E_y, B_z) in the same region. In the downstream the magnetic field B_y is vanishingly dissipated, which is also shown by the magnetic field lines (red lines) in the bottom plot of figure 4.8 and the top plot with solid line in figure 4.9.

The above result indicates another important result. That is, the downstream condition is same the one derived by the upstream of $\sigma = 0$ in spite of the finite value of σ in practice. In particular, considering the alternating magnetic fields and the current sheets, the averaged-σ of the upstream plasma, called $\langle\sigma\rangle$, is defined by

$$\langle\sigma\rangle = \frac{\langle B_0^2\rangle}{8\pi\langle n_0\rangle mc^2\gamma_0} \tag{4.11}$$

$$= \frac{\langle B_0^2\rangle/B_0^2}{\langle n_0\rangle/n_0^2}\sigma, \tag{4.12}$$

where $\langle B_0^2\rangle$ is given by

$$\frac{\langle B_0^2\rangle}{B_0^2} = \frac{\int_{-L/2}^{L/2}\tanh^2(x/\lambda_{cs0})dx}{L} \tag{4.13}$$

$$\simeq 1 - \frac{2\lambda_{cs0}}{L} \simeq 0.83. \tag{4.14}$$

$\langle n_0\rangle$ is given by equation (4.10). Therefore $\langle\sigma\rangle = 0.03$, but the result is inconsistent with the result suggesting $\sigma = 0$ in the upstream. As shown in appendix D, the downstream condition follows σ' which is σ evaluated by $\langle B_0\rangle^2$ ($= 0$ in this case), not $\langle\sigma\rangle$ by $\langle B_0^2\rangle$, when the alternating magnetic fields disappear in the downstream.

4.5.2 Particle Acceleration

Figure 4.11 shows the time evolution of the energy spectrum. The spectrum with the highest energy tail is at the final time step, corresponding to figure 4.8, 4.9 and 4.10. The dashed line shows the two-dimensional Maxwellian,

$$N(\gamma) \propto \gamma\exp(-\gamma/T). \tag{4.15}$$

The high energy tail gradually grows with time. So the spectrum may become harder for a longer term, although the acceleration is still weak within the short time simulation. Figure 4.12 shows the trajectory of two accelerated positrons. In the left plot, the shock front travels from $(x(c/\omega_{p0})^{-1}, t\omega_{p0}) \sim (125, 80)$ to $(85, 160)$, then the shock speed is $\sim 0.5c$. The two particles gain energy with comparable level, but their location of x is different each other at all times.

The particle represented by the solid ! !lines, called "A," is mainly located in the upstream. The particle represented by the dashed lines, called "B," traces the trajectory "A" until $t = 115\omega_{p0}$, and then drifts into the shock downstream region. Both particles are strongly affected by E_y all the time, shown in the right plot of figure 4.12. In response to the E_y, u_y changes widely. Additionally, as seen in the drift motion of "B" at $t = 115\omega_{p0}$, the change of u_x is yielded by the Lorentz force of (E_y, B_z). Therefore the electric field E_y excited by the Weibel instability exists from the upstream to the shock transition region (see figure 4.10), and can accelerate these particles.

One of the differences from the thick current sheets case is the effect of (E_z, B_y). This background components often accelerate particles, which is seen as a particle represented by solid lines is accelerated during $t\omega_{p0} = 400 - 408$ in figure 4.7. In this small current sheets case the acceleration by (E_z, B_y) is not expected. The other is the reflection of particles in the downstream. In the thick current sheets case the residual magnetic fields of background component (B_y) in the downstream often reflects the accelerated particles to the upstream. However, in this case, the background alternating magnetic fields completely dissipates and can not reflect particles. Therefore the continuous acceleration with crossing the shock front in the thick current sheets case does not work in this thin current sheets case.

4.6 Summary and Discussion

We investigated the interaction between alternating magnetic fields and a relativistic collisionless shock in two-dimension. At the beginning, we showed the result of the uniform inflow case. The y-averaged shock feature (shown in the bottom of figure 4.1) confirms consistency with the MHD result by the Rankine-Hugoniot relations. It should be noted that the filamentation of the upstream plasma in the top of figure 4.1. Although we do not analyze precisely, it seems that the precursor wave induces it via radiation pressure. Accordingly the nonuniform upstream plasma disturbs the shock front. The energy spectrum in figure 4.2 is nearly relativistic Maxwellian for three-dimensional velocity space defined by equation (4.1). So the particle

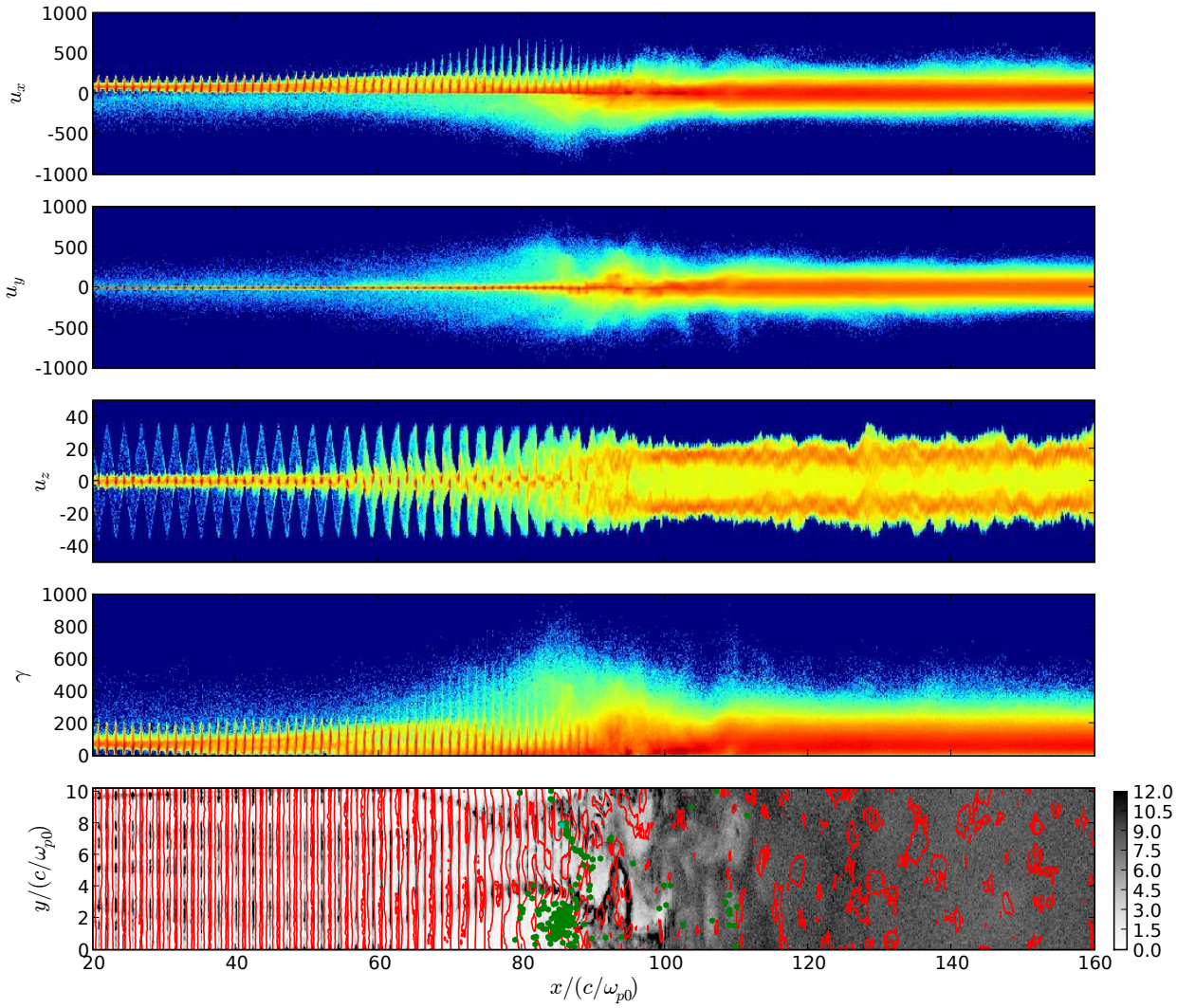

Figure 4.8: Phase space density plots and number density with magnetic field lines for positron. All abscissa are spacial axes for x. From the above the phase space density for u_x, u_y, u_z and γ is represented by the color contour with logarithmic scale. Bottom shows the number density as the monochromatic contour and the magnetic field lines with red lines. The green and cyan dots mean the high Lorentz factor particles of > 800 and > 1000, respectively.

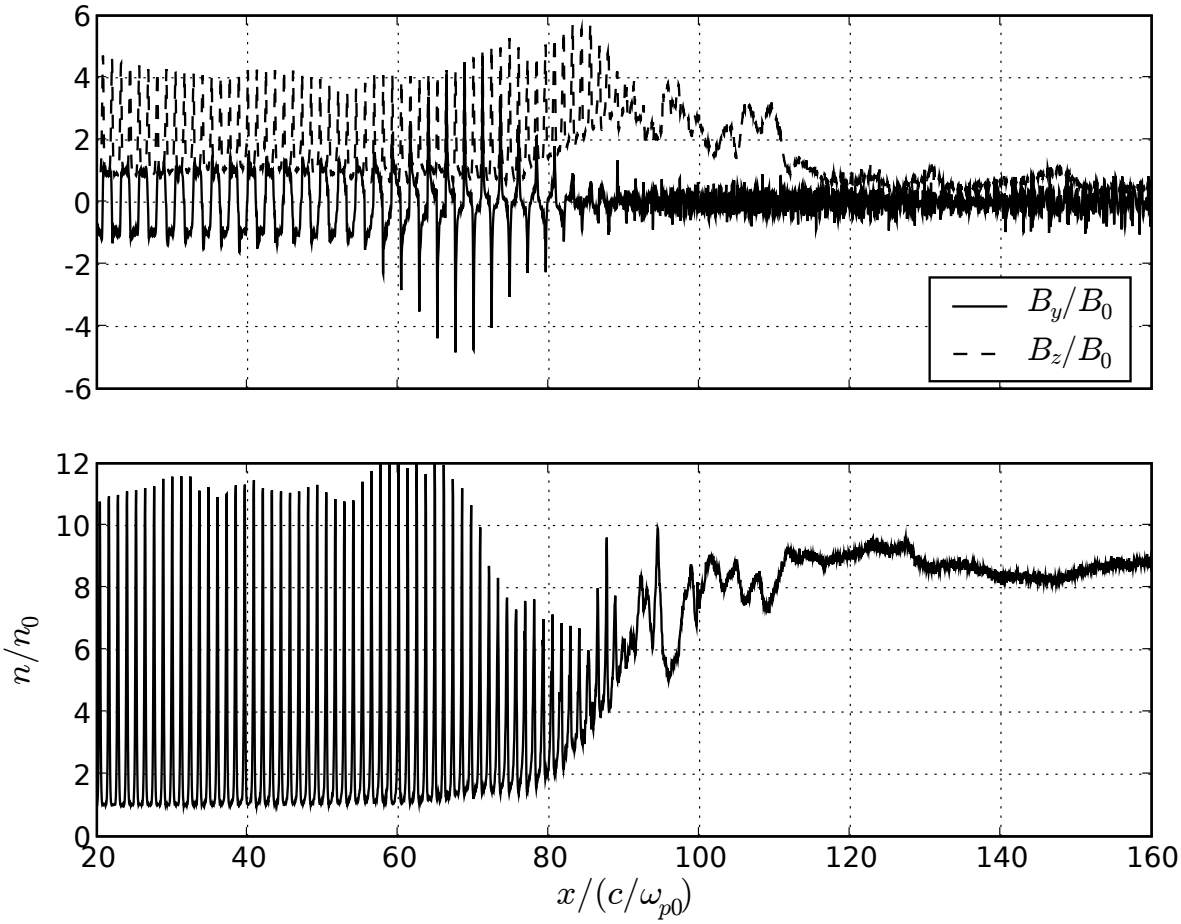

Figure 4.9: Shock profiles for x-direction, averaged over y. Top shows the magnetic field B_y and the *absolute value* of B_z. Bottom is density n. They are normalized by each initial upstream value. The peaks of B_z in the upstream is affected by the dense current sheets, explained by equation (4.5).

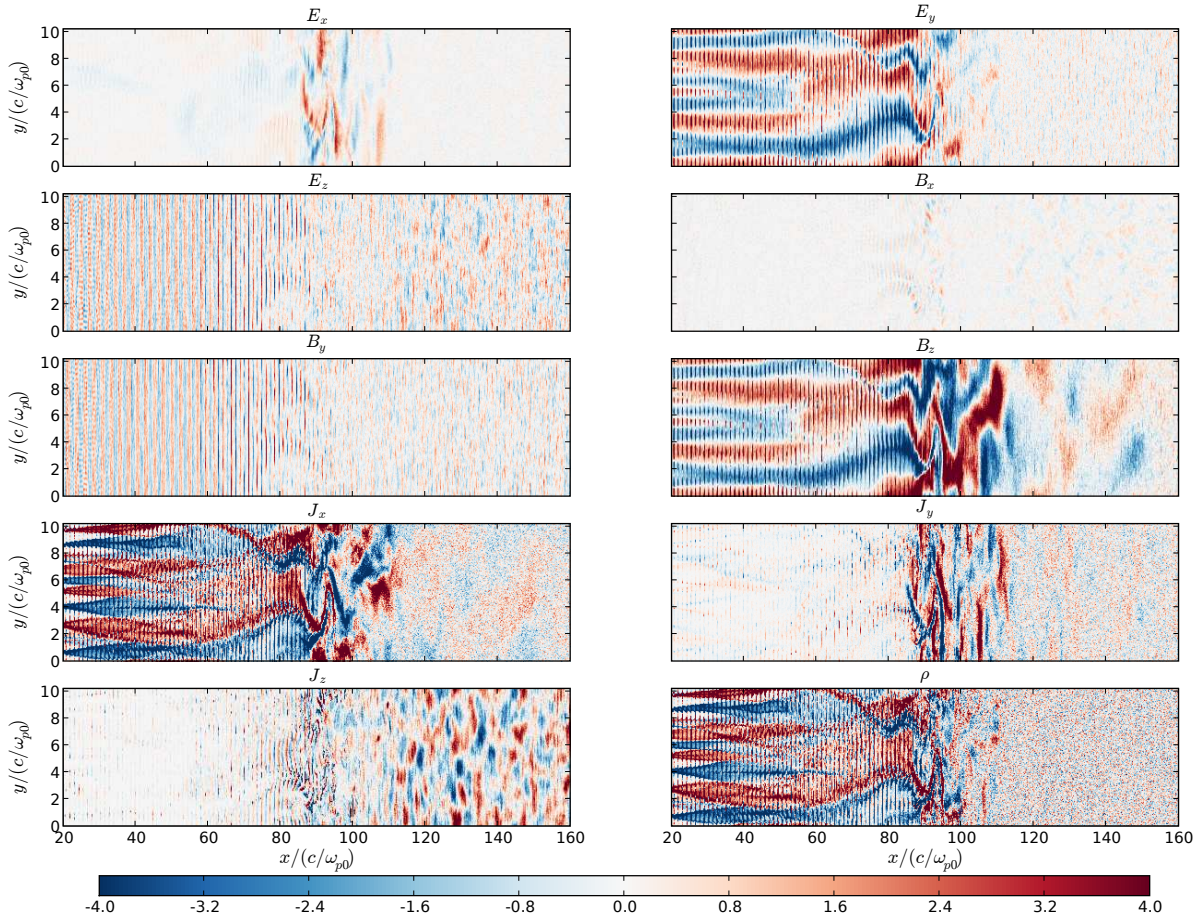

Figure 4.10: Spacial distribution of electric fields, magnetic fields, current densities and charge density. All quantities are normalized by the initial upstream value of the background magnetic field (B_0). As shown by the color bar, red and blue mean positive and negative, respectively. The time of this snapshot is identical to that of figure 4.8 and 4.9.

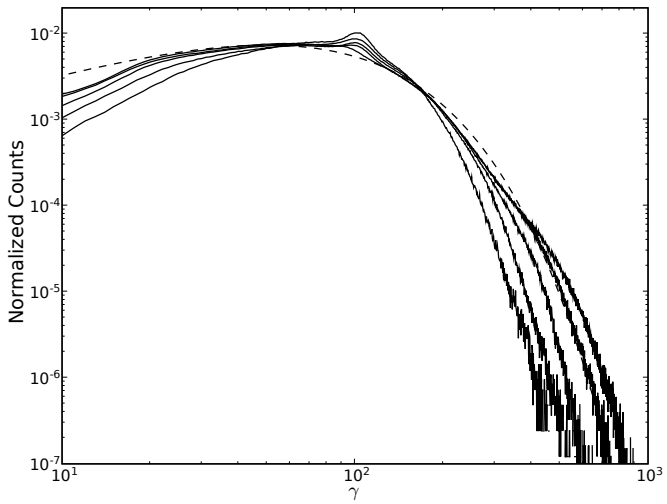

Figure 4.11: Time evolution of normalized energy (Lorentz factor) spectrums of the plasma within the region of the alternating magnetic fields (solid line) and two-dimensional Maxwellian (dashed line) defined by equation (4.15). The solid lines show the energy spectrum for each $t = 30/\omega_{p0}$. The peaks at $\gamma = 100$ are contribution of the cold upstream plasma. The spectrums continuously become harder. The spectrum with highest energy tail is the last time snapshot, which is same time to that of figure 4.8, 4.9 and 4.10. The temperature of the Maxwellian is $T = 0.5mc^2\gamma_0$, which is consistent with the value expected by the Rankine-Hugoniot relations.

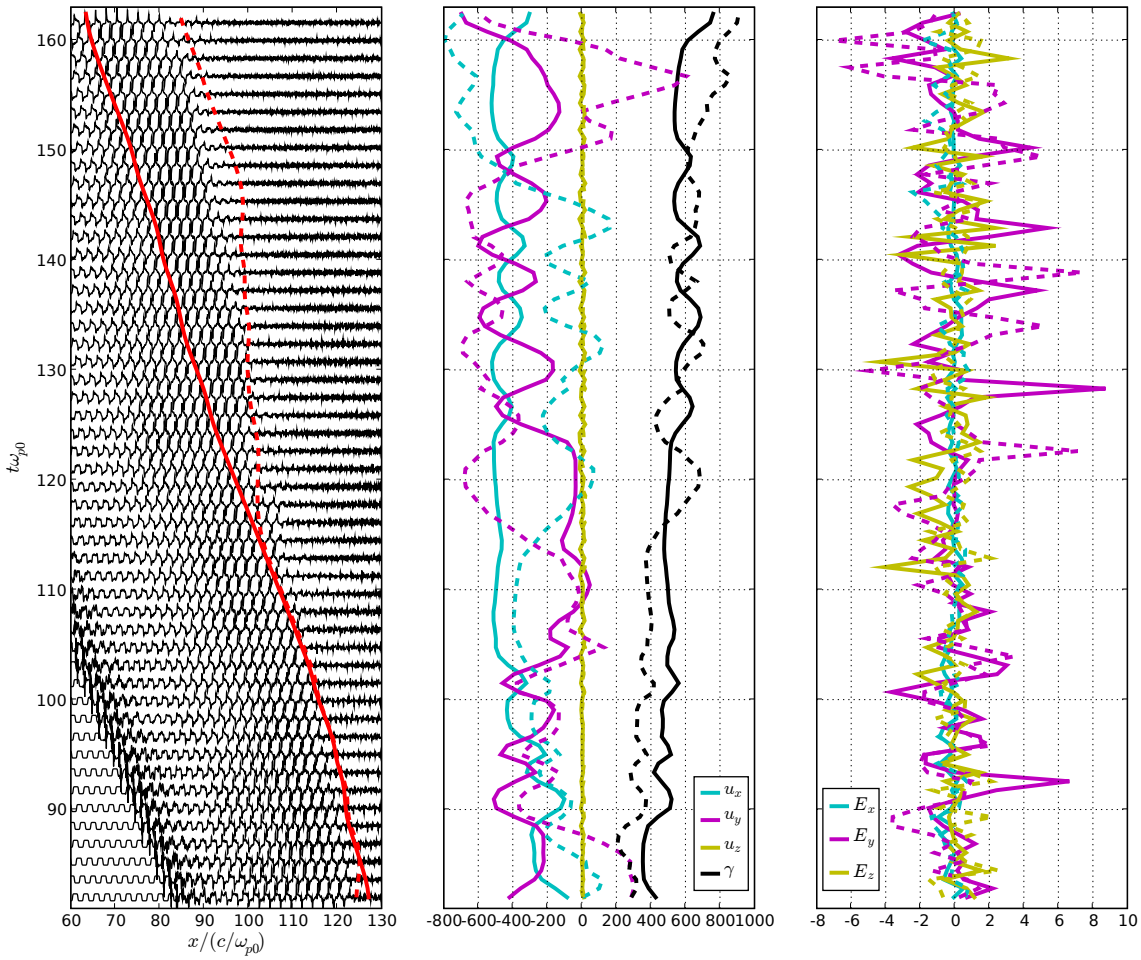

Figure 4.12: History of the two positrons. The two positrons are represented by the solid lines and the dashed lines, respectively. The ordinates are the temporal axes. Left plot shows the particle location for x (red lines) with the stack plot of the magnetic field (B_y) averaged over y-direction. Middle shows the four-velocity and the Lorentz factor. Right shows the electric fields works on the particle. The four-velocity, the Lorentz factor and the electric fields are normalized by each initial upstream value. The plot of the final time step is identical to the plot of figure 4.8, 4.9 and 4.10.

acceleration is not observed in this simulation setting.

Next the alternating magnetic fields with thick current sheets are injected into the uniform shock. Only the particle with larger gyro-radius than the clearance of the current sheets can across the alternating magnetic fields, because such particles do not complete their gyro-motion within the uniform magnetic field region between the adjacent current sheets. The gyro-radius is proportional to the Lorentz factor so we found the energy criterion of such particles, represented by equation (4.3). Some of the particles satisfy the criterion flow back upstream, seen in figure 4.3.

Such back-flow particles induces the Weibel instability from the upstream to the shock transition region. The instability generates magnetic field B_z, different from the background one B_y. Because the center-of-mass frame is different from the shock downstream frame, E_y is also observed in figure 4.6. The electric field E_y by the Weibel instability and the background one E_z accelerate the particles, which presents as a high energy tail of the spectrum in figure 4.5. As seen in figure 4.7 the accelerated particles travel between the shock upstream and the shock downstream. The reflection in the upstream is yielded by the drift motion and that in the downstream is by the residual magnetic fields. This result indicates the long term acceleration. Additionally the high energy tail grows with time in figure 4.5.

Finally, we showed the case of thin current sheets injection. The current sheet width and each clearance are smaller than the typical gyro radius defined by the upstream magnetic field and bulk Lorentz factor. Actually the particles barely feel the magnetic field. Unlike the one-dimensional case, the shock is formed due to the Weibel instability (Kato, 2007). This means the magnetic field excited by the instability (B_z) works on particles, rather than the alternating magnetic fields (B_y). The shock structure is similar to the unmagnetized plasma case. Because the magnetic field excited by the Weibel instability is perpendicular to the x-y plane, the distribution of the particle velocity is nearly two-dimensional (u_x, u_y). The alternating magnetic fields B_y dissipates completely in the downstream, and the other B_z also disappear after the shock transition region. So the particle reflection in the downstream does not take place, but still figure 4.11 indicates the growth of high energy tail.

The condition of the thin current sheets case is similar to the pulsar wind. As shown in section 4.5.1 and appendix D, the shock downstream condition is determined by $\langle B_0 \rangle$. Therefore the effective-σ, or σ', changes from 0 to $\langle \sigma \rangle$ in response to the change of latitude of the pulsar wind from the equatorial plane to the edge which the alternating magnetic fields exist (see figure 1.7). The difference of value between σ' and $\langle \sigma \rangle$ means the efficient magnetic dissipation. This result would solve the σ problem. Additionally the acceleration via the Weibel instability is valid close to the equatorial plane.

CHAPTER 5

Concluding Remarks

We studied the interaction between alternating magnetic fields and a relativistic shock in electron-positron plasma.

First, in order to solve the two-dimensional relativistic shock simulation by Particle-in-Cell method correctly, we studied the solution to the numerical Cherenkov radiation. The solution is given by a set of follows.

- Using "the exact spectral method" to correctly solve the dispersion relation of electromagnetic mode
- Filtering the largest resonance point by aliases of the current density

Second, we studied the interaction between alternating magnetic fields and a relativistic shock using one-dimensional PIC simulations. The phenomena are classified into two cases. One is "small current sheet": the current sheet width and each clearance are smaller than the downstream typical gyro-radius. The other is "large current sheet": the current sheet width and each clearance are comparable or larger than the downstream typical gyro-radius.

1. Common feature
    - Particle acceleration by the precursor wave
2. Small current sheet
    - Strong dissipation of the alternating magnetic fields

3. Large current sheet

    - Excitation of large amplitude magnetosonic waves
    - Additional particle acceleration by the magnetosonic waves

Although the acceleration by the precursor wave is not seen for "small current sheet" in our simulation time scale, it should arise in principle.

Finally, we studied the interaction by the two-dimensional simulations on the basis of the one-dimensional study. The classification is similar to the one-dimensional case.

1. Common feature

    - Flowing back particles with crossing the alternating magnetic fields
    - Weibel instability by the back flow
    - Particle acceleration by the electric field excited by the Weibel instability

2. Small current sheet

    - Strong dissipation of the alternating magnetic fields by the magnetic reconnection

3. Large current sheet

    - Dispersion of large amplitude magnetosonic wave in nonuniformalized downstream by magnetic reconnections
    - Additional particle acceleration by the alternating electromagnetic field in the upstream
    - Particle reflection by the residual magnetic field in the downstream

Although we did not observe the acceleration by the precursor wave within the simulation time because of computational limitation, it would arise in longer time simulation. The back-flow particles can be also observed in one-dimensional simulations with the same parameter setting, the Weibel instability is the two-dimensional proper.

APPENDIX A

Particle-in-Cell Method

The particle acceleration mechanism and the magnetic field dissipation mechanism closely relate to the plasma kinetic effects. When one numerically simulates the kinetic effect, the simulation method should resolve the particle motion. The magneto-hydro-dynamics (MHD) simulation can solve the global structure of plasma, but not the particle motion. The kinetic effect is replaced by some parameters in the MHD equations. The most popular methods to describe the plasma kinetic effect are the Vlasov method and the Particle-in-Cell (PIC) method.

In the Vlasov method, a distribution function is solved by the Vlasov equation in the phase space. This method make a numerical noise low level. The problem is the memory size for the calculation. For instance, if one tries a small two-dimensional simulation with 100×100 spatial grids and $100 \times 100 \times 100$ momentum spatial grids, the total grid number is 10^{10}! The Vlasov method in case of the multi-dimensional simulation requires huge memory size for present computational resources.

In the PIC method, individual particle is directly solved by the equation of motion. The electromagnetic fields are defined on the spatial grids and are solved by the Maxwell's equations. The procedure for one time step in PIC method is shown below (see also figure A.1). The electromagnetic fields on each particle are obtained from neighboring grids by spatial interpolations. The Lorentz force by the electromagnetic fields progress the time step of these particles via the equation of motion. The position and velocity of these particles define the charge density and the current density on the neighboring grids. Then the Maxwell's equations progress the time step of the electromagnetic fields on the grids. These information interchange between particles and grids via the spacial interpolations yields larger numerical noise than

that of the Vlasov method. In the PIC method, usually the particle number in a grid should be much larger than unity to keep statistical precision and to decrease the noise. The memory size required by this PIC method is basically the grid number plus the particle number. Although the large number of particles consumes a large amount of memory, the size is usually much smaller than that of the Vlasov method with same scale. For these reasons, we used the PIC method for study of kinetic plasma processes.

As shown above, the PIC method mainly consists of three parts, particle motion solver, electromagnetic field solver and momentum calculation (interpolation between particles and grids). In this appendix we introduce the basic schemes of the particle solver, the electromagnetic field solver and the momentum calculation in the PIC method.

In the following sections, the position and velocity of particles are defined on integer and half-integer time steps, respectively. Charge density, electric fields and magnetic fields are defined on integer spacial grids and integer time steps. Current densities are defined on half-integer grids and half-integer time steps. For some parameters, interpolations between spacial grids are needed to satisfy these definition.

A.1 Particle Motion Solver

The velocity of the particles are solved by the equation of motion. In case that the particle velocity is nearly light velocity, one should use the relativistic equation of motion,

$$m\frac{d\boldsymbol{u}}{dt} = q\left\{\boldsymbol{E} + \frac{\boldsymbol{u}}{c\gamma} \times \boldsymbol{B}\right\}, \tag{A.1}$$

where m is the rest mass, q is the charge, $\boldsymbol{u}$ is the four-velocity, γ is the Lorentz factor defined by $\gamma = \sqrt{1 + u^2/c^2}$, and $\boldsymbol{E}$ and $\boldsymbol{B}$ are electric fields and magnetic fields, respectively. The most popular method to solve the particle motion in the PIC method is Buneman-Boris method (Boris, 1970), which ensures no work volume by the magnetic field. According to the method, the relativistic equation of motion (equation (A.1)) is rewritten in a difference equation form

$$\frac{\boldsymbol{u}^{n+1} - \boldsymbol{u}^{n+1}}{\Delta t} = \frac{q}{m}\left(\boldsymbol{E}^n + \frac{\boldsymbol{u}^{n+1/2} + \boldsymbol{u}^{n-1/2}}{2c\gamma} \times \boldsymbol{B}^n\right). \tag{A.2}$$

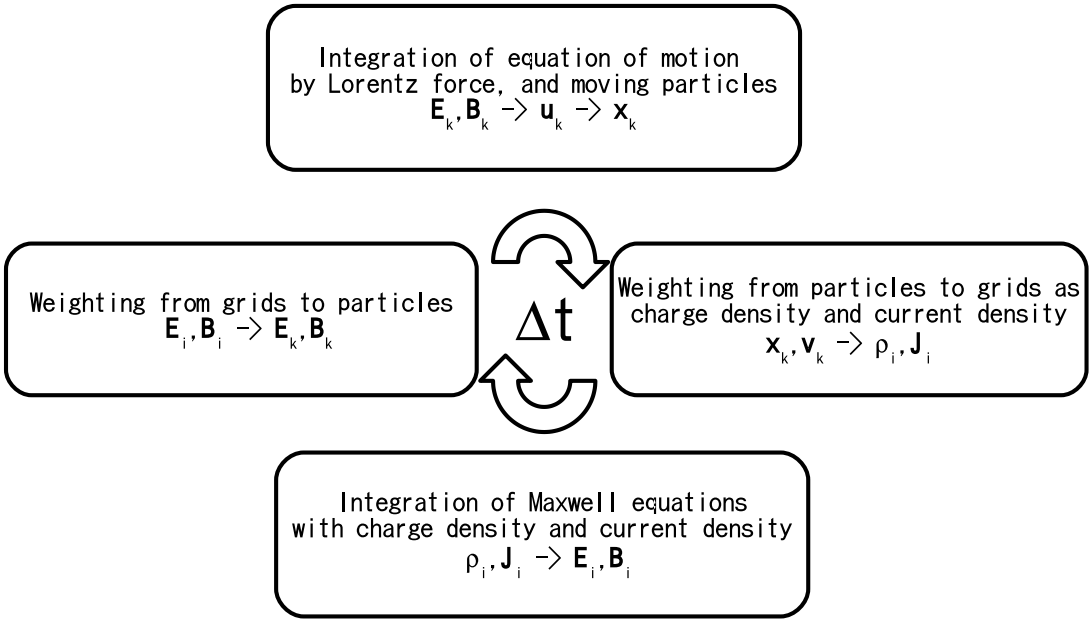

Figure A.1: Chart of the PIC method for one time step. Top and bottom squares show the solver of equation of motion and the Maxwell equations, respectively. Left and right show the interpolations between particles and grids (momentum calculations).

Now equation (A.2) is divided by three steps, an acceleration by $\boldsymbol{E}$ for a half time step ($\Delta t/2$), a rotation by $\boldsymbol{B}$ for one time step (Δt) and an acceleration by $\boldsymbol{E}$ for half time step ($\Delta t/2$) again. The first step and the final step are respectively expressed as

$$\boldsymbol{u}^{-} = \boldsymbol{u}^{n-1/2} + \frac{q}{m}\boldsymbol{E}^{n}\frac{\Delta t}{2}, \tag{A.3}$$

$$\boldsymbol{u}^{n+1/2} = \boldsymbol{u}^{+} + \frac{q}{m}\boldsymbol{E}^{n}\frac{\Delta t}{2}. \tag{A.4}$$

Substituting equation (A.3) and (A.4) into equation (A.1), the equation for the second step is derived,

$$\boldsymbol{u}^{+} = \boldsymbol{u}^{-} + \frac{2}{1+T^2}\left(\boldsymbol{u}^{-} + \boldsymbol{u}^{-} \times \boldsymbol{T}\right) \times \boldsymbol{T}, \tag{A.5}$$

where $\boldsymbol{T} = q\boldsymbol{B}^{n}\Delta t/(2mc\gamma^{-})$ and $\gamma^{-} = \sqrt{1+(u^{-})^2/c^2}$. Eventually the order of equation to be solved in the code is equation (A.3), (A.5) and (A.4). After converting the four-velocity $\boldsymbol{u}^{n+1/2}$ into the three-velocity $\boldsymbol{v}^{n+1/2}$ using $\boldsymbol{v}^{n+1/2} = \boldsymbol{u}^{n+1/2}/\sqrt{1+(u^{n+1/2}/c)^2}$, the position of the particles is updated by

$$\boldsymbol{x}^{n+1} = \boldsymbol{x}^{n} + \boldsymbol{v}^{n+1/2}\Delta t. \tag{A.6}$$

A.2 Electromagnetic Field Solver

For the two-dimensional simulation we used an advanced method shown in chapter 2. In this section we introduce one of the basic methods (Birdsall and Langdon, 2005), used in one-dimensional simulation (chapter 3). Now we solve the parameters along the x-axis. The magnetic field has only the z-component. From equation (2.1) and (2.2), in such case the electric field has x- and y-component, and the x-component is separated from the y-component as an electrostatic field given by the Poisson equation (equation (2.4)). Then the equation (2.1) and (2.2) can be rewritten by

$$\frac{1}{c}\frac{\partial E_y}{\partial t} = -\frac{\partial B_z}{\partial t} - \frac{4\pi}{c}J_y, \tag{A.7}$$

$$\frac{1}{c}\frac{\partial B_z}{\partial t} = \frac{\partial E_y}{\partial t}. \tag{A.8}$$

Defining $F^{\pm} \equiv E_y \pm B_z$, equation (A.7) and (A.8) become

$$\left(\frac{1}{c}\frac{\partial}{\partial t} \pm \frac{\partial}{\partial x}\right) F^{\pm} = -\frac{4\pi}{c} J_y. \tag{A.9}$$

In the difference equation form, these change to

$$\frac{(F^+)_i^{n+1} - (F^+)_i^n}{c\Delta t} + \frac{(F^+)_i^n - (F^+)_{i-1}^n}{\Delta x} = -\frac{4\pi}{c}(J_y)_{i-1/2}^{n+1/2}, \tag{A.10}$$

$$\frac{(F^-)_i^{n+1} - (F^-)_i^n}{c\Delta t} - \frac{(F^-)_{i+1}^n - (F^-)_i^n}{\Delta x} = -\frac{4\pi}{c}(J_y)_{i+1/2}^{n+1/2}. \tag{A.11}$$

These equations solves the advection of $F^{\pm}$, so there is no restriction by the Courant condition. Then one can set the relation between the spacial grid width Δx and the temporal step width Δt to $\Delta x = c\Delta t$. Then equation (A.10) and (A.11) are simplified as follows,

$$(F^{\pm})_i^{n+1} = (F^{\pm})_{i\mp1}^n - 4\pi(J_y)_{i\mp1/2}^{n+1/2}\Delta t. \tag{A.12}$$

These equations progress the time step of $F^{\pm}$ in the code. Finally they are converted into the electromagnetic fields,

$$E_y = \frac{1}{2}(F^+ + F^-), \tag{A.13}$$

$$B_z = \frac{1}{2}(F^+ - F^-). \tag{A.14}$$

Meanwhile the electrostatic field E_x is solved by

$$\frac{\partial E_x}{\partial x} = 4\pi\rho, \tag{A.15}$$

from equation (2.4). This equation is easily rewritten in the difference form,

$$(E_x)_{i+1/2}^n = (E_x)_{i-1/2}^n + 4\pi\rho_i^n. \tag{A.16}$$

One can use this equation to solve the electrostatic field E_x. In equation (A.16), E_x is defined on half-integer grids. However it should be re-defined on integer grids by linear interpolations, unless the self-force arise, which moves the particle by the electrostatic potential of itself.

Because the electrostatic field mixes with the other components in Maxwell's equations for multi-dimensional case, this method can not be directly extended to the multi-dimensional one.

A.3 Momentum Calculation

In the PIC method physical parameters are defined not only on the grids but also on particles. So charge density and current densities on grids, and electromagnetic fields work on particles must be correctly evaluated to solve electromagnetic fields and particles consistently. We introduce the most popular method of the interpolation between grids and particles.

To calculate the charge density and the current densities, the contribution of a particle is divided into neighboring grids. For the two-dimensional case the weights for each grid is proportional to the area of the opposite side over the particle (see figure A.2). For example the contributions of a charge by a particle to the grids are

$$\rho_{i,j} = q(1-\delta x)(1-\delta y), \tag{A.17}$$

$$\rho_{i+1,j} = q\delta x(1-\delta y), \tag{A.18}$$

$$\rho_{i,j+1} = q(1-\delta x)\delta y, \tag{A.19}$$

$$\rho_{i+1,j+1} = q\delta x\delta y. \tag{A.20}$$

The total charge density on the grid is obtained by the summation of all particles. The current density is similarly given using the particle velocity and position at the half-integer time step.

On the other hand, the contribution of electromagnetic fields works on a particle in the cell is inversion of the above.

$$\boldsymbol{A} = \boldsymbol{A}_{i,j}(1-\delta x)(1-\delta y) + \boldsymbol{A}_{i+1,j}\delta x(1-\delta y) + \boldsymbol{A}_{i,j+1}(1-\delta x)\delta y + \boldsymbol{A}_{i+1,j+1}\delta x\delta y, \tag{A.21}$$

where $\boldsymbol{A}$ is an arbitrary electromagnetic field vector.

Although we introduced a simple linear interpolation here, one has other options (e.g. Jacobs and Hesthaven (2006)). Although the higher order interpolation (shape factor) decrease the noise, the computational costs increase drastically. This is a reason that the higher order interpolation is not used frequently.

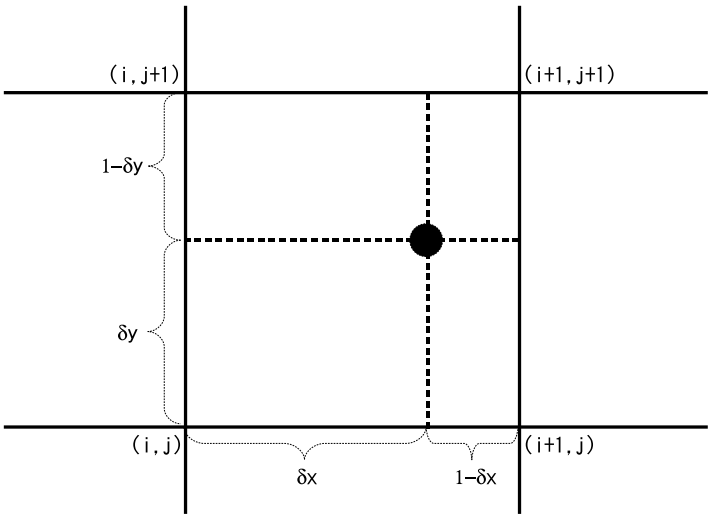

Figure A.2: Schematic diagram for interpolation between a particle and grids. The black circle means a particle in a cell. The abscissa and the ordinate show the x-grids and y-grids, respectively.

APPENDIX B

Code Check

In order to check the code, we show the dispersion relation. The simulation condition is uniform plasma with back ground magnetic field of y component $\boldsymbol{B} = (0, B_y, 0)$. The plasma has no bulk velocity. The thermal four-velocity is $u_{th} = 0.1$. The ratio of the gyro frequency and the plasma frequency, which characterizes the physical property, is $\Omega/\omega_p = 0.5$, where

$$\Omega = \frac{eB}{mc\gamma_{th}}, \tag{B.1}$$

$$\omega_p = \sqrt{\frac{8\pi n e^2}{m\gamma_{th}}}. \tag{B.2}$$

Figure B.1 shows the dispersion relation for parallel propagating waves by the simulation result. The contour is obtained by Fourier transformation for B_x. These modes can be expressed in equations by the linear analysis

$$\omega^2 = \frac{1}{2}\left[c^2k^2 + \omega_{UH}^2 \pm \sqrt{(c^2k^2 + \omega_{UH}^2)^2 k^4 - 4c^2k^2\Omega^2}\ \right], \tag{B.3}$$

where ω_{UH} is the upper-hybrid frequency $\omega_{UH} = \sqrt{\omega_p^2 + \Omega^2}$. The positive signed equation means the electromagnetic mode, which is a degeneracy of L-mode and R-mode in ion-electron plasma. The electromagnetic mode is described by a red dashed line in figure B.1. The frequency of the electromagnetic mode is ω_{UH} at $k = 0$, and asymptotically approaches to the frequency of $\omega = ck$ in high wavenumber. The negative one is the Alfvén mode, which is a degeneracy of whistler and ion cyclotron waves in ion-electron plasma. The Alfvén mode is described by a green dashed line in figure B.1. The frequency of this wave is $\omega = 0$ at $k = 0$ and $\omega \to \Omega$ for $k \to \infty$.

Figure B.2 shows the dispersion relation for perpendicular propagating waves by the simulation result. The contour is also obtained by Fourier transformation for B_x. These modes can

be expressed in equations by the linear analysis,

$$\omega^2 = \frac{1}{2}\left[(c^2+c_s^2)k^2+\Omega^2+\omega_p^2 \pm \sqrt{(c^2-c_s^2)^2k^4+2(c^2-c_s^2)(\omega_p^2-\Omega^2)k^2+(\Omega^2+\omega_p^2)^2}\ \right]. \quad \text{(B.4)}$$

,where c_s is the sonic wave,

$$c_s = \sqrt{(\Gamma-1)\frac{\gamma_{th}-1}{\gamma_{th}}}c. \quad \text{(B.5)}$$

Γ is a ratio of specific heat. In this case the particle velocity has three dimensional distribution, and this value is $\Gamma = 4/3$. The positive signed equation means the extra-ordinary mode (X-mode). This mode is described by a red dashed line in figure B.2. The frequency of the X-mode is also ω_{UH} at $k = 0$, and asymptotically approaches to the frequency of $\omega = ck$ in the high wavenumber. The negative one is the fast mode, described by a green dashed line in figure B.2. The frequency of this wave is $\omega = 0$ at $k = 0$ and asymptotically approaches to the frequency of the sonic wave.

Although the amplitude of these high wavenumber components decreases by the low-pass filter, All of these waves are well fitted by the linear dispersion relations.

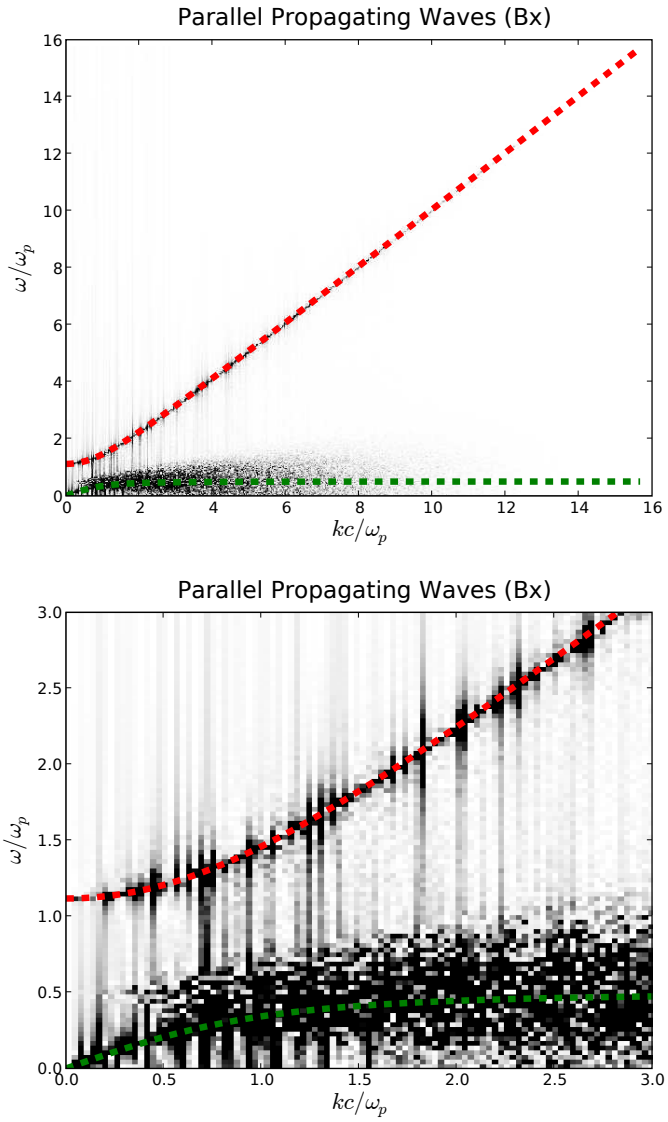

Figure B.1: Dispersion relations of parallel propagating waves of B_x. The contour shows the simulation result. The red dashed line is the electromagnetic mode and the green dashed line is the Alfvén mode. These modes are described by equation (B.3). The top is the full simulation scale. The bottom is that of a low frequency part.

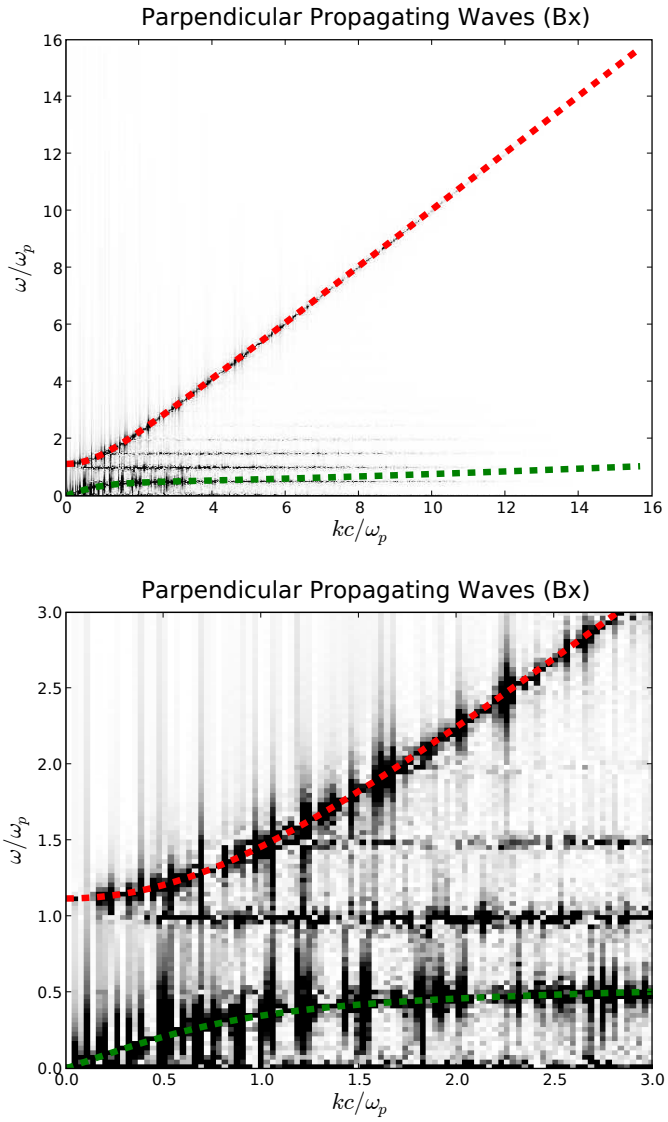

Figure B.2: Dispersion relations of perpendicular propagating waves of B_x. The contour shows the simulation result. The red dashed line is the extra-ordinary mode and the green dashed line is the fast mode. These modes are described by equation (B.4). The top is the full simulation scale. The bottom is that of a low frequency part.

APPENDIX C

Magnetosonic Wave

The magnetosonic wave generated at the shock front transfers the bulk energy of the current sheet plasma into the shock heated downstream plasma. The magnetosonic wave is believed to play a significant role in the additional plasma acceleration and the shock dynamics in the downstream. In this appendix we estimate the magnetosonic wave amplitude on a simple assumption of conservation laws and compare the result with the simulation result. First, we evaluate the upstream current sheet plasma momentum and the downstream magnetosonic wave momentum. Provided the upstream uniform plasma is converted into the downstream one, we could approximately consider the current sheet plasma n_{cs0}, added on the uniform one n_0, as exciting the magnetosonic wave. Therefore the uniform component of the upstream and the downstream is ignored in the following equations. Then the total momentum of the injection current sheet plasma exciting a magnetosonic wave is described

$$M_{cs0} = \int_{-\infty}^{\infty} 2mn_{cs0}(x)u_0 dx \tag{C.1}$$

$$= 4\lambda_{cs0} mn_{cs0} u_0, \tag{C.2}$$

where $n_{cs0}(x) = n_{cs0}\cosh^{-2}(x/\lambda_{cs0})$. The magnetosonic wave momentum propagating with c_s in the downstream is

$$M_{ms} = \int dt \int dx \left\{ -\frac{\partial}{\partial x}\left(\frac{B_z(x)^2 + E_y(x)^2}{8\pi} + P_{th}(x) \right) \right\} \tag{C.3}$$

$$= \frac{1}{c_s}\int_{-\infty}^{\infty} \left\{ \frac{2B_1B_2(x) + (1 + c_s^2/c^2)\, B_2^2(x)}{8\pi} + \left(2B_1B_2(x) + B_2^2(x)\right)\frac{P_{th1}}{B_1^2} \right\} dx \tag{C.4}$$

$$= \frac{2\lambda_{ms}}{c_s}\left\{ \pi\left(\frac{1}{8\pi} + \frac{P_{th1}}{B_1^2}\right) B_1B_2 + \left(\frac{1 + c_s^2/c^2}{8\pi} + \frac{P_{th1}}{B_1^2}\right) B_2^2 \right\}, \tag{C.5}$$

where

$$B_z(x) = B_1 + B_2(x) = B_1 + B_2 \cosh^{-1}(x/\lambda_{ms}), \tag{C.6}$$

$$E_y(x) = (c_s/c)\, B_2(x) = (c_s/c)\, B_2 \cosh^{-1}(x/\lambda_{ms}), \tag{C.7}$$

$$P_{th}(x) = P_{th1} + P_{th2}(x) = P_{th1} + P_{th2} \cosh^{-2}(x/\lambda_{ms}). \tag{C.8}$$

The index "1" and "2" mean the downstream background part and the wave part quantity, respectively. In the equation (C.4) we used a relation $B(x)_z^2/P_{th}(x) = const.$ on the assumption of the magnetic moment conservation in highly relativistic case $mu^2/\gamma B_z \sim T(x)/B_z(x) = const.$, mass flux conservation and magnetic flux conservation $B_z(x)/n(x) = const.$, where the thermal pressure is described by $P_{th}(x) = n(x)T(x)$. If a part of the injection current sheet momentum converts into the magnetosonic wave momentum $\alpha M_{cs0} = M_{ms}$ for $0 < \alpha < 1$,

$$\frac{B_2}{B_0} = a\left(-1 + \sqrt{1+b}\right), \tag{C.9}$$

$$a = \frac{\pi}{2}\,\frac{B_1}{B_0}\,\frac{\sigma_0 B_1^2/B_0^2 + P_{th1}/(n_0 mc^2\gamma_0)}{\sigma_0\,(1+c_s^2/c^2)\,B_1^2/B_0^2 + P_{th1}/(n_0 mc^2\gamma_0)}, \tag{C.10}$$

$$b = \frac{8\alpha c_s/c\; n_{cs0}/n_0}{\pi^2 \lambda_{ms}/\lambda_{cs0}}\,\frac{\sigma_0\,(1+c_s^2/c^2)\,B_1^2/B_0^2 + P_{th1}/(n_0 mc^2\gamma_0)}{\left\{\sigma_0 B_1^2/B_0^2 + P_{th1}/(n_0 mc^2\gamma_0)\right\}^2}. \tag{C.11}$$

The upstream parameters with index 0 describe downstream parameters with index 1 by using the Rankine-Hugoniot relations (Gallant et al., 1992), $n_1/n_0 = B_1/B_0 = 2.8$, $T_1 = 0.48$ for $\sigma_0 = 0.1$. In this case equation (C.9) is

$$\frac{B_2}{B_0} = \frac{3.3}{0.58 + 0.38 c_s^2/c^2}\left(-1 + \sqrt{1 + (3.8 + 1.4 c_s^2/c^2)\,\frac{\alpha c_s/c}{\lambda_{ms}/\lambda_{cs0}}}\right). \tag{C.12}$$

On the other hand the magnetosonic wave amplitudes for CASE2-4 are $(B_1 + B_2)/B_0 \approx 4.1, 6.7, 7.4$ respectively. For CASE1 we presume that the amplitude is same to the average of the uniform downstream value ~ 3.1, because it is under the fluctuation level. The wave length of a magnetosonic wave should be larger than the inertia length $c/\omega_p = 0.42c/\omega_{p0}$, which could yield a criterion classifying the current sheet width into the thick and the thin current sheet. In the thick current sheet case (CASE3 and CASE4), we assume that the width and group velocity are $\lambda_{ms} \sim \lambda_{cs0}$ and $c_s \sim c$, respectively, on the basis of the simulation results.

If one substitutes these parameters into equation (C.12), the amplitude B_2/B_0 is constant for fixed α. The magnetosonic wave amplitude is approximately ~ 6.7 and ~ 7.4 for CASE3 and CASE4, respectively. Using these average, one can determine as $\alpha = 0.65$. Although this value, of course, includes not only the actual momentum conversion ratio, but also other error effects, we use this α to evaluate the thin current sheet cases (CASE1 and CASE2) for ease. In the thin current sheet case, the width and the group velocity are $\lambda_{ms} = c/\omega_p = 0.42c/\omega_{p0}$ and $c_s \sim 0.82c$, respectively. Here we used a dispersion relation with a low frequency approximation for relativistic hot magnetosonic wave in two-dimensional velocity space,

$$\frac{\omega}{k} \simeq \sqrt{\frac{1+2\sigma}{2+2\sigma}}c = 0.82c, \tag{C.13}$$

where $\sigma = 0.57$ is a ratio of the magnetic energy density to the thermal energy density. Then one can derive the magnetosonic wave amplitude as a function of the current sheet width,

$$\frac{B_2}{B_0} = 4.0\left(-1 + \sqrt{1 + 6.0\frac{\lambda_{cs0}}{c/\omega_{p0}}}\right). \tag{C.14}$$

Figure C.1 shows the simulation results and the above model results. Equation (C.14) roughly explains the simulation results of CASE1 and CASE2. The essence of this result is that the wave length should be larger than the inertia length.

The momentum density determines the amplitude. In case of the thick current sheet $\lambda_{cs0} > c/\omega_p$, since the magnetosonic wave length λ_{ms} is comparable to the current sheet width, the amplitude is constant for different current sheet width λ_{cs0}. However in the thin case $\lambda_{cs0} < c/\omega_p$, the magnetosonic wave length is the inertia length c/ω_p. Therefore as the initial current sheet width decreases, the magnetosonic wave momentum also decreases. As a result the amplitude becomes smaller than the thick current sheet case with the same current sheet plasma density n_{cs0}/n_0. This is the reason that the amplitude of the magnetosonic wave is quite small in CASE1 and CASE2.

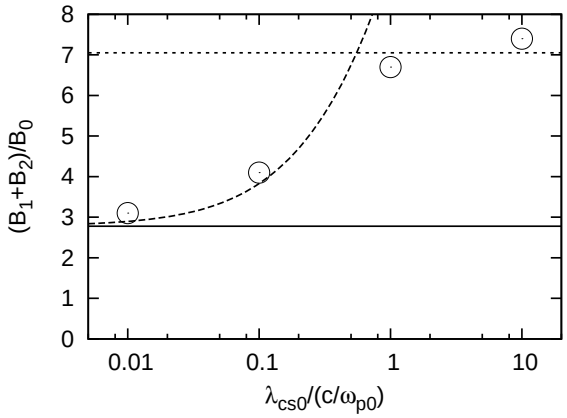

Figure C.1: Magnetosonic wave amplitude. The solid line shows background magnetic field as defined by the shock jump conditions. The dashed and the dotted line are described by the equation C.12 for $\lambda_{ms} = c/\omega_p$ and $\lambda_{ms} = \lambda_{cs0}$, respectively. The circles are the simulation results.

APPENDIX D

Unequally Spaced Current Sheets in Two Dimension

In chapter 4, we showed the case of equally spaced current sheets. For comparison we also investigate the unequally case. Similar to chapter 4, the results are also divided into two cases, "thick current sheet" and "thin current sheet". All parameters conform to the case of the equally spaced current sheets except the clearance. In this case we set the clearances $L_1 = 5L/4$ and $L_2 = 3L/4$, where L_1 is positive B_y region, L_1 is positive B_y region and L is the clearance for equally spaced current sheets case defined in chapter 4. Then the average of B_y for the region including two current sheets is $\langle B_0 \rangle = 0.25B_0$, on the other hand in the equally spaced current sheets case in chapter 3 that is $\langle B_0 \rangle = 0.25B_0$. These clearance is same setting to the unequally case in section 3.4.1.

D.1 Thick Current Sheet

Figure D.1 shows the particle distribution in phase space (x - u_x, u_y, u_z, γ), and the positron number density with the magnetic field lines in two-dimensional space (x-y). The phase space plots are represented by summation for y-direction. The magnetized electron-positron plasma are injected from the left boundary ($x = 0$), and are reflected by the right boundary ($x = 409.6$).

The shock front is located at $x \sim 265c/\omega_{p0}$. So the left region is the shock upstream and the right region is the shock downstream. In order to avoid the reflection of the magnetosonic wave at the boundary (see section 3.3.2), we prepare the uniform shock downstream to get through the magnetosonic waves by the injection of the uniform plasma in the beginning of the simulation. The uniform region is $x > 355c/\omega_{p0}$ In the positron number density plot with the

magnetic field lines, note that the direction of the magnetic field lines is anti-parallel on the both side of the current sheet, represented as dense parts with monochromatic contour.

Now the averaged alternating magnetic field is $\langle B_0 \rangle = 0.25 B_0$. Then there is no back-flow particles for long distance, even though some particles have energy larger than the criterion defined by equation (4.3). The back-flow distance is the gyro radius given by the averaged magnetic field $\langle B_0 \rangle = 0.25 B_0$ at most. Such particles are seen at just upstream of the shock front ($x = 255 - 265$) in figure D.1, and thin current filaments are also seen at the same region. However it is not enough to generate electric field for the particle acceleration.

Compared with the current sheets clearance (L) in section 4.4, this case has larger ($L_1 > L$) and smaller one ($L_2 < L$). Although the fluctuation of the shock front grows continuously in figure 4.3 of section 4.4, the larger clearance prevents the fluctuation from growing. As a result, drastic magnetic reconnections in the downstream are suppressed, and the large amplitude magnetosonic waves excited at the shock front propagate without dispersion, like the one-dimensional case. The large amplitude magnetosonic wave momently gives the energy to particles as shown in the first paragraph of section 3.3.3. These high energy particles seen in the bottom plot in figure D.1 as dots. The time evolution of the energy spectrum is shown in figure D.3. The high energy part is power-law, but no growth of time.

D.2 Thin Current Sheet

Next we show the case of thin current sheets. As shown in appendix C, the amplitude of the magnetosonic wave is not so large. So we do not prepare the absorption region unlike the thick current sheets case.

Figure D.4 shows the particle distribution in phase space (x - u_x, u_y, u_z, γ), and the positron number density with the magnetic field lines in two-dimensional space (x-y). The phase space plots are represented by summation for y-direction. The magnetized electron-positron plasma are injected from the left boundary ($x = 0$), and are reflected by the right boundary ($x = 163.8$). The shock front is located at $x \sim 108 c/\omega_{p0}$. Similar to the above "thick current sheet" case,

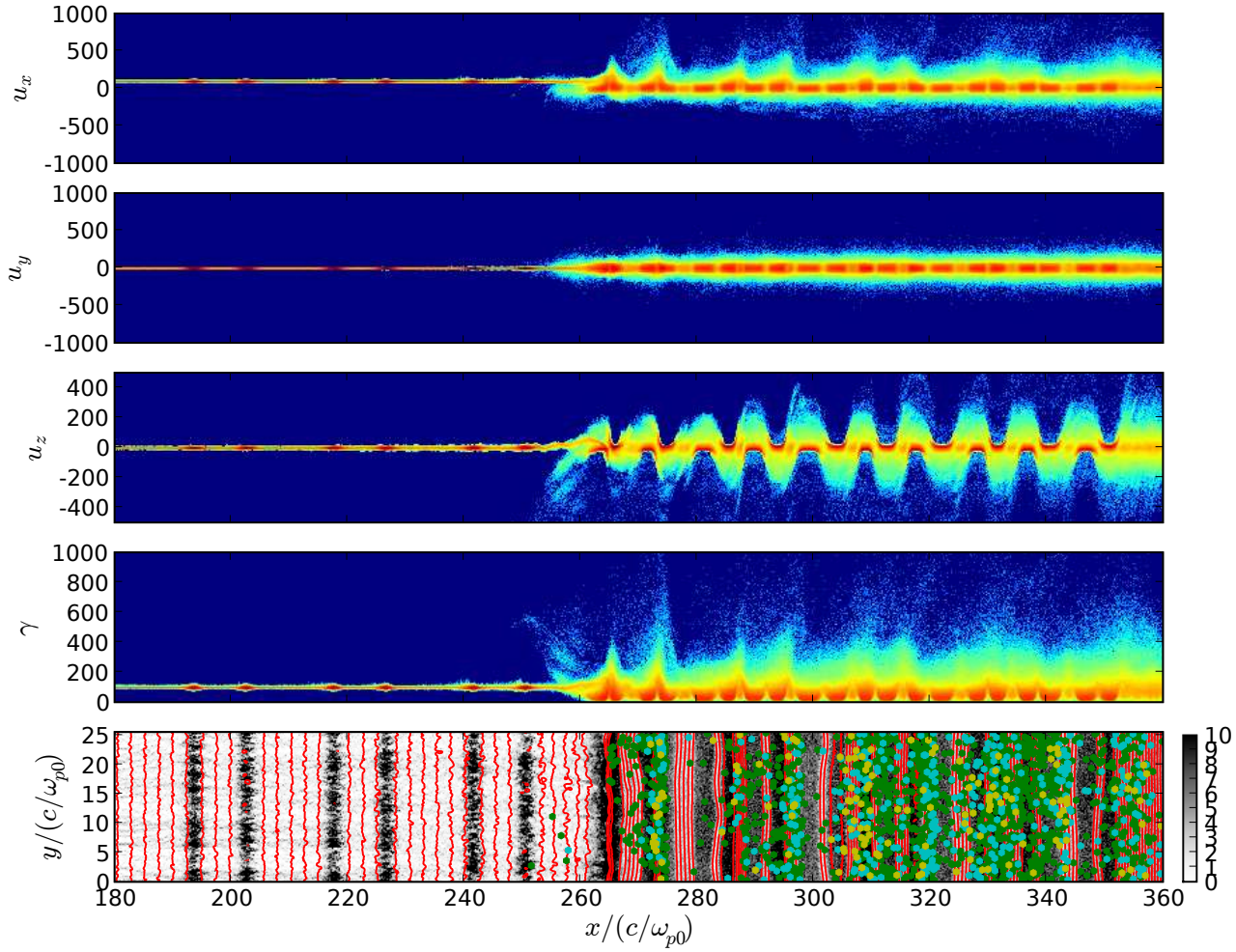

Figure D.1: Phase space density plots and number density with magnetic field lines for positron. All abscissa are spacial axes for x. From the above the phase space density for u_x, u_y, u_z and γ is represented by the color contour with logarithmic scale. Bottom shows the positron number density as the monochromatic contour and the magnetic field lines with red lines. The density contour is normalized by the initial upstream value. The green, cyan and yellow dots mean the high Lorentz factor particles of > 800, > 1000 and > 1200, respectively.

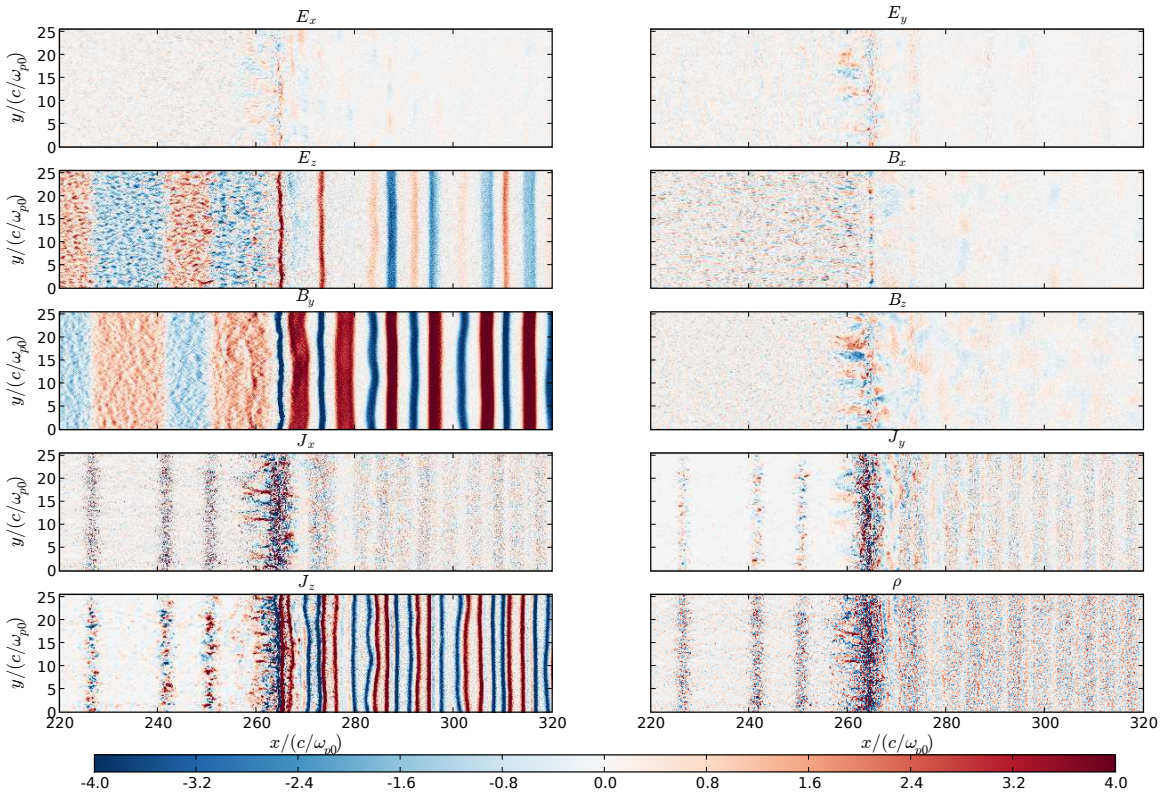

Figure D.2: Spacial distribution of electric fields (E_x, E_y, E_z), magnetic fields (B_x, B_y, B_z), current densities (J_x, J_y, J_z) and charge density (ρ). All quantities are normalized by the initial upstream value of the background magnetic field (B_0). As shown by the color bar, red and blue mean positive and negative, respectively. The time of this snapshot is identical to that of figure D.1.

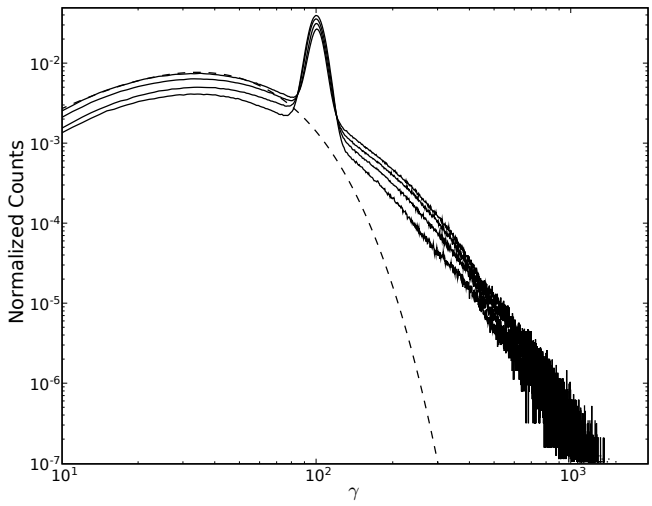

Figure D.3: The time evolution of normalized energy (Lorentz factor) spectrum of the plasma within the region of the alternating magnetic fields (solid line) and three-dimensional Maxwellian (dashed line). The solid lines show the energy spectrum for each $t = 40/\omega_{p0}$. The sharp peaks at $\gamma = 100$ are contribution of the cold upstream plasma. The spectrum with highest value at $\gamma \sim 30$ is the final time snapshot, which is same time to that of figure D.1 and D.2. The temperature of the Maxwellian is $T = 0.17mc^2\gamma_0$, which is smaller than the value expected by the Rankine-Hugoniot relations, to fit the moderate peak at $\gamma \sim 30$.

there is just a little back flow at $x = 104 - 108$ in figure D.4. Accordingly indications of the Weibel instability is barely observed in figure D.5.

Figure D.6 shows the y-averaged profiles for B_y (top), absolute value of B_z (middle) and positron number density n (bottom). B_y shows disappearance of the alternating magnetic fields at the shock front and uniform magnetic field in the downstream. The absolute value of B_z confirms almost no Weibel instability in this case, compared with figure 4.9 in section 4.5.

The plot of the number density clearly shows the downstream value $\sim 11n_0$. The averaged number density of the upstream $\langle n \rangle \simeq 2.7n_0$ is given by equation (4.10), so the compression ratio is ~ 4.1. On the other hand, the compression ratio, derived from the averaged-σ $\langle \sigma \rangle = 0.03$ defined by equation (4.12), is ~ 3.7. This is not well accorded with the simulation result ~ 4.1. Then let us think of the evaluation of σ using $\langle B_0 \rangle$, not $\langle B_0^2 \rangle$. Here we call it σ'. This is easily evaluated as follows,

$$\sigma' = \frac{\langle B_0 \rangle^2 / B_0^2}{\langle n \rangle / n_0} \sigma \sim 2.3 \times 10^{-3}, \tag{D.1}$$

where we used the values, $\langle n \rangle \simeq 2.7n_0$, $\langle B_0 \rangle = 0.25B_0$ and $\sigma = 0.1$. Then using σ' the compression ratio is ~ 4.0, and this value is roughly consistent with the simulation result ~ 4.1. Additionally the relation of the magnetic field amplitude between the averaged upstream value $\langle B_0 \rangle = 0.25B_0$ and the downstream one $B_1 \sim 1.0B_0$ satisfies the compression ratio ~ 4, shown in the top plot of figure D.6. Therefore the shock profile is characterized by the averaged magnetic field $\langle B_0 \rangle$, not by the square mean value $\langle B_0^2 \rangle^{1/2}$, in case that the alternating magnetic fields completely disappear.

Finally, figure D.7 shows the energy spectrum. This means no particle acceleration. These results support the acceleration via Weibel instability in chapter 4.

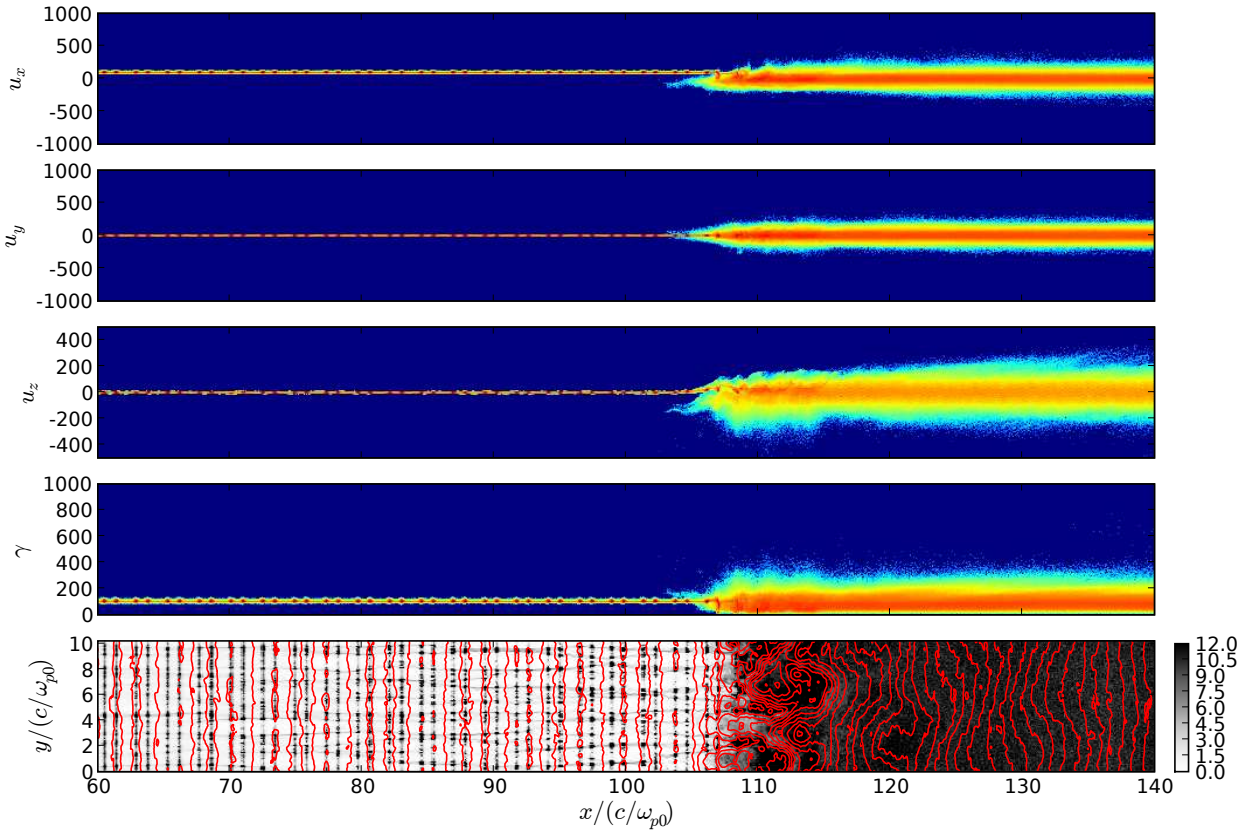

Figure D.4: Phase space density plots and number density with magnetic field lines for positron. All abscissa are spacial axes for x. From the above the phase space density for u_x, u_y, u_z and γ is represented by the color contour with logarithmic scale. Bottom shows the number density as the monochromatic contour and the magnetic field lines with red lines. There is no high Lorentz factor particles of > 800

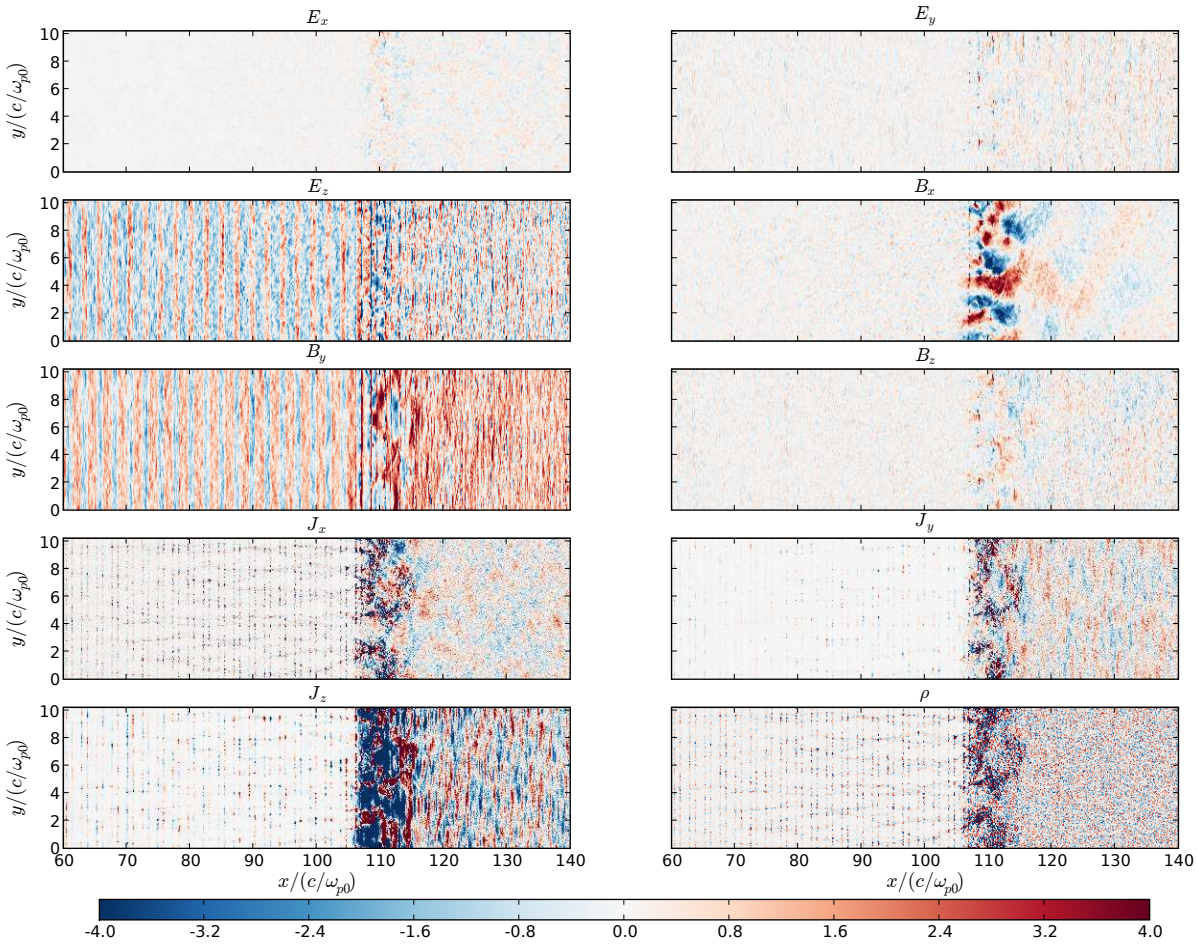

Figure D.5: Spacial distribution of electric fields (E_x, E_y, E_z), magnetic fields (B_x, B_y, B_z), current densities (J_x, J_y, J_z) and charge density ρ. All quantities are normalized by the initial upstream value of the background magnetic field (B_0). As shown by the color bar, red and blue mean positive and negative, respectively. The time of this snapshot is identical to that of figure D.4 and D.6.

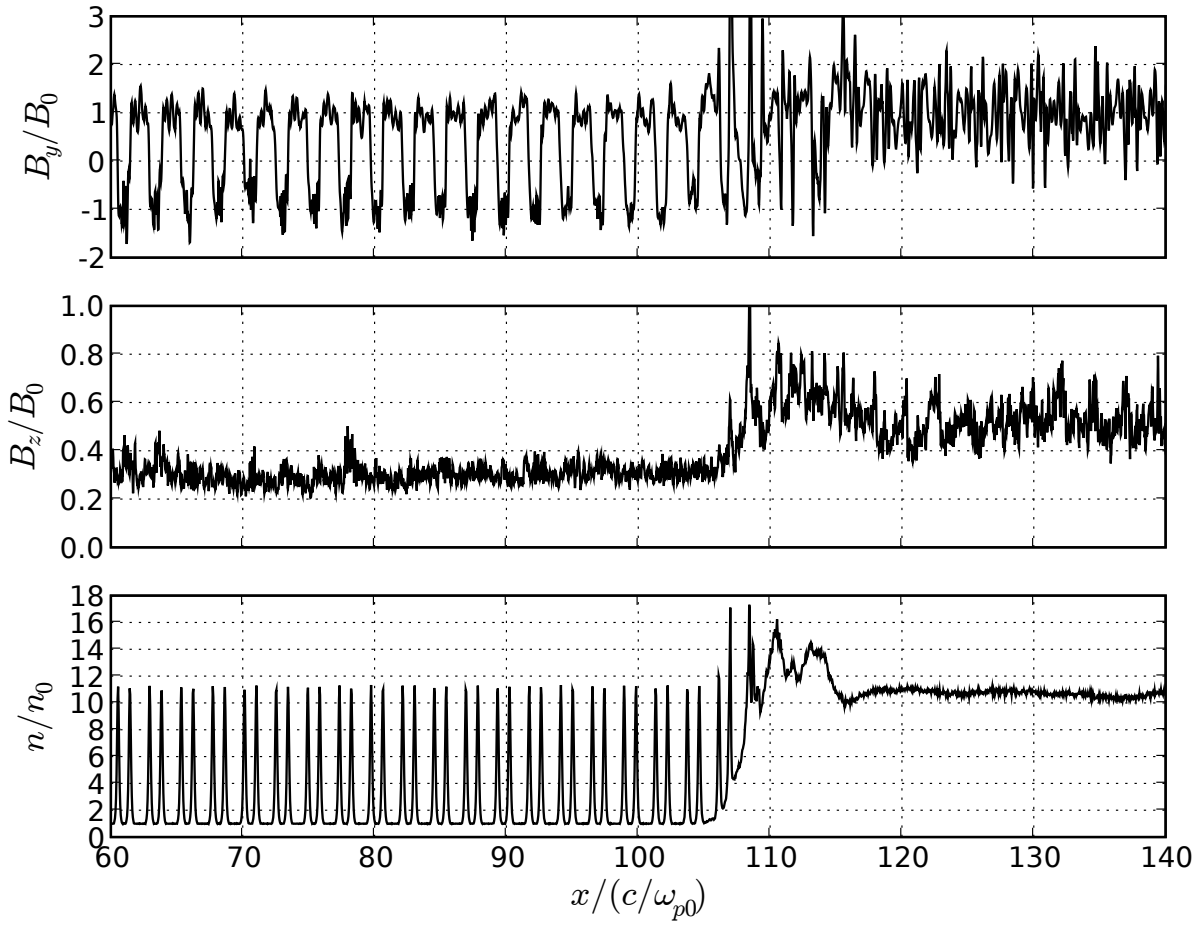

Figure D.6: Shock profiles for x-direction, averaged over y. Top shows the magnetic field B_y, middle is the *absolute value* of B_z and bottom is number density of positron n. They are normalized by each initial upstream value.

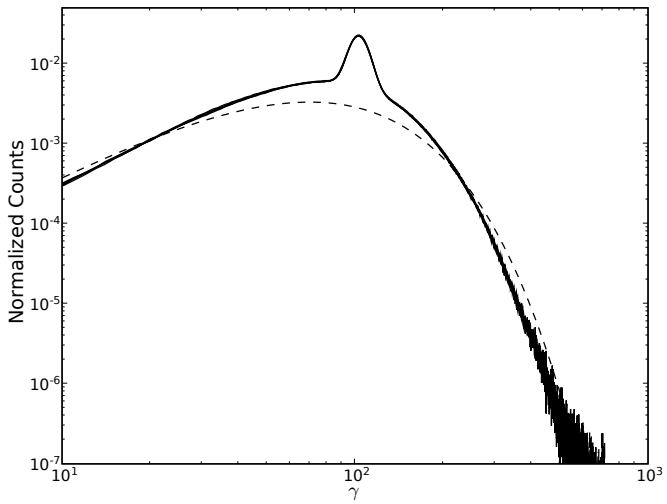

Figure D.7: Time evolution of normalized energy (Lorentz factor) spectrum of the plasma within the region of the alternating magnetic fields (solid line) and two-dimensional Maxwellian (dashed line) defined by equation (4.15). The solid lines show the energy spectrum for each $t = 30/\omega_{p0}$, but all plots overlap each other and no time evolution is observed. The peaks at $\gamma = 100$ are contribution of the cold upstream plasma. The time of the final spectrum is at the same to figure D.4, D.5 and D.6. The temperature of the Maxwellian is $T = 0.35mc^2\gamma_0$, which is almost consistent with the value expected by the Rankine-Hugoniot relations.

Bibliography

Aharonian, F. A. and A. M. Atoyan (1998) "Nonthermal Radiation of the Crab Nebula", in N. Shibazaki ed. *Neutron Stars and Pulsars: Thirty Years after the Discovery*, pp. 439–+.

Arons, J. (1979) "Some problems of pulsar physics", *Space Science Reviews*, Vol. 24, pp. 437–510.

——— (2004) "Theory of pulsar winds", *Advances in Space Research*, Vol. 33, pp. 466–474.

Begelman, M. C. and J. G. Kirk (1990) "Shock-drift particle acceleration in superluminal shocks - A model for hot spots in extragalactic radio sources", *Astrophys. J.* , Vol. 353, pp. 66–80.

Bell, A. R. (1978a) "The acceleration of cosmic rays in shock fronts. I", *Monthly Notices of the RAS* , Vol. 182, pp. 147–156.

——— (1978b) "The acceleration of cosmic rays in shock fronts. II", *Monthly Notices of the RAS* , Vol. 182, pp. 443–455.

Bietenholz, M. F. and P. P. Kronberg (1990) "The magnetic field of the Crab Nebula and the nature of its 'jet'", *Astrophys. J.* , Vol. 357, pp. L13–L16.

Birdsall, C. K. and A. B. Langdon (2005) *PLASMA PHYSICS VIA COMPUTER SIMULATION*: Taylor & Francis Group.

Blandford, R. D. and J. P. Ostriker (1978) "Particle acceleration by astrophysical shocks", *Astrophys. J.* , Vol. 221, pp. L29–L32.

Bogovalov, S. V. (1999) "On the physics of cold MHD winds from oblique rotators", *Astron. Astrophys.* , Vol. 349, pp. 1017–1026.

Boris, J. P. (1970) "Relativistic plasma simulation-optimization of a hybrid code", in *Proc. Fourth Conf. Num. Sim. Plasmas*.

Chiueh, T. (1989) "Numerical studies of multiple-encounter shock drift acceleration", *Astrophys. J.* , Vol. 341, pp. 497–505.

Coroniti, F. V. (1990) "Magnetically striped relativistic magnetohydrodynamic winds - The Crab Nebula revisited", *Astrophys. J.* , Vol. 349, pp. 538–545.

de Jager, O. C. and A. K. Harding (1992) "The expected high-energy to ultra-high-energy gamma-ray spectrum of the Crab Nebula", *Astrophys. J.* , Vol. 396, pp. 161–172.

Drenkhahn, G. and H. C. Spruit (2002) "Efficient acceleration and radiation in Poynting flux powered GRB outflows", *Astron. Astrophys.* , Vol. 391, pp. 1141–1153.

Emmering, R. T. and R. A. Chevalier (1987) "Shocked relativistic magnetohydrodynamic flows with application to pulsar winds", *Astrophys. J.* , Vol. 321, pp. 334–348.

Gaensler, B. M. and P. O. Slane (2006) "The Evolution and Structure of Pulsar Wind Nebulae", *Annual Review of Astronomy and Astrophysics*, Vol. 44, pp. 17–47.

Gallant, Y. A., M. Hoshino, A. B. Langdon, J. Arons, and C. E. Max (1992) "Relativistic, perpendicular shocks in electron-positron plasmas", *Astrophys. J.* , Vol. 391, pp. 73–101.

Godfrey, B. B. (1974) "Numerical Cherenkov Instabilities in Electromagnetic Particle Codes", *Journal of Computational Physics*, Vol. 15, pp. 504–+.

Goldreich, P. and W. H. Julian (1969) "Pulsar Electrodynamics", *Astrophys. J.* , Vol. 157, pp. 869–+.

Green, D. A., R. J. Tuffs, and C. C. Popescu (2004) "Far-infrared and submillimetre observations of the Crab nebula", *Monthly Notices of the RAS* , Vol. 355, pp. 1315–1326.

Greenwood, A. D., K. L. Cartwright, J. W. Luginsland, and E. A. Baca (2004) "On the elimination of numerical Cerenkov radiation in PIC simulations", *Journal of Computational Physics*, Vol. 201, pp. 665–684.

Haruki, T., J. I. Sakai, and S. Saito (2006) "Electromagnetic wave emission during collision between a current sheet and a fast magnetosonic shock associated with coronal mass ejections", *Astron. Astrophys.* , Vol. 455, pp. 1099–1103.

Hibschman, J. A. and J. Arons (2001a) "Pair Multiplicities and Pulsar Death", *Astrophys. J.* , Vol. 554, pp. 624–635.

——— (2001b) "Pair Production Multiplicities in Rotation-powered Pulsars", *Astrophys. J.* , Vol. 560, pp. 871–884.

Hickson, P. and S. van den Bergh (1990) "CCD observations of the polarization of the Crab Nebula", *Astrophys. J.* , Vol. 365, pp. 224–229.

Hoh, F. C. (1966) "Stability of Sheet Pinch", *Physics of Fluids*, Vol. 9, pp. 277–284.

Horns, D. and F. A. Aharonian (2004) "The Crab Nebula: Linking MeV Synchrotron and 50 TeV Inverse Compton Photons", in V. Schoenfelder, G. Lichti, and C. Winkler eds. *5th INTEGRAL Workshop on the INTEGRAL Universe*, Vol. 552 of ESA Special Publication, pp. 439–+.

Hoshino, M. and J. Arons (1991) "Preferential positron heating and acceleration by synchrotron maser instabilities in relativistic positron-electron-proton plasmas.", *Physics of Fluids B*, Vol. 3, pp. 818–833.

Hoshino, M., J. Arons, Y. A. Gallant, and A. B. Langdon (1992) "Relativistic magnetosonic shock waves in synchrotron sources - Shock structure and nonthermal acceleration of positrons", *Astrophys. J.* , Vol. 390, pp. 454–479.

Hoshino, M. (2001) "Nonthermal Particle Acceleration in Shock Front Region:"Shock Surfing Accelerations"", *Prog. Theor. Phys. Suppl.*, Vol. 143, pp. 149–181.

Hudson, P. D. (1965) "Reflection of charged particles by plasma shocks", *Monthly Notices of the RAS* , Vol. 131, pp. 23–+.

Jacobs, G. B. and J. S. Hesthaven (2006) "High-order nodal discontinuous Galerkin particle-in-cell method on unstructured grids", *Journal of Computational Physics*, Vol. 214, pp. 96–121.

Jaroschek, C. H., R. A. Treumann, H. Lesch, and M. Scholer (2004) "Fast reconnection in relativistic pair plasmas: Analysis of particle acceleration in self-consistent full particle simulations", *Physics of Plasmas*, Vol. 11, pp. 1151–+.

Kato, T. N. (2005) "Saturation mechanism of the Weibel instability in weakly magnetized plasmas", *Physics of Plasmas*, Vol. 12, pp. 705–+.

——— (2007) "Relativistic Collisionless Shocks in Unmagnetized Electron-Positron Plasmas", *Astrophys. J.* , Vol. 668, pp. 974–979.

Kennel, C. F. and F. V. Coroniti (1984a) "Confinement of the Crab pulsar's wind by its supernova remnant", *Astrophys. J.* , Vol. 283, pp. 694–709.

——— (1984b) "Magnetohydrodynamic model of Crab nebula radiation", *Astrophys. J.* , Vol. 283, pp. 710–730.

Kirk, J. G. and O. Skjæraasen (2003) "Dissipation in Poynting-Flux-dominated Flows: The σ-Problem of the Crab Pulsar Wind", *Astrophys. J.* , Vol. 591, pp. 366–379.

Kirk, J. G., O. Skjæraasen, and Y. A. Gallant (2002) "Pulsed radiation from neutron star winds", *Astron. Astrophys.* , Vol. 388, pp. L29–L32.

Kirk, J. G. (2004) "Particle Acceleration in Relativistic Current Sheets", *Physical Review Letters*, Vol. 92, No. 18, pp. 181101–+.

——— (2006) "Dissipation in pulsar winds", *Advances in Space Research*, Vol. 37, pp. 1970–1974.

Larrabee, D. A., R. V. E. Lovelace, and M. M. Romanova (2003) "Lepton Acceleration by Relativistic Collisionless Magnetic Reconnection", *Astrophys. J.* , Vol. 586, pp. 72–78.

Lyubarsky, Y. and J. G. Kirk (2001) "Reconnection in a Striped Pulsar Wind", *Astrophys. J.* , Vol. 547, pp. 437–448.

Lyubarsky, Y. E. (2003) "The termination shock in a striped pulsar wind", *Monthly Notices of the RAS* , Vol. 345, pp. 153–160.

Lyubarsky, Y. (2005) "The termination shock in a striped pulsar wind", *Advances in Space Research*, Vol. 35, pp. 1112–1115.

Marsden, P. L., F. C. Gillett, R. E. Jennings, J. P. Emerson, T. de Jong, and F. M. Olnon (1984) "Far-infrared observations of the Crab nebula", *Astrophys. J.* , Vol. 278, pp. L29–L32.

Mészáros, P. (2001) "Gamma-Ray Bursts: Accumulating Afterglow Implications, Progenitor Clues, and Prospects", *Science*, Vol. 291, pp. 79–84.

Michel, F. C. (1971) "Coherent Neutral Sheet Radiation from Pulsars", *Comments on Astrophysics and Space Physics*, Vol. 3, pp. 80–+.

——— (1973) "Rotating Magnetospheres: an Exact 3-D Solution", *Astrophys. J.* , Vol. 180, pp. L133+.

——— (1982) "Theory of pulsar magnetospheres", *Reviews of Modern Physics*, Vol. 54, pp. 1–66.

——— (1994) "Magnetic structure of pulsar winds", *Astrophys. J.* , Vol. 431, pp. 397–401.

Mori, K., D. N. Burrows, J. J. Hester, G. G. Pavlov, S. Shibata, and H. Tsunemi (2004) "Spatial Variation of the X-Ray Spectrum of the Crab Nebula", *Astrophys. J.* , Vol. 609, pp. 186–193.

Nishikawa, K.-I., P. Hardee, G. Richardson, R. Preece, H. Sol, and G. J. Fishman (2005) "Particle Acceleration and Magnetic Field Generation in Electron-Positron Relativistic Shocks", *Astrophys. J.* , Vol. 622, pp. 927–937.

Pétri, J. and Y. Lyubarsky (2007) "Magnetic reconnection at the termination shock in a striped pulsar wind", *Astron. Astrophys.* , Vol. 473, pp. 683–700.

Piran, T. (1999) “Gamma-ray bursts and the fireball model”,, Vol. 314, pp. 575–667.

Rees, M. J. and J. E. Gunn (1974) “The origin of the magnetic field and relativistic particles in the Crab Nebula”, *Monthly Notices of the RAS* , Vol. 167, pp. 1–12.

Sagdeev, R. Z. (1966) “Cooperative Phenomena and Shock Waves in Collisionless Plasmas”, *Reviews of Plasma Physics*, Vol. 4, pp. 23–+.

Schmidt, G. D., J. R. P. Angel, and E. A. Beaver (1979) “The small-scale polarization of the Crab Nebula”, *Astrophys. J.* , Vol. 227, pp. 106–113.

Spitkovsky, A. (2005) “Simulations of relativistic collisionless shocks: shock structure and particle acceleration”, in T. Bulik, B. Rudak, and G. Madejski eds. *Astrophysical Sources of High Energy Particles and Radiation*, Vol. 801 of American Institute of Physics Conference Series, pp. 345–350.

Tsubouchi, K. and H. Matsumoto (2005) “Effect of upstream rotational field on the formation of magnetic depressions in a quasi-perpendicular shock downstream”, *Journal of Geophysical Research (Space Physics)*, Vol. 110, pp. 4101–+.

Vermeulen, R. C. and M. H. Cohen (1994) “Superluminal motion statistics and cosmology”, *Astrophys. J.* , Vol. 430, pp. 467–494.

Weibel, E. S. (1959) “Spontaneously Growing Transverse Waves in a Plasma Due to an Anisotropic Velocity Distribution”, *Physical Review Letters*, Vol. 2, pp. 83–84.

Weisskopf, M. C., J. J. Hester, A. F. Tennant, R. F. Elsner, N. S. Schulz, H. L. Marshall, M. Karovska, J. S. Nichols, D. A. Swartz, J. J. Kolodziejczak, and S. L. O’Dell (2000) “Discovery of Spatial and Spectral Structure in the X-Ray Emission from the Crab Nebula”, *Astrophys. J.* , Vol. 536, pp. L81–L84.

Yee, K. S. (1966) “Numerical Solution of Inital Boundary Value Problems Involving Max well’s Equations in Isotropic Media”, *IEEE Trans. Antennas Propag.*, Vol. 14, p. 302.

Zenitani, S. and M. Hoshino (2001) "The Generation of Nonthermal Particles in the Relativistic Magnetic Reconnection of Pair Plasmas", *Astrophys. J.* , Vol. 562, pp. L63–L66.

——— (2005) "Relativistic Particle Acceleration in a Folded Current Sheet", *Astrophys. J.* , Vol. 618, pp. L111–L114.

——— (2007) "Particle Acceleration and Magnetic Dissipation in Relativistic Current Sheet of Pair Plasmas", *Astrophys. J.* , Vol. 670, pp. 702–726.